Electronic Transport through Suspended Graphene Nanoribbons Using a Scanning Tunneling Microscope

DOCTORAL THESIS by:

Niklas Friedrich

Thesis Supervisor:

José Ignacio Pacual Chico

Thesis Tutor:

Jose María Pitarke

August, 2022

This Thesis has been carried out at CIC nanoGUNE BRTA

Abstract

Single molecule spintronics aims to implement information processing techniques using electronic spins with tailored single molecules produced by organic chemistry. Graphene nanostructures are promising molecular platforms for single molecule spintronics because they combine electron mobility through conjugated parts with the possibility of hosting spin states. Industry driven research is capable of the integration of graphene flakes into transport devices for information processing. Recently, collaborations between chemists and physicists produced important advances in fabricating and characterizing spin-hosting graphene nanostructures. However, the study of the electronic transport through spin-hosting graphene nanostructures remains a challenge for testing the potential of single molecule spintronics.

In this Thesis, I investigated the two-terminal electronic transport through individual spin-hosting graphene nanoribbons (GNRs) suspended between the tip and the substrate of a low-temperature scanning tunneling microscope. Three types of GNRs were investigated: a seven and a five-seven-five armchair graphene nanoribbon, both with substitutional boron doping and a hybrid structure of (3,1)-chiral graphene nanoribbons and iron porphyrin. The ribbons were fabricated *in situ* under ultra-high vacuum conditions using on-surface synthesis strategies and characterized by means of scanning tunneling microscopy and spectroscopy (STM and STS). Bond resolved low bias images using a CO-functionalized tip confirmed the atomic structure of the molecules. Selected ribbons were positioned in a free-standing configuration bridging STM tip and substrate by mechanical manipulation with the STM tip.

The substitutional boron doping induces localized states in the seven armchair GNRs around the dopant sites. The high spatial localization of this states enables us to create a double tunneling barrier configuration,

similar to transport experiments through quantum dots, by suspending GNRs with the dopant site spaced from source and drain electrodes. Probing the transport by STS experiments in this configuration resolved resonant electron tunneling through boron state, excitations, and the ribbon's band states for free-standing segments up to more than $8\,\text{nm}$. In all these cases, we found that the transport is bipolar through the occupied boron state.

Density functional theory simulations show that the presence of the boron dopants interrupts the free propagation of electrons in the topologically non-trivial valence band of the seven armchair graphene nanoribbon. Consequently, a spin-polarization of the topologically protected edge state is predicted. We confirmed the magnetic character of the boron induced state experimentally through a Kondo resonance that emerged upon cleaving the boron dopants from the substrate.

Furthermore, we provide a detailed study of the topological origin of the boron induced state combining density functional theory (DFT) and mean field Hubbard (MFH) model calculations. We found both from experiment and calculations that it is possible to selectively shift the spin-polarized state to various positions inside the nanoribbon by controlling the hybridization of boron dopants with the surface.

Since the ribbons are semiconducting materials, electronic transport is essentially governed by electron tunneling through the band gap or by electron injection into frontier bands. We found a family of GNRs where the transport is ballistic while hosting localized spins inside. In agreement with this, two-terminal transport experiments showed ballistic transport with constant conductance ($\sim 0.2G_0$) for retraction length up to $3\,\text{nm}$ and a simultaneous Kondo resonance at zero bias. Atomic defects in the ribbon enable inelastic electron scattering resulting in electron-hole pair excitations that are described in an underfilled Hubbard model.

I also studied hybrid nanoribbon structures formed by chiral graphene nanoribbons contacted to spin-hosting iron porphyrin molecules. In two-terminal transport experiments through suspended hybrid ribbons, we were able to excite the iron's spin by inelastic electrons injected into the chiral GNRs. We found that on the surface, some iron porphyrin molecules undergo a renormalization of their magnetic anisotropy energy due to charge fluctuations in the spin-hosting d orbitals. Upon cleaving

it from the substrate, the molecule leaves this mixed valence regime, recovering the unperturbed magnetic anisotropy energy.

On the Shoulders of Many

Although, only my name appears below the title of this Thesis, I could not have written it without the support of many people. Some of them might not be aware of their impact on me, and for others, I might be unaware of their influences. In the following, I want to explicitly mention some of the people that had an important impact on me and this Thesis.

First of all, I want to thank my Doktorvater Nacho. I feel like I could not have had better luck than having had started my PhD under your guidance. You helped me to learn and grow scientifically in the last years. You always provided constructive feedback, and your passion for atomic scale magnetism ignited my motivation to dig down the deep holes of π magnetism in graphene nanoribbons, topology or many-body physics, to name just a few. But your support and motivation did not stop at the lab door. I always was certain, I could count on your help and support, when I needed it. I am greatly looking forward to continuing my research together with you.

Another great source of inspiration were my friends in and out of nanoGune. First of all, Stefano, thanks a lot for all the great time we had together, the pintxos, the philosophical beers, the less philosophical beers, the rides up-Igeldo-down-Igeldo-up-Igeldo-down-Igeldo — what a wonderful roundabout, isn't it? — and all the great advice you offered. Your curiosity and drive to learn and to ask questions impress me a lot. Not only you, but all the people that over the years shared my passion for cycling and discovered Euskadi together with me made me live a happier life! I am looking forward to many more rides with you. Leo, you did an awesome job always finding the steepest road ahead, and climbing it together. Matteo, Marita, Dongfei and Alex, I enjoyed each ride together! Thanks for keeping up with my crazy routes, sometimes even while discussing physics, and of course, also, for all the mostos and beers

we shared during or after the rides. Kat, Jon, Oksana, Anil and Lei, you are (not yet) cyclists, nevertheless, I had many joyful moments during the last years because of you. You enrich my life a lot by sharing the most tasty food or your perspective on the world. Iñaki, mil esker por introducirme a full a la cultra vasca y por tantas kañas juntas! Daniel, your company is always so much fun and you bring on the most interesting discussions! Thanks for sharing so much of your perspectives on science and academia with me. Und auch für viele tolle Festivals, Wanderungen, Essen oder Radtouren. Ich freue mich schon auf das nächste Mal, wenn wir potentielle Energie in Spaß umwandeln!

Another group of people, without whom this Thesis would not exist, are all the great and brilliant people that I worked with on "my" STM Milano. Li, you taught me incredibly well, how to drive Milano. Thanks for all the productive measurements, stimulating discussions and late-evening preparations for baking to Nestor, Jeremy, Alessio, Fran, Lorenz, Naroa and Fabian. Although not in Milano, still we shared countless hours in labs next to each other or fighting with the ATL. Thanks for all your help and advice Carmen, Javi, David, Reyes, Martina, Dimas, Djuro, Xabi, Rolf, Andrea, Danilo and Mikel. Yvonne, your comments and guidance improved my outreach activities a lot.

During the PhD I had the pleasure to get to know the beautiful Strasbourg. A big merci beaucoup to Guillaume, for being so welcoming, for your scientific advice, for not believing me and making me check the data over and over again until the last uncertainty is removed and for guiding me to the greatest cycling roads. Thanks a lot to Anna for everything you have taught me about STML. I learned so much during so little time, because you did an incredible job in teaching me. Tomas, you were most patient with me, when I asked the same questions over and over again and did not mind explaining another time. The stay would not have been the same without the many discussions (sometimes closer to STML, sometimes further away) over coffee. For that, I want to extend the merci beaucoup to Luis, Kiril, Fabrice and Virginie.

An important part of this Thesis is based on a incredibly fruitful colaboration with Pedro. You provided me with so many answers and so much more questions. I understand a big part of the things presented here thanks to your work and your effort to explain it to me. This is true also for Sofia who spent so much time explaining me the simplest

things in the Hubbard code. Countless hours of heated debates about topology shaped this Thesis, which would not have been possible without the everlasting interest from Thomas, Dani and Aran.

Der direkte wissenschaftliche Einfluss ist vielleicht etwas geringer, aber von meiner Familie habe ich immer Unterstützung dafür erhalten, zu forschen — von meiner Erziehung während der Kindheit und Jugend, bis hin zur Doktorarbeit im Ausland. Danke Papa, dass Du stets meine wissenschaftliche Neugier geweckt hast! Mama, dank Dir für all die kleinen und großen Dinge, die mir die Sicherheit geben, dass ich erreichen kann, was ich mir vornehme und dass ich immer auf Dich zählen kann. Vielen Dank für Deine große Neugier an meiner Arbeit und Dein Vertrauen in mich. Vielen Dank auch Dir, Margret, für Deinen unerschütterlichen Glauben an meine wissenschaftliche Karriere.

Sabi, mi vida y esta tesis no serían las mismas sin tí. Muchísimas gracias por tanto apoyo que me das (especialmente durante el tiempo en cual pasé más tiempo escribiendo la tesis en nanoGune que en casa). Muchísimas gracias porque reafirmas mucho mi pasión por la ciencia. Gracias por siempre ser tan comprensiva con las dinámicas complejas que impone el sistema académico a mi vida. Aprendo tanto de tí, y me abres muchas nuevas perspectivas al mundo que sin tí no tendría. Me emociona muchísimo que nos hemos atrevido a la aventura de crear una vida nueva juntas! Und obwohl ich Dich bisher nur in schwarz-weißen Ultraschallbildern gesehen habe, Du bist eine unglaubliche Motivation für mich, dazu beizutragen, die Welt ein kleines bisschen besser zu machen, liebe Tochter.

Contents

Introduction

The invention of the scanning tunneling microscope was a fundamental milestone for the experimental access to atomic scale objects, as it is honored in the explanatory statement of the Nobel prize awarded for its invention[1]. Its ability to generate real space images of nanometersized objects attracted the attention of many scientist since. First experiments focused on the study of pristine metal surfaces. Later, individual molecules absorbed on a metal surface came into experimental reach by cooling the microscope to cryogenic temperatures. The thermal diffusion of molecules is suppressed at few Kelvin, enabling the precise characterization by scanning tunneling microscopy (STM). Spectroscopic measurements, characterizing the electronic structure of the sample, benefited as well from the reduced thermal broadening of the electron's Fermi distribution at low temperature. It allowed detailed studies of low-energy excitations like spin-excitations or vibrations.

The experimental capabilities of the scanning tunneling microscope go beyond the pure observation of the sample. One can actively arrange individual adatoms and molecules on the metal substrate creating complex quantum architectures by a simple and controlled procedure. The metal tip of the scanning tunneling microscope behaves almost like a finger on the nanoscale, allowing to drag, push or pull the quantum objects. Giving access to the atomic scale quantum properties of matter, both in a sense of characterization and of manipulation, the low-temperature scanning tunneling microscope has become a widely used tool of modern experimental condensed matter physics, despite it being a highly demanding technique.

Addressing an individual molecule electronically would allow to use its intrinsic quantum properties for information processing. This idea dates back almost 50 years, when Aviram and Ratner[2] envisioned to replicate

the function of a macroscopic diode in a single molecule by a careful composition of different chemical moieties. Since then, various single molecule electronic devices were realized[3–10]. However, single-molecule spintronic devices[11] are scarce. Experiments on single molecule devices lack a clear control on the molecular position between and the contacts to the electrodes. Information on the behaviour of individual objects is only obtained from statistical analysis in large-area devices[12–14], restricting the possibility to study atomistic processes in the electronic transport.

This limitation is overcome in this Thesis by performing two-terminal transport experiments in a low-temperature scanning tunneling microscope. Its imaging capability allows us to specifically target the most reactive moiety for forming the tip-molecule contact[15]. The mechanical stability of the tunneling junction enables us to suspend the molecule between tip and substrate in a two-terminal transport configuration with well defined contacts to both electrodes, creating highly reproducible experimental conditions. Temirov *et al.*[15] pioneered this technique by measuring the Kondo coupling strength of a single molecular spin in two-terminal transport experiments. Shortly after, the procedure was applied by Lafferentz *et al.*[16] to investigate the precise atomic scale characteristics of electronic conductance through several nanometers long, non-rigid polymers, containing hundreds of atoms.

The overlap between the molecule's and substrate's electron wave function is lowered in the molecular segment that bridges tip and substrate resulting in a direct correlation between the conductance through a molecular wire and its electronic states[17]. In fact, the reduced hybridization enables access to the individual molecules' intrinsic quantum properties that are quenched in the adsorbed molecule. For example, Reecht *et al.*[18] showed that suspending polythiophene polymers between tip and substrate of a scanning tunneling microscope, the lifetime of the excited electronic state becomes large enough, that decay channels involving photon emission become relevant and electroluminescence of the individual polymer can be investigated.

Graphene nanoribbons (GNRs), quasi-one-dimensional stripes of sp^2-hybridized carbon, constitute a prime candidate to probe spin phenomena in such transport experiments. One can control the GNRs' electronic band structure and spin polarization by a careful choice of their atomic structure. For example a seven atom wide GNR with a zigzag edge is

metallic, while a seven carbon atom wide GNR with an armchair edge has a large band gap[19]. The seven atom wide armchair GNR is topologically non-trivial[20] creating spin polarized edge states at its termini. Extending its width to nine carbon atoms creates a topologically trivial ribbon. As a consequence, ribbons that alternate between seven and nine atom wide segments host a series of topologically protected edge states[20,21].

Top-down fabrication methods are not precise enough to control the shape of graphene nanoribbons at the atomic level. Grill *et al.*[22] and Cai *et al.*[23] provided in their seminal works a bottom-up route to synthesize atomically-precise graphene nanoribbons reliably. Small molecular precursors are deposited on a noble metal surface and polymerized by thermal activation of an Ullmann-coupling-like reaction. In a second step at higher temperature, the graphene nanoribbons are formed by planarizing the polymer through a cyclodehydrogenation reaction. Their publications were followed by the search for different molecular precursors, suitable for creating the desired atomic configuration tailoring the ribbon's electronic bands[24,25] or spin polarization[21,26]. For the integration of GNRs into spintronic devices, detailed studies of their transport properties, especially focusing on their intrinsic low-bias spin excitations are needed.

In this Thesis I tackle the decoupling and lack of transport experiments simultaneously by suspending individual spin hosting graphene nanoribbons between the tip and sample of a scanning tunneling microscope in a two-terminal transport configuration. Early work on suspended GNRs[17,27] focused on the electronic band structure, neglecting the ribbons' potential to host spin-polarized states.

Here, spin hosting states in the decoupled segments of suspended GNRs are accessed using currents of either co-tunneling or ballistic electrons. Fingerprints of atomic-scale magnetism are detected in spectroscopic conductance measurements over a large range of tip-substrate separations, showing example cases of spin manipulation. The spins are embedded in the interior of the GNRs, resulting in an increased chemical stability as compared to ribbons hosting spin-polarized states at their edges or open-shell graphene nanoflakes.

This Thesis is distributed in the following Chapters:

CHAPTER 1 introduces essential methods, techniques and concepts used in this Thesis. It starts by discussing key aspects of the scanning tunneling microscope, especially its ability for mechanical manipulation of individual molecules which is used to reach the two-terminal transport configuration. The graphene nanoribbon are produced in a bottom-up approach *via* on-surface synthesis strategies. This technique is introduced with a focus on the Ullmann-like coupling and cyclodehydrogenation reaction. To conclude the experimental part of this Chapter, the experimental setup is presented.

Next, the reader is familiarized with key aspects of electronic transport, discussing the double barrier system, as well as, differences between the co-tunneling and resonant tunneling regime. The Chapter continues by presenting the three families of graphene nanoribbons probed in the transport experiment of this Thesis. A special focus is placed on the topological classification of GNRs, as this is the origin of rich spin physics in one family of the investigated ribbons. The Kondo effect is vital to experimentally probe atomic scale magnetism. The Chapter discusses its origin and characteristic fingerprint in scanning tunneling spectroscopy. The Chapter is completed by the presentation of the mean-field Hubbard model, which approximates the π electron system of graphene nanoribbons in a single-particle Hamiltonian, allowing to simulate the spin physics of the large graphene nanoribbons investigated in this Thesis in computationally cheap calculations.

CHAPTER 2 studies resonant transport through 7aGNRs suspended between tip and sample of a low temperature scanning tunneling microscope. Substitutional doping with two boron atoms induces a localized state at the dopant position, creating a double barrier configuration that enables bipolar transport through the occupied boron state. Furthermore, the boron state quantizes the valence band resulting in quantum well states that create a diode-like behaviour.

CHAPTER 3 reports on the magnetic character of the boron induced state by studying its Kondo physics in the suspended configuration. We show that the state emerges by inhibiting the propagation of electrons travelling in the topologically non-trivial valence band of the seven armchair graphene nanoribbon.

CHAPTER 4 reports results of suspended borylated ribbons. In particular, we found that a spin polarized end state emerges at th boundary between the suspended and the adsorbed segments of a ribbon with dense boron doping. This spin state was unexpected for borylated GNRS and its origin is explained by considering that the topological phase of the valence band of suspended and adsorbed ribbons is apparently different.

CHAPTER 5 analyzes a nanoribbon family that combines a spin-polarized flat band and a dispersive transport band crossing the Fermi level. The ribbons simultaneously permit ballistic electron transport at few mV over several nanometers and exhibit a stable Kondo resonance in a single transport experiment.

CHAPTER 6 shows the possibility of addressing the spin of a functional unit embedded in a hybrid structure combining a chiral graphene nanoribbon and an iron-porphyrin molecule. We find a renormalization of the magnetic anisotropy by charge fluctuation in one type of the Fe-porphyrins.

CHAPTER 7 concludes the Thesis by summarizing the research and presenting a short outlook to future work.

1 Experimental Techniques and Physical Concepts

The experimental work of this Thesis was performed using a scanning tunneling microscope held at $\sim 5\,\mathrm{K}$ to analyze samples prepared *in situ* by on-surface synthesis techniques under ultra-high vacuum (UHV) conditions. The combination of these techniques allows us to characterize atomically precise graphene nanoribbons in real space by scanning tunneling microscopy (STM), their band structure and magnetic excitations by scanning tunneling spectroscopy (STS), as well as the mechanical manipulation of graphene nanoribbons using the tip of the scanning tunneling microscope. Suspending the ribbon between tip and substrate removes the hybridization between molecular states and substrate and gives access to the unperturbed electronic states of the molecule in a two-terminal transport configuration.

In the following, I will first present the tool set provided by the scanning tunneling microscope. I will restrict the discussion here to the aspects most relevant for this Thesis, as STM and STS are well established techniques with excellent comprehensive literature available[28]. The on-surface synthesis is introduced, which is used to fabricate the investigated graphene nanoribbons (GNRs). The more experimental Section of the Chapter is closed by a presentation of the experimental setup.

In the second Section of the chaper, I will introduce physical concepts that are important in this Thesis. I will start by a discussion of different electronic transport regimes through molecular wires, especially in a double barrier configuration. An overview over graphene nanoribbons is given, with a focus on the three GNRs investigated in this Thesis, followed by the concept of topology applied to GNRs. Next, the Kondo effect, providing the key experimental fingerprint for the detection of

atomic scale magnetism in this Thesis, is presented. The Chapter closes by introducing the mean-field Hubbard model, which is used to simulate the spin polarization of GNRs.

1.1 Experimental Methods and Systems

1.1.1 Scanning Tunneling Microscopy

Gerd Binnig and Heinrich Roher were awarded the Nobel prize[1] for the invention of the scanning tunneling microscope in 1986, only four years after their invention[29,30]. The scanning tunneling microscope exploits the quantum mechanical tunnel effect to characterize a conductive sample with atomic precision. For that, a metallic tip terminated in a single apex atom is placed in close proximity ($\sim 1\,\mathrm{nm}$) to the sample's surface using piezoelectric actors. The tunneling current depends exponentially on the separation z between tip and surface, which allows us to detect atomic scale changes of the surface. The exponential dependency follows from solving the time-independent Schrödinger equation for a plane wave penetrating into a rectangular energy barrier of finite width and finite height. This simplified picture describes the general tunneling process, but ignores physical boundary conditions set by the scanning tunneling microscope.

Bardeen[31] developed a model that describes the tunneling process in a metal-insulator-metal junction. First, the two sides of the tunneling junction (tip plus vacuum and vacuum plus sample) are treated separately. Their eigenstates, Ψ_tip and Ψ_sample respectively, are obtained from solving the time-independent Schrödinger equation. These states are used in a next step, to calculate the transitions between different states within time-dependent perturbation theory resulting in the transition matrix element

$$M_{fi} = \frac{\hbar^2}{2m} \int_\mathrm{S} \left[\Psi_{\mathrm{tip},i} \nabla \Psi^*_{\mathrm{sample},f} - \Psi^*_{\mathrm{sample},f} \nabla \Psi_{\mathrm{tip},i} \right] \, \mathrm{d}\mathbf{S}, \qquad (1.1)$$

where $\hbar$ is the reduced Planck constant, m the mass of the electron and S is an arbitrary surface separating tip and sample. The indices i and f indicate the initial and final state of the tunneling process.

The tunneling current is given by

$$I = \frac{2e}{\hbar} \sum_{i,f} |M_{fi}|^2 \delta(E_f - E_i), \tag{1.2}$$

where e is the electron charge and E_f and E_i the energies of the final and initial state. The appearing delta function assures conservation of energy, *i.e.* tunneling is an elastic process. The current can be calculated explicitly using Equation (1.1).

Equation 1.2 can be extended by introducing the density of states in tip and sample to calculate the transition matrix elements. In the limit of zero temperature, we obtain for a one-dimensional, rectangular energy barrier

$$I = \frac{4\pi e}{\hbar} \int_0^{eV} \rho_{\text{tip}}(\varepsilon - eV)\rho_{\text{sample}}(\varepsilon)T(\varepsilon, V, z)\,\mathrm{d}\varepsilon, \tag{1.3}$$

where V is the applied bias between tip and sample, ρ describes the electronic density of states and $T(\varepsilon, V, z)$ is the transmission factor. The transmission reduces exponentially with an increasing work function Φ of the metal. Importantly, this means that the main contribution to the tunneling current stems from electrons located at the Fermi level. For small bias $eV \ll \Phi$, the energy-dependent part of the transmission factor can be considered constant, leaving only an exponential dependence on z, as discussed above.

Equation 1.3 can be extended to finite temperatures by including two Fermi-Dirac distributions $f(E)$, accounting for the thermal excitations in tip and sample. The extended equation reads

$$I = \frac{4\pi e}{\hbar} \int_{-\infty}^{\infty} \{f(\varepsilon - eV) - f(\varepsilon)\}\, \rho_{\text{tip}}(\varepsilon - eV)\rho_{\text{sample}}(\varepsilon)T(\varepsilon, V, z)\,\mathrm{d}\varepsilon. \tag{1.4}$$

While this equation accounts accurately for energy dependence of the tunneling process and the density of states in tip and sample, it neglects spatial information.

Tersoff and Hamann extended the model[32] to account for spatially resolved tunneling at small V. Starting from Equation 1.2, they calculated the matrix elements M_{if} explicitly assuming an s-wave orbital for the tip

and a plane wave Fourier expansion for the surface. These approximations lead to

$$I \propto \rho_{\text{sample,TH}}(E_{\text{F}}, \boldsymbol{r}_{\text{t}}), \tag{1.5}$$

with $\rho_{\text{sample,TH}}(E_{\text{F}}, \boldsymbol{r}_{\text{t}})$ being the *local* density of states of the surface evaluated at E_{F} and the position of the tip $\boldsymbol{r}_{\text{t}}$. Therefore, a single atom terminated tip can obtain local information about the surface with picometer precision.

Imaging Modes

To record an image, the tip scans the xz-plane. The movement of the tip with picometer precision is controlled *via* piezoelectric crystals. In the "constant current" mode, a feedback loop controls the elongation of the z-piezo crystal to maintain the current at a constant value in the order of picoampere. The tip's movement is translated to a topographic image of the surface.

The constant current mode is used for samples with a strong three dimensional character, for example the simultaneous imaging of isolated molecules and the underlying metal surface. Although such images contain precise information about the location of the molecules, the obtained height does not reflect the real atomic height but is convoluted with the chemical information encoded in $\rho_{\text{sample}}(\varepsilon)$ in Equation 1.3. For example, CO molecules on Ag(111) appear as depressions when imaged at low bias, even though the molecule absorbs with its atoms above the atoms of the surface plane.

An alternative to the constant current imaging is the so called "constant height" imaging, where the tip scans the xy-plane while the feedback is switched off. The information about the surface is now encoded in the flowing current.

Bond Resolved Scanning Tunneling Microscopy

The constant height mode is especially important to unravel the atomic structure of planar, organic molecules. The presence of small molecules in the junction between tip and substrate enhances the contrast resolved in STM[33]. Covalent electron bonds appear as sharp lines of high current against a dark background. One can exploit this mechanism to obtain

bond-resolved images using a CO-functionalized tip (CO-tip), *i.e.* a tip that has a single CO molecule attached to its apex atom[34,35] with the carbon atom forming the tip-CO bond and the oxygen atom sitting closer to the substrate (for tip functionalization see Section 1.1.3). Images are scanned at small tip substrate separation and very low bias ($\sim 1-5\,\mathrm{mV}$). The contrast is improved by three basic principles:

First and most importantly, the Pauli repulsion between CO and electron bonds inside the molecule deflects the CO towards regions of lower electron density[36–38]. For example, while scanning above the benzene rings of a pentacene molecule, the CO is deflected towards their center, resulting in a low conductance most of the time. Only in few positions exactly above the covalent $C-C$ bonds, the lateral relaxation is not enough for the oxygen apex to reach the low-conductance center of the benzene ring and an increased conductance is observed. The difference between apparent apex position (as determined by the voltage applied to the piezo crystals) and the real apex position (due to lateral relaxation of the CO) increases the sharpness of features observed in the STM images.

Second, the tunneling current involves the convolution of the *p*-wave character of the CO with the sample LDOS[39]. The convolution is especially important to consider, if molecular orbitals are mapped. Third, changes in the DOS due to the presence of CO in the junction need to be considered for a complete description[40]. A detailed discussion of the different effects and their interplay is given by Jelinek in[41].

1.1.2 Scanning Tunneling Spectroscopy

Scanning tunneling spectroscopy gives a direct access to the energy dependence of the LDOS *via* the experimentally available $\mathrm{d}I/\mathrm{d}V$ signal. STS allows us to identify molecular orbitals and spin-related phenomena that present a characteristic fingerprint in the LDOS, like the Kondo effect (see Section 1.2.4). Combining STS with STM gives access to the spatial distribution of the orbitals.

An analytic expression connecting the LDOS to the $\mathrm{d}I/\mathrm{d}V$ is derived by differentiation of Equation 1.3 with respect to V

$$\frac{\mathrm{d}I}{\mathrm{d}V} \propto e\rho_{\mathrm{tip}}\rho_{\mathrm{sample}}(eV)T(eV,V,z) + \int_0^{eV} \rho_{\mathrm{tip}}\rho_{\mathrm{sample}}(\varepsilon)\frac{\partial T(\varepsilon,V,z)}{\partial V}\,\mathrm{d}\varepsilon,$$

(1.6)

where a constant ρ_{tip} is assumed. According to this expression, structural features observed in the differential conductance plot can be attributed to the sample LDOS. The transmission factor T depends exponentially on V, which adds a monotonic background to the $\mathrm{d}I/\mathrm{d}V$ signal.

The differential conductance is obtained using a lock-in amplifier. A small, sinusoidal AC modulation with amplitude V_{M} and frequency ω is applied to the DC voltage V_0 of the scanning tunneling microscope. The bias' modulation translates to a modulation of the current that, for small V_{M}, can be expressed in a Taylor expansion[28]

$$
\begin{aligned}
I(t) =&\, I(\,V_0 + V_{\text{M}}\sin\omega t\,) \\
\approx&\, I(V_0) + V_{\text{M}}\sin\omega t\,\frac{\mathrm{d}I(V)}{\mathrm{d}V} + \frac{V_{\text{M}}^2}{4}\sin 2\omega t\,\frac{\mathrm{d}^2 I(V)}{\mathrm{d}V^2} + \text{h.o.}
\end{aligned}
\tag{1.7}
$$

The higher order contributions of V_{M} contain harmonics in the form

$$
\text{h.o.} \sim V_{\text{M}}^n \sin n\omega t\,\frac{\mathrm{d}^n I}{\mathrm{d}V^n}\,,
\tag{1.8}
$$

with n being a natural number. In this expansion, higher order terms in V_{M} were omitted for each harmonic.

The lock-in amplifier multiplies the current by the AC modulation and integrates the resulting signal. In leading order, only AC components of the current with the frequency of the bias modulation survive the integration due to the orthogonality of the harmonics of a sine function. The resulting signal is proportional to the real $\mathrm{d}I/\mathrm{d}V$ signal up to a constant scaling factor. Higher order derivatives of the current can be accessed by multiplying the current with the corresponding harmonic of the AC modulation in the first step. A direct numerical differentiation of the I-V-signal is also possible, but often results in higher noise compared to a lock-in amplifier.

1.1.3 Mechanical Manipulation of Individual Molecules

Apart from microscopy and spectroscopy, the tip of a scanning tunneling microscope can be exploited to manipulate matter at the atomic scale. Individual adatoms can be positioned with atomic precision by controlled manipulation with the tip[42]. The combination of van der Waals and
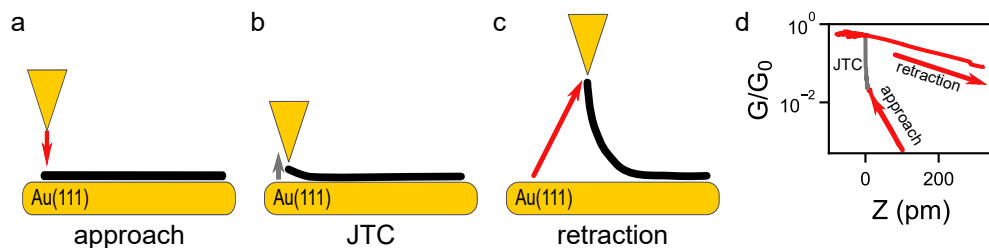
Figure 1.1: Lifting a molecule to create a two-terminal transport device: a The tip is approached at low bias towards the reactive moiety. **b** The tip-molecule bond forms in a sudden event, sometimes called "jump-to-contact". In this Thesis, this point defines the 0 on the z axis. **c** The tip is retracted, lifting the molecule partially from the substrate. **d** The low-bias conductance allows to monitor the different stages of the retraction process. During the approach, the current increases exponentially. The jump-to-contact is characterized by a sudden sharp rise in conductance. Upon retraction, the current is increased compared to the approach curve, indicating the lifting of the molecule.

electrostatic forces between tip and adatom is sufficient to drag or push individual atoms from one absorption site to another. Such, it is possible to build atomically precise nanostructures and study their physics[43]. The procedure is easily extended to small molecules like CO[44,45] and even large molecular structures[46].

The control over individual molecules goes beyond lateral manipulation in the surface plane. Out-of-plane manipulation becomes feasible by forming a bond between tip apex and a reactive moiety of the molecule[15]. To lift a molecule, the tip of the scanning tunneling microscope is stabilized above the reactive moiety and approached towards the surface at low bias. A sketch of this situation is provided in Figure 1.1a. Initially, the tunneling current increases exponentially, as the tip-surface separation z is reduced. A sudden increase in the conductance, often referred to as "jump to contact", indicates the formation of a tip molecule bond (Figure 1.1b).

Retracting the tip after contact formation lifts the molecule partially from the surface (Figure 1.1c) and thus forms a molecular wire bridging tip and substrate. In some cases, a pure retraction in z without any lateral movement is sufficient to lift the molecule. However, optimal lifting efficiency is reached following a trajectory involving lateral tip movement[47]. The trajectory needs to be customized for each molecule. Trajectories minimizing the lateral movement of the molecule over the

13

surface show the highest success rates. For this Thesis this implies lifting trajectories along the GNR's backbone, if projected onto the substrate plane.

The success of the lifting process is monitored by observing the conductance through the tip-molecule-substrate junction. If the molecule is lifted, the conductance is significantly increased as compared to identical tip-sample separation before contact formation (Figure 1.1d). The orbitals of the lifted molecule open additional channels for electrons tunneling from tip to substrate resulting in the increased conductance (see also Section 1.2.1).

The electronic hybridization between substrate and molecule is reduced in the free-standing segment of the molecule[15,16] and two-terminal transport experiments probing the pristine properties of the molecule are possible[17]. Long, one dimensional molecules like graphene nanoribbon can be dragged laterally[48] to move them onto ultra-thin insulators like NaCl[49]. The NaCl electronically decouples the molecule from the substrate permitting us to spatially resolve the unperturbed electronic structure of the ribbon. It is even possible to balance organic molecules with an extended π electron system in a fragile, meta-stable, upright configuration "on their edge"[50].

Tip Functionalization

Small molecules can detach easily from the surface and stick only to the tip. If the molecule absorbs in a well-defined position, the tip becomes functionalized. CO-functionalized tips to visualize the atomic structure of molecules are discussed in detail above under **Bond Resolved Scanning Tunneling Microscopy** in Section 1.1.1. Apart from the atomic structure, appropriate tip functionalization allows the measurement of the local density of states[51], molecular vibrational modes[52], electrostatic surface dipole moments[53,54] or magnetic phenomena[55]. Tip functionalization, especially CO-functionalization to determine the atomic structure of molecules, has become a standard tool in every STM and STS group.

1.1.4 On-Surface Synthesis

On-surface synthesis (OSS) strategies extend the classical toolbox of in-solution chemistry to fabricate large molecular nanostructures that were

previously impossible to synthesize. In OSS, molecular precursors are deposited under UHV conditions onto an atomically flat metal surface, followed by the thermal or tip-induced activation of one or more chemical reactions. Importantly, the geometrical confinement into a plane combined with the presence of a catalytically active metal enables reaction pathways, which are in some cases inaccessible to in-solution chemistry[56]. Since OSS is performed under UHV conditions, it enables the straightforward characterization and analysis with surface-science techniques, including STM and STS.

Hla *et al.*[57] showed the possibility to induce a chemical reaction by electron-induced activation or bond breaking. They performed each of the necessary reaction steps of the Ullmann-coupling[58] — dissociation of the halide, diffusion of the phenyl rings towards each other and chemical association to form biphenyl — in a sequential manner using the tip of a scanning tunneling microscope. Furthermore, the tunneling current-induced dehydrogenation of organic molecules is feasible[59]. An Ullmann-like C–C coupling and a dehydrogenation reaction are the necessary steps to form the GNRs presented in this Thesis. However, the step-by-step OSS is mostly restricted to works studying the reaction pathway itself[60,61] or the site selective creation of π radicals in graphene nanostructures[62].

Table 1.1: Substrate temperatures: Substrate temperatures used in the sample preparation to induce the reaction steps of Ullmann-like coupling (UC) and cyclodehydrogenation reaction (CDH).

	Chapter	UC (°C)	CDH (°C)
2B-7aGNR	2–4	200	400
2B-575-aGNR	5	250	300
FeTPP-chGNR hybrid	6	200	250

In this Thesis, the on-surface reactions creating the graphene nanoribbons are activated thermally. Submonolayers of the molecular precursors were deposited on the clean Au(111) substrate held at room temperature. A first annealing step induces an Ullmann-like C–C coupling polymerizing the molecular precursors[22]. In a second step, the polymeric chains are planarized at higher temperature[23] *via* the so-called cyclodehydrogenation (CDH). The CDH is a C–C coupling reaction, which closes the carbon rings of the graphene honeycomb lattice under dissociation of two hydrogen atoms.
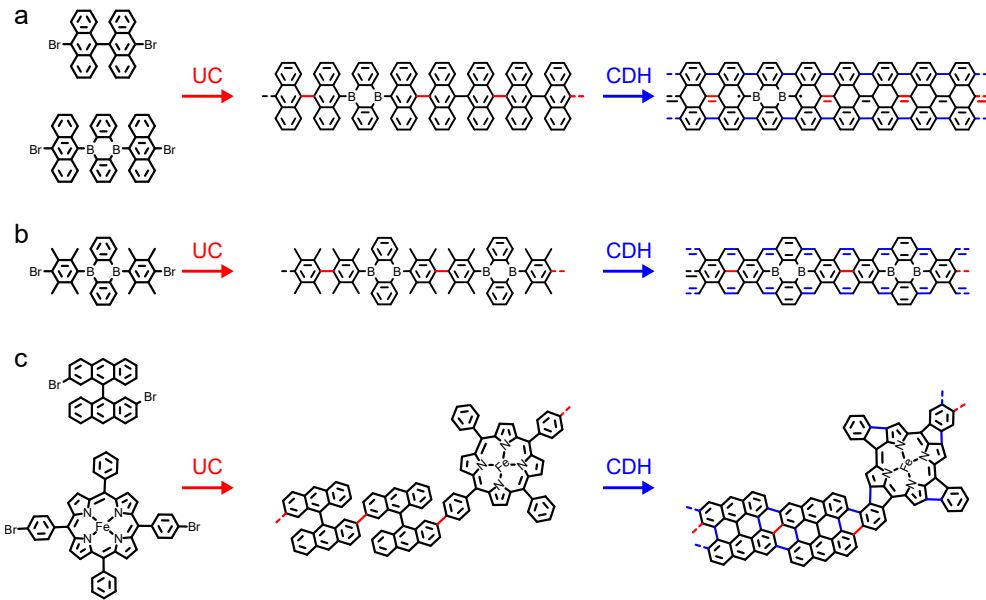
Figure 1.2: **Molecular precursors and envisioned synthesis route for the investigated nanoribbons: a, b, c** Lewis structures of (left to right) the molecular precursors, the Ullmann-coupled polymer and the planar GNR corresponding to the ribbon used in Chapter 2–4 (**a**), Chapter 5 (**b**) and Chapter 6 (**c**). Submonolayers of the molecular precursors were codeposited on the sample held at room temperature before the thermal activation of the reaction steps.

Different precursor molecules were needed to prepare the GNRs investigated in this Thesis (see Figure 1.2). If two molecular precursor were needed for the on-surface synthesis, both molecules were co-deposited on the cold substrate before the first annealing step inducing the Ullmann-coupling. The respective temperatures used for the thermal activation of the reaction are listed in Table 1.1.

1.1.5 Experimental Setup

The experiments presented in this Thesis were performed inside a custom-built ultra-high vacuum (UHV) chamber with a base pressure of $p < 10^{-10}$mbar. Figure 1.3a presents a picture of the system. The substrate for on-surface synthesis of the graphene nanoribbons is a polished gold single crystal cut to the Au(111) surface. It was obtained from MaTeck GmbH and prepared *in situ* by sputtering the gold surface with Ne$^+$ ions,
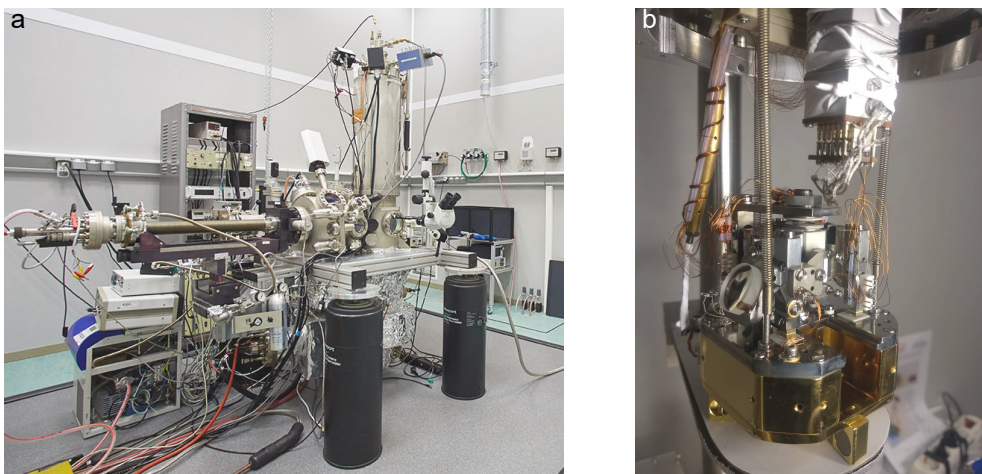
Figure 1.3: Laboratory and Slider Head: a,b Picture of the UHV low-temperature scanning tunneling microscope system and CreaTec slider head used in this Thesis.

followed by thermal annealing *via* resistive or electron beam heating. Substrate temperatures were controlled using a thermocouple in close proximity to the gold crystal.

Precursor molecules were provided by collaborators from the group of Diego Peña as highly purified crystalline powders, with the exception of trans$-Br_2FeTPP(Cl)$ (Chapter 6, commercially obtained from PorphyChem SAS), and further purified by thermal purification inside the UHV chamber. The precursor molecules were evaporated directly onto the cleaned gold substrate using a commercial four pocket molecular beam evaporator from Dodecon Nanotechnology GmbH. Evaporation rates were controlled before sample preparation using a quartz microbalance placed in the molecular beam.

Samples were transferred *in situ* into a scanning tunneling microscope head, held at $T \approx 5\,\mathrm{K}$ by a thermal shield connected to a liquid helium bath cryostat. The whole unit was surrounded by a second thermal shield connected to a liquid nitrogen bath cryostat. The scanning tunneling microscope head is suspended on three springs inside the liquid helium shield to reduce high frequency vibrations. Low frequency vibrations are damped by resting the complete UHV chamber on pneumatic feet from Newport. A further reduction of mechanical vibrations is achieved by eddy current damping of the inner shield and head.

The experiments presented here were performed using two different scanning tunneling microscope heads. The experiments presented in Chapter 5 were performed using a slider head from CreaTec Fischer & Co GmbH (CreaTec) (Figure 1.3b) controlled *via* the Nanonis Real-Time Controller RC5 and the Nanonis software package, both from SPECS Surface Nano Analysis GmbH. The other experiments were performed on a CreaTec inverted beetle type head controlled *via* the CreaTec STMAFM software in combination with a CreaTec STMAFM Control 3 unit. An external Stanford Research Systems SR830 lock-in amplifier was used to acquire STS data. Standard parameters are a modulation frequency $f = 760\,\mathrm{Hz}$, a modulation amplitude of $V_{\mathrm{RMS}} = 2$ to $20\,\mathrm{mV}$ and a time constant $\tau = 10\,\mathrm{ms}$. A home-built passive voltage divider (1/10) was used to resolve the low-bias features with increased precision in some measurements.

Custom programs for lifting the graphene nanoribbons were programmed in Python and LabView to interface the STMAFM and Nanonis software, respectively. STM and STS data was processed using WSxM[63] and the python matplotlib libary[64]. Color maps use perceptual continuous color scales[65].

1.2 Concepts

1.2.1 Electronic Transport Through Molecular Wires

In STM, molecules are typically absorbed on the metallic substrate. The molecular orbitals are hybridized with the states of the metal and well separated from the tip. Molecules used for tip functionalization hybridize with the electronic states of the tip, but remain well separated from the substrate's state. In either configuration, the molecular orbitals are hybridized with one electrode and well separated from the other. All voltage applied to the junction drops over a single tunneling barrier.

Molecules on ultra-thin insulators[49,66] investigated by STM are decoupled electronically from substrate and tip, resulting in a double tunneling barrier configuration. The molecule in the junction provides isolated orbitals for electronic transport from tip to substrate. These states divide the tip-substrate tunneling barrier into one tip-molecule and one

molecule-substrate tunneling barrier. This situation is depicted in Figure 1.4a. In such a double barrier configuration a fraction α of the total applied bias voltage V drops over the tip-molecule barrier. Correspondingly the fraction $(1 - \alpha)$ drops over the molecule-sample barrier. Importantly, the molecular levels now shift with respect to the Fermi levels of both electrodes. For particular situations this can result in electronic transport through the same molecular level independent of polarity of the applied voltage. This is referred to as bipolar transport.

A second case that in general requires the description in a double barrier configuration are molecular wires. Molecular wires are molecules that are suspended in a free standing configuration between two electrodes and, therefore, can hybridize with both equally.

Example cases for this scenario are molecules in break junction experiments where the molecules are in covalent contact with both electrodes[67] or molecules suspended between the tip and sample in a scanning tunneling microscope[15,16].

The electronic transport through a double barrier system is divided into the regimes of co-tunneling, resonant tunneling and sequential tunneling[68]. I will focus on their application to a scanning tunneling microscope. Figure 1.4b–d depicts a sketch of the three different situations. The co-tunneling regime describes electronic transport at low bias (Figure 1.4b) *via* tunneling events. In this regime, the conductance G through the molecular wire suspended between tip and sample reduces exponentially with its length z

$$G(z) = G_0 e^{-\beta z} \tag{1.9}$$

with the prefactor G_0 and the decay constant β. The value of G_0 is determined by the precise atomic configuration of the tip-molecule bond and the spatial overlap between molecular and tip orbitals[69,70].

The decay constant β depends on the full electronic structure of the molecular wire[71,72]. Second order co-tunneling processes open an electronic transport channel in the energy window between the Fermi levels of tip and substrate[73] resulting in $\beta < \beta_0$ with the vacuum tunneling decay constant β_0. The partial hybridization of the molecular wire with the metallic substrate results in a broadening of the molecular orbitals (indicated by the blue lines in Figure 1.4 reducing β further.

We reach the regime of resonant tunneling, when the bias is increased sufficient for a molecular orbital to lie inside the transmission window be-
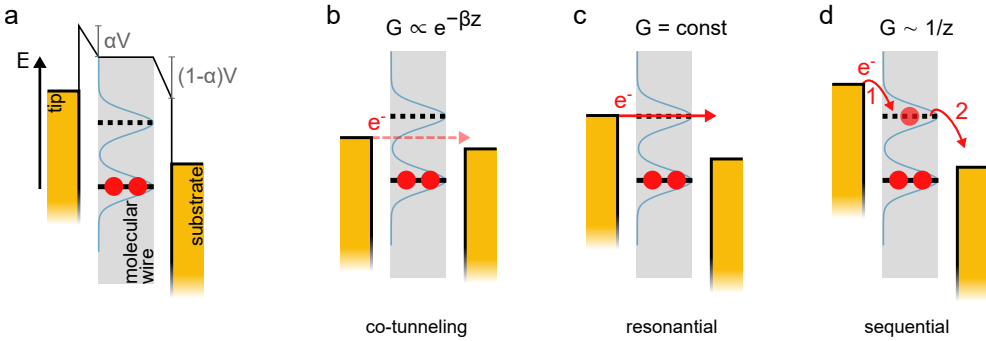
Figure 1.4: The three transport regimes through a double tunneling barrier: a Sketch of a double barrier configuration with a molecular wire in the junction between tip and substrate. The fraction α of the applied bias V drops over the tip-molecule barrier. Correspondingly, the fraction $(1-\alpha)$ drops over the molecule-substrate barrier. Note, that in the double barrier configuration the molecular levels shift with respect to both electrodes. **b** Sketch of the co-tunneling regime. No molecular level is located in the transport window between the two Fermi levels. Second-order processes enable additional tunneling channels through the molecular wire. The regime is characterized by an exponential decay of conductance. **c** Sketch of the resonant tunneling regime. A molecular level lies inside the transport window. Electrons can tunnel in a single coherent process from tip to substrate. The conductance becomes independent of the length. **d** Sketch of the sequential tunneling regime. A molecular level lies inside the transport window, but the transmission through the tunneling barriers is low. Electrons move in two incoherent tunneling events from tip to substrate. The conductance depends only weakly on the length of the molecular wire.

tween the respective Fermi levels of tip and sample[74] (Figure 1.4c). First we assume a high electron transmission through the tunnel barriers. For low electron transmission we reach the regime of sequential tunneling discussed later. In the resonant tunneling regime, the molecule couples strongly with the electrodes and a coherent state spanning from tip through molecule into the substrate forms.

Resonant electron tunneling from tip to substrate (or vice versa depending on the bias) is characterized by $\beta = 0$, meaning

$$G(z) = \text{const}, \tag{1.10}$$

i.e. ballistic electron transport through the molecular wire. In experiments, a finite curvature of the molecular wire can result in a finite β even under resonance conditions[17]. The associated current through the molecular wire is largest, if the molecular orbital aligns with the upper

Fermi level. If the orbital is tuned to a lower position in the transmission window, a reduced electron transmission through the barrier reduces the current. Nevertheless, we remain in the resonant transport regime as long as the electrons tunnel in a coherent process from tip to substrate.

The third regime, transport *via* sequential tunneling, describes the electron transport through a molecular orbital in the transmission window, if coupling to the leads is weak, *i.e.* the tunneling transmission through the barriers is low[75,76] (Figure 1.4d). In the sequential transport regime, electrons tunnel into the orbital and leave the orbital in a second, independent tunneling process after a finite lifetime in the molecule.

As the electron resides a finite lifetime in a real (charged) molecular state, the observed transport gap is increased with respect to the band gap of the neutral molecule[49]. Sequential transport is non-coherent. It depends only weakly on z, showing linear resistance in some cases $(G \sim 1/z)$[77–80]. In scanning tunneling microscopy, sequential transport is important in the description of molecules placed on thin insulating layers[49,66], where the molecule is decoupled from tip and substrate.

All transport experiments presented in this Thesis probe coherent electron transport, *i.e.* co-tunneling or resonant transport, through single graphene nanoribbons suspended between tip and substrate of a low-temperature scanning tunneling microscope by means of mechanical manipulation (see Section 1.1.3). Access to the co-tunneling regime was feasible for all ribbons. The regime of resonant transport is investigated in Chapter 2, 5. Resonant transport could not be reached for all ribbons, as too high current or bias routinely resulted in a rupture of the tip-molecule bond, in some cases coinciding with a chemical decomposition of the molecule[81].

1.2.2 Graphene Nanoribbons

Graphene nanoribbons are narrow, quasi one-dimensional stripes of graphene, a monolayer of hexagonal sp^2-hybridized carbon atoms. The electronic confinement into one dimension results, in general, in a semiconducting system[82,83]. The ribbon's band gap is determined by its width and edge orientation[19,83–87], which follows one of the two high-symmetry directions of graphene (armchair and zigzag GNRs, blue and red in Figure 1.5a) or alternates between the two (chiral GNRs, purple
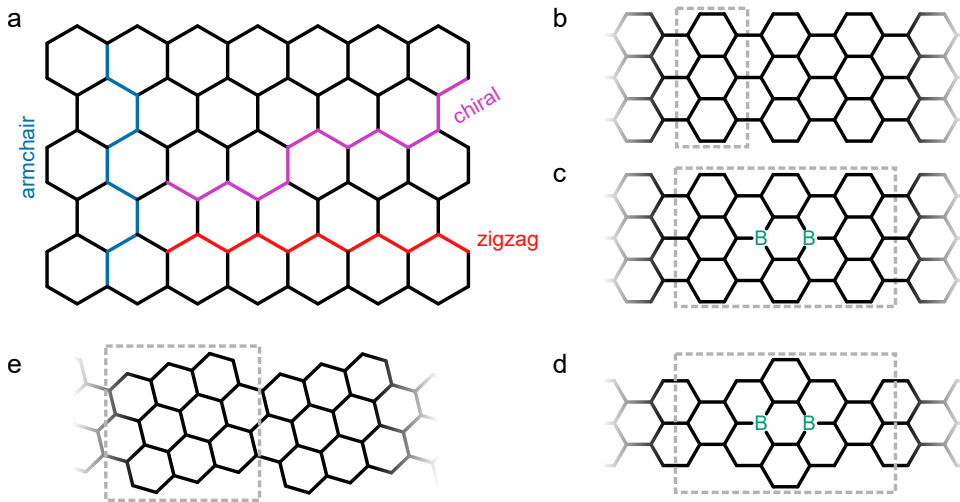
Figure 1.5: Graphene and graphene nanoribbons: a Graphene is formed by sp^2 hybridized carbon atoms that form a honeycomb lattice. Graphene nanoribbons, one dimensional narrow stripes of graphene are classified by their edge structure as armchair, zigzag or graphene nanoribbons. **b–e** Atomic structure of the different GNRs investigated in this Thesis and their respective unit cell (dashed, grey rectangle). **b** 7aGNR, **c** 2B-7aGNR, **d** 2B-575-aGNR, **e** (3,1)-chiral GNR.

in Figure 1.5a). GNRs inherit the high electron mobility of extended graphene, which makes them an interesting material for molecular spintronics. Apart from their low resistivity, graphene nanoribbon can also host spin polarized states.

Intrinsic π magnetism emerges in graphene nanoribbon, for example due to spin-polarized states at zigzag edges[83,84,88,89], topological protected edge states[20,21,26,90] (see Section 1.2.3) or functionalization with side groups[91]. Another route to induce spin-polarized states in graphene based nanostructures is to covalently fuse GNRs and spin-hosting organic molecules into hybrid nanostructures[92]. A detailed review of spin-polarized π electron systems in graphene nanostructures was recently published by De Oteyza and Frederiksen[93].

In this Thesis, the electronic transport through three types of GNRs is studied. Their synthesis and atomic structures are presented in Section 1.1.4. Chapters 2–4 are dedicated to seven carbon atom wide GNRs with subsitutional 2B doping[94,95] (2B-7aGNRs, Figure 1.5c). The boron doping creates in-gap states that are localized around the 2B-unit[96].

These states are connect to the topological character of the 7aGNR[20] (see Section 1.2.3). These 2B-states present the same wave function symmetry as the valence band (VB) of the pristine 7aGNR, blocking its free propagation inside the ribbon[97]. If a second 2B-unit is located in some distance to the first, the pristine ribbon's VB gets confined between the two 2B-units and quantum well modes of the band form[96,97]. For dense boron doping, the in-gap boron states merge into a non-dispersive band[97,98].

Chapter 5 discusses the electronic transport properties of a ribbon that is derived from a 2B-7aGNR with dense boron doping by reducing its width in the pristine anthracene units from seven to five carbon atoms. We find that this ribbon combines a spin-polarized flat band with a dispersive transport band crossing the Fermi level.

In Chapter 6 spin excitations in an iron porphyrin molecule are studied *via* charge injection through a chiral graphene nanoribbon (Figure 1.5e). For this, iron porphyrins and chiral GNRs are fused covalently to form a hybrid system[92]. The chrial ribbon used is a particularly well suited for the fabrication of hybrid devices due to the low substrate temperatures required in its OSS[99]. On Au(111), the ribbon's valence band lies close to the Fermi level[100], suggesting high co-tunneling rates, beneficial for the low-bias charge injection through the ribbon.

1.2.3 Topological Classification of Graphene Nanoribbons

The topological classification of a material associates a global invariant with the material's electronic bandstructure. The value of such an invariant is intrinsically connected to physical properties, for example the wave function symmetries of valence and conduction band. For one dimensional systems like graphene nanoribbons, the Zak phase γ was shown to be a useful topological number[101], that correctly predict the presence of zero-energy electronic states localized at the material's surface[102]. Materials that develop this so-called edge or boundary state at their interface to vacuum are called topological or topologically non-trivial.

The Zak phase of the nth electronic band is given by[101]:

$$\gamma_n = i \int_{\mathrm{BZ}} \mathrm{d}k \left\langle u_{nk} \left| \frac{\partial u_{nk}}{\partial k} \right. \right\rangle, \tag{1.11}$$

where BZ is the one dimensional Brillouin zone, k the crystal momentum and u_{nk} is the periodic part of the Bloch function of the nth band. The total Zak phase of the system is obtained by summing the γ_n of all occupied bands.

In general, it can be very challenging to calculate γ. However, for inversion symmetric systems, γ is quantized to 0 or $\pi \pmod{2\pi}$[101,103] and the Z_2 invariant can be calculated from

$$(-1)^{Z_2} = \prod_n \xi_n(\Gamma) \tag{1.12}$$

where $\xi_n(\Gamma) = \pm 1$ is the parity eigenvalue of the nth band at Γ and $\prod_n$ goes over all occupied bands. Note that n is necessarily even due to inversion symmetry of the system. The Z_2 invariant only takes the values of 0 and 1 and is related to the Zak phase via[20,104]

$$(-1)^{Z_2} = e^{i \sum_n \gamma_n}, \tag{1.13}$$

with $\sum_n$ over all occupied bands. It is evident that the evaluation of ξ_n is a lot simpler than the exact calculation of γ_n. The system is topological for $Z_2 = 1$ and trivial for $Z_2 = 0$. Cao $et.$ $al.$ give in[20] analytical formulas to directly calculate Z_2 for different types of armchair GNRs (aGNRs). The seven atom wide 7aGNR is topologically non-trivial. Dense 2B doping removes effectively one electron from the band structure, which results in a topologically trivial ribbon.

We can gain some intuitive understanding of the origin of the zero-energy edge state from the definition of the topological phase in Equation 1.12. For that, we consider a transition from a trivial to a topological material. In a trivial material, there is an even number of bands with odd parity, while in a topological material, the number is odd. The order of occupied bands is not important. We can imagine a continuous, adiabatic connection between the two systems, where an occupied band moves up in energy while an unoccupied band of opposite parity moves to lower energies. Importantly, the band occupation, and therefore the

Z_2 invariant, can only change, if at some point during the transformation the band gap closes, *i.e.* the system becomes metallic.

Connecting two materials of different topological character creates a sharp, but continuous transition between them and the above described topological transition occurs at their interface, implying the existence of a zero-energy state. One model system to study topological transitions and edge states is the Su, Schrieffer, Heeger (SSH) model. It is applied throughout this Thesis to the zero-energy states emerging in the borylated 7aGNRs.
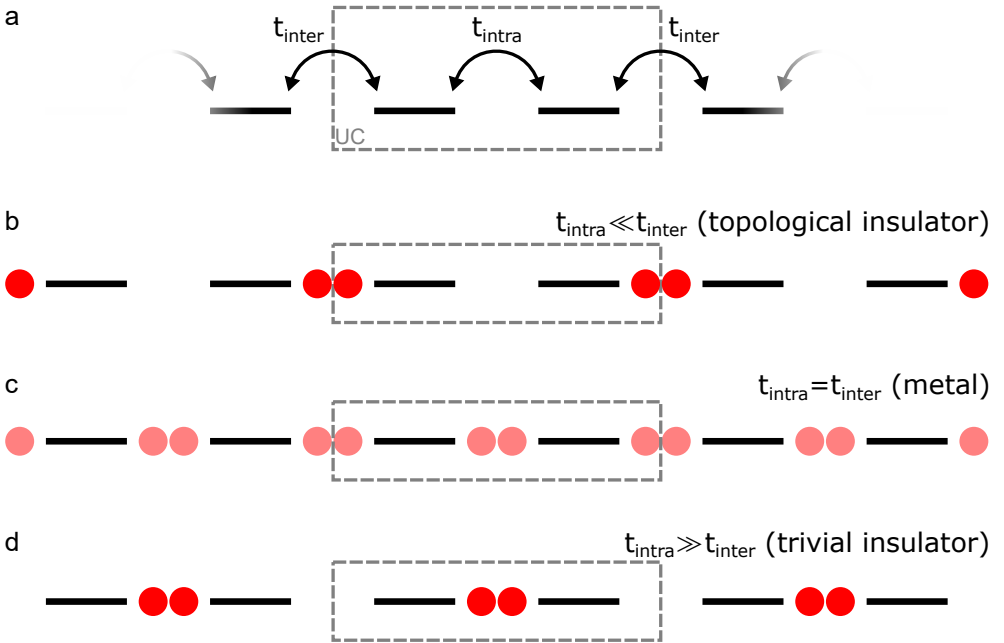
The SSH Model

Figure 1.6: A topological transition in the SSH model: a Unit cell of the SSH chain. Electron sites are connected by the staggered hopping amplitudes t_{intra} within the unit cell and t_{inter} with the site in the adjacent unit cell. **b** For $t_{intra} \ll t_{inter}$, the chain dissociates into dimers that mainly localize at the boundary between unit cells. At the termination of the SSH chain forms a topologically protected edge state. This situation describes a topological insulator. **c** For $t_{intra} = t_{inter}$, the electrons have no preferential position with respect to the bonds. The chain is metallic. **d** For $t_{intra} \gg t_{inter}$, the chain dissociates into dimers, too. Now, they are localized within the unit cell and the chain forms a trivial insulator.

The SSH model[105] describes the electron dispersion in polyacetylene due to the alternation of single and double bonds by the hopping of spinless fermions along a one dimensional chain with staggered hopping amplitudes (t_{intra} and t_{inter}) (see Figure 1.6). If one of the hopping parameters is zero, the system is insulating and all fermions are fully localized between each two sites. Interestingly, two single fermions remain isolated and unpaired at the two edges of a finite SSH chain for $t_{\text{intra}} = 0$, $t_{\text{inter}} > 0$. This corresponds to the spin-polarized edge state observed in topological insulators. For $t_{\text{inter}} = 0$, $t_{\text{intra}} > 0$, all fermions are paired. The chain is topologically trivial. It is possible to pass from one state to the other by continuously increasing one parameter and decreasing the other. Again, we will necessarily pass a metallic configuration, where the fermions are fully delocalized at $t_{\text{inter}} = t_{\text{intra}}$. I will use the SSH-model in Chapter 4 to study the topological character of spin-polarized states in the boron-doped GNRs.

Topological edge states cannot break symmetries present in the bulk system. Importantly, the sublattice symmetry of the pristine and boron-doped 7aGNR implies chiral, *i.e.* spin-polarized edge states. The interaction of the spin-polarized edge state with the substrate's electrons leads to the Kondo effect.

1.2.4 The Kondo Effect

The Kondo model describes the interaction of a single spin with a bath of non-interacting electrons. It was first developed to explain an increase in the low-temperature resistance of metals containing magnetic impurities[106]. Today, it is a very important STS feature to identify atomic scale magnetism.

In the 1930s, de Haas *et al.*[107] measured an increased resistivity of metallic wires at low temperatures, which could not be explained by the conventional theory for resistance caused by electron-phonon scattering. It took 30 years until Jun Kondo[108] came up with an adequate theoretical description of the phenomenon. He investigated the interaction of a single magnetic impurity with the conduction band electrons of the metal using perturbation theory and found that the 2nd order term of the

perturbation leads to a logarithmic correction of the resistivity of the wire

$$\rho = \rho_0 + aT^5 + cJ \log T, \tag{1.14}$$

with the material constants ρ_0, a and c, the temperature T and the antiferromagnetic coupling constant $J < 0$. The terms of Equation 1.14 describe the zero-temperature resistance, the resistance due to electron-phonon scattering and to electron-spin scattering, respectively.

The Kondo model in this form has the shortcoming that ρ diverges for $T \to 0\,\mathrm{K}$ and only describes the physics accurately above the so-called Kondo-Temperature[109]

$$T_\mathrm{K} \sim \exp\left[-\frac{1}{\rho|J|}\right]. \tag{1.15}$$

The problem was solved by Wilson[110] using a numerical renormalization approach by showing that the conduction band electrons and the electron in the impurity form a singlet many-body ground state for low temperatures. The spin of the magnetic impurity is effectively screened by the surrounding electron bath.

The physical mechanism behind the screening can be understood in the single impurity Anderson model (SIAM)[111]. Schrieffer and Wolff showed that the SIAM Hamiltonian and the Kondo Hamiltonian are equivalent to each other[112]. Insights about the physics in one model are therefore valid to understand the other. The SIAM describes a two level quantum system (QS) with single-electron states available at ε and $\varepsilon + U$ that is coupled to an electron bath ($E_\mathrm{Fermi} \equiv 0$) (see Figure 1.7a). I will restrict the discussion to the case of $\varepsilon < 0$ and $U > |\varepsilon|$, *i.e.* a singly occupied QS, as this is the relevant range for Kondo physics.

The classically forbidden excitations shown in Figure 1.7b are quantum mechanically allowed by the Heisenberg uncertainty principle as part of a virtual excitation that decays sufficiently fast. The decay does not favor one spin over the other and the QS is equally likely to end up in the initial state $|\downarrow\rangle$ (Figure 1.7a) or in the spin-flipped state $|\uparrow\rangle$ (Figure 1.7c). As a consequence, the ground state of the system is an $S = 0$ spin-singlet resonance state formed by the linear combination of $|\downarrow\rangle$ and $|\uparrow\rangle$. It is important to note, that this is a many-body ground state caused by the coupling to the electron bath. The many-body character of the state
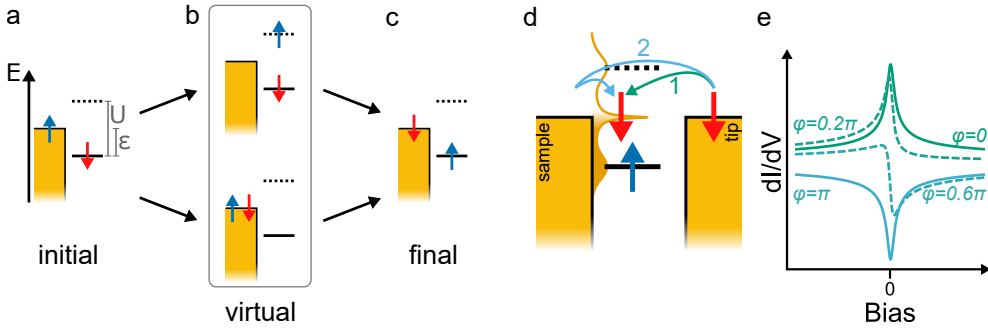
27

Figure 1.7: The Kondo effect: **a** Sketch of a single impurity spin that is weakly interacting with an electron bath. **b** Hopping processes can lead to virtual spin excitations. **c** The virtual excitations can decay to a different ground state that results in a spin flip with respect to the initial configuration. **d** The resonant superposition of initial and final state, connected *via* the virtual excitation forms a narrow resonance that is pinned to the Fermi level. In STS experiments, electrons tunneling from tip to substrate can either tunnel directly through the resonance (1) or tunnel indirectly *via* a different channel into the substrate and from there into the resonance (2). **e** The Kondo resonance manifests itself in $\mathrm{d}I/\mathrm{d}V$ spectroscopy as a Frota lineshape. The complex phase factor is determined by the tunneling channels (1) and (2). A peak ($\varphi = 0$) corresponds to tunneling directly through the resonance. A dip ($\varphi = \pi$) corresponds to only indirect tunneling. Interference between the direct and indirect channel leads to intermediate values of φ.

pins it to the Fermi level, as electrons close to E_{Fermi} are exponentially more likely involved in the resonant scattering process.

The Kondo resonance is characterized by a logarithmic line shape. Historically, the Fano line shape[113] was used to phenomenologically describe the Kondo resonance. But recent work[114] showed that the Frota function[115] describes the Kondo resonance better in case of small lock-in modulations like the ones used in this Thesis

$$Frota(V) \propto \mathrm{Im}\left[ie^{i\varphi}\sqrt{\frac{i\Gamma_{\mathrm{Frota}}}{eV - E_{\mathrm{K}} + i\Gamma_{\mathrm{Frota}}}}\right], \qquad (1.16)$$

where Im is the imaginary part of the argument, φ is a phase factor, E_{K} is the center of the resonance and Γ_{Frota} is the width of the resonance. The phase factor φ accounts for interference due to different tunneling channels connecting tip and sample. In most STS experiments, tunneling is restricted to the direct Kondo channel, 1 in Figure 1.7d, where all electrons tunnel through the spin-polarized orbital of the magnetic impurity,

corresponding to $\varphi = 0$[116] (Figure 1.7e). On the other hand, electrons can also tunnel directly or *via* a non-spin-polarized orbital into the sample, from where they can interact with the Kondo impurity (channel 2 in Figure 1.7d). This interaction causes a dip in the $\mathrm{d}I/\mathrm{d}V$ spectrum, corresponding to $\varphi = \pi$. Intermediate values of φ describe the degree of mixing between the two channels.

The half width at half maximum (HWHM) $\Delta/2 = 2.542\Gamma_{\mathrm{Frota}}$ of the Kondo resonance at $T = 0$ is proportional to the Kondo temperature. Increasing temperature weakens the Kondo scattering, resulting in a broadening of the resonance following the expression[117]

$$\Delta = 2\sqrt{(\alpha k_{\mathrm{B}}T)^2 + (2k_{\mathrm{B}}T_{\mathrm{K}})^2},\tag{1.17}$$

where k_{B} is the Boltzmann constant. The constant $\alpha = 2\pi$ is obtained from a Fermi-liquid model for $S = 1/2$[117]. In experiments, values of $\alpha = 5.4$[118] and $\alpha = 9.5$[89] for $S = 1/2$, and $\alpha = 8.5$ for $S = 1$[119] were found. The combination of these unique properties — zero-bias pinning, a well-defined line shape and characteristic broadening with increasing temperature — makes the Kondo resonance an ideal fingerprint for experimental detection of atomic scale magnetism.

1.2.5   The Mean-Field Hubbard Model

The experimental synthesis and characterization of graphene nanostructures is challenging and time consuming. Furthermore, it is difficult to disentangle the physics of the unperturbed system from effects emerging due to hybridization with the substrate. The mean-field Hubbard model provides a relatively simple Hamiltonian that captures the essential physics of graphene nanostructures precisely allowing to predict their properties from inexpensive calculations.

The carbon atoms in a graphene nanostructure form an sp^2 lattice where three of the four valence electrons form σ bonds, while the fourth forms a π bond. The π-electron movement in this system can be described in a simple tight binding picture[120]

$$H_{\mathrm{TB}} = \sum_{i,j,\sigma} t_{ij} c_{i\sigma}^{\dagger} c_{j\sigma},\tag{1.18}$$

where t_{ij} is the hopping amplitude between site i and site j, and $c_{i\sigma}^\dagger$ $(c_{i\sigma})$ creates (annihilates) one electron with spin σ in the p_z orbital at site i. The hopping amplitudes t_{ij} can be calculated from the overlap between atomic orbital wavefunctions at the sites i and j. The coefficients t_{ij} vanish for atoms that are separated sufficiently far from each other. In fact, it was shown that considering up to third-nearest neighbour hopping reproduces accurately *ab initio* calculations[89,121]. The term collapses to

$$H_{\text{TB}} = -t_1 \sum_{\langle i,j \rangle,\sigma} (c_{i\sigma}^\dagger c_{j\sigma}) - t_2 \sum_{\langle\langle i,j \rangle\rangle,\sigma} (c_{i\sigma}^\dagger c_{j\sigma}) - t_3 \sum_{\langle\langle\langle i,j \rangle\rangle\rangle,\sigma} (c_{i\sigma}^\dagger c_{j\sigma}) + h.c., \quad (1.19)$$

The first (second, third) term sums over the first (second, third) nearest neighbors in the carbon lattice as defined by geometrical distance. The two subsystems of $\sigma =\uparrow$ and $\sigma =\downarrow$ are completely decoupled and their eigenenergies are degenerate.

To study spin polarization related phenomena in the system, electron-electron interaction needs to be considered by introducing the Hubbard term[120]

$$H_{\text{H}} = U \sum_i n_{i\uparrow} n_{i\downarrow}, \quad (1.20)$$

with the Coulomb repulsion U and the number operator $n_{i\sigma} = c_{i\sigma}^\dagger c_{i\sigma}$. To solve this Hamiltonian efficiently, a mean-field description is employed. This approximation reduces the dimension of the Hilbert space by removing fast growing terms of $\mathcal{O}(4^N)$, with the number of p_z electrons N and, such, allows the simulation of experimentally relevant graphene nanoribbons containing hundreds of atoms. The number operator can be rewritten using the mean occupation $\langle n_{i\sigma} \rangle$

$$n_{i\sigma} = \langle n_{i\sigma} \rangle + \delta n_{i\sigma}, \quad (1.21)$$

where $\delta n_{i\sigma}$ is a small correction. Omitting terms that are quadratic in δn, we get

$$H_{\text{MFH}} = U \sum_i (n_{i\uparrow}\langle n_{i\downarrow}\rangle + \langle n_{i\uparrow}\rangle n_{i\downarrow} - \langle n_{i\uparrow}\rangle\langle n_{i\downarrow}\rangle) \approx H_{\text{H}}. \quad (1.22)$$

This term describes the interaction of spin up (down) electrons with a stationary mean field of spin down (up) electrons. By definition, the

stationary mean field replaces the sum of all electron-electron interactions by the interaction with an effective potential. The eigenenergies and eigenvectors of the non-interacting single particle Hamiltonian

$$H = H_{\mathrm{TB}} + H_{\mathrm{MFH}} \tag{1.23}$$

can be obtained by solving its eigenequation self-consistently.

In this Thesis, I use the MFH model to study the spin-polarization of a 7aGNR with dense 2 B-doping (Chapter 4) and simulate a partial substrate hybridization of the ribbon. For this, I relied on the hubbard Python package developed by Sofia Sanz and Thomas Frederiksen[122]. The hopping amplitudes $t_1 = 2.7\,\mathrm{eV}$, $t_2 = 0.2\,\mathrm{eV}$, $t_3 = 0.18\,\mathrm{eV}$ and $U = 3.5\,\mathrm{eV}$[89,121] were used, unless otherwise stated. Boron atoms were modelled by an additional on-site potential ($\varepsilon_{\mathrm{B}} = 3\,\mathrm{eV}$) added to the corresponding diagonal elements of the Hamiltonian and, at the same time, removing one electron from the total number of available electrons.

2 Bipolar Transport Through a Graphene Nanoribbon with Localized Boron States

Coherent electron transport through single molecules allows to probe directly molecular properties like energy level alignment, vibrational modes or spin states. In most STM experiments molecules are absorbed on a metallic substrate, resulting in an electronic hybridization that perturbs the molecular properties. Ultra-thin insulating layers electronically decouple the molecule from the substrate, creating a double barrier configuration. However, electron transport through such decoupled molecules occurs in an incoherent two-step process. Here, we present coherent electron transport through a double barrier configuration realized by suspending a boron doped seven armchair graphene nanoribbon between tip and substrate of a scanning tunneling microscope. The substitutional boron moiety in the suspended part of the ribbon acts as a quantum dot, with a localized in-gap state. Varying the tip-substrate separation, we are able to continuously change the vertical position of the quantum dot in the junction and study resonant transport with varying barrier width. Our results suggest that electronic transport is bipolar, namely, that the same occupied resonances are involved at each bias polarity. We identify bipolar transport also through vibronic satellite peaks, with eigenmode energy of $20\,\text{meV}$ and through the valence band of the ribbon. In fact, in this last case, we find fingerprints of a band quantization in form of Fabry-Perot quantum well modes.

2.1 Introduction

The coherent electronic conductance through molecular wires is determined by the relative alignment of the molecular states with respect to the Fermi levels of the source and drain electrodes[76,123]. The different transport regimes through a molecular wire are discussed in more detail in Section 1.2.1. Frequently, the Fermi level of the unbiased electrodes falls into the gap between the highest occupied and lowest unoccupied molecular orbital (HOMO and LUMO). Applying a small bias results in off-resonant coherent electron tunneling. This regime is characterized by an exponential decrease of the conductance G through the molecular wire $G \propto e^{-\beta z}$ with the decay constant β and wire length z[68].

Resonant electron tunneling is reached when a molecular orbital aligns with the Fermi level of one of the electrodes[74]. A coherent state connecting the molecule and the electrodes forms and the electronic transport becomes ballistic, *i.e.* independent of the length of the molecular wire ($\beta = 0$). The experimental access to the resonant tunneling regime is challenging. In ungated experiments, high voltages resulting in high currents are needed, resulting in fast degradation of the junction by rupture of the electrode-molecule bond[81,124] or even the chemical dissociation of the molecular wire itself[125].

Here, we study the electronic transport through the dilute 2B-doped 7aGNR (Figure 2.1a) suspended in the junction of a low-temperature scanning tunneling microscope. The ribbons were fabricated following the two-step on-surface synthesis *via* successive Ullmann-coupling and cyclodehydrogenation that is discussed in Section 1.1.4. Differential conductance ($\mathrm{d}I/\mathrm{d}V$) spectra sampled at transport lengths from $2\,\mathrm{nm}$ to $8\,\mathrm{nm}$ exhibit a complex spectrum composed of multiple resonances and satellite peaks, both at negative and positive bias.

The strongest resonances are assigned to the valence band (VB) of the ribbon and states localized around the dopant position (2B-states). Surprisingly, we find a closing of the gap between resonances at positive and negative bias with increasing tip retraction z. The conventional description of unipolar transport, where the whole voltage drops at the tip-ribbon contact, fails to describe this situation. Instead, a simple model assuming bipolar transport through the VB and the occupied 2B-state yields consistent results without the need for further assumptions.

Bipolar transport implies transport through a double tunneling barrier, which is expected for molecular wires in contact with both electrodes[18]. We find that approximately $60 - 70\%$ of the applied bias drops at the tip-ribbon bond.

Satellite peaks are identified as vibronic excitations. Their different energy spacing at positive and negative voltage is consistent with the different potential drops in the bipolar transport model. Quantum well modes of the confined valence band are, also identified in the dI/dV spectra. The resonant electronic conductance through the confined VB's zero mode remains constant, $i.e.$ $\beta = 0$, while increasing the tip retraction more than $3\,nm$, in agreement with expectations for a perfect electron transmission in a Fabry-Perot resonator[96].

2.2 Bipolar Transport Through a Localized Boron State

We start by probing the transport through a pristine 7aGNR without boron for reference. The two-terminal transport configuration is reached by mechanical manipulation of the ribbon using the tip of the STM[17,27,126–128] following the procedure described in Section 1.1.3. The conductance through the ribbon drops exponentially with increasing tip-sample-distance z and we obtain a co-tunneling decay constant of $\beta = 4\,nm^{-1}$ at $-20\,mV$, in good agreement with Koch et $al.$[17]. Retracting the ribbon to $z > 3\,nm$ enables us to reach the onset of resonant transport at higher bias without breaking the tip-ribbon bond. A dI/dV spectrum recorded at $z = 6.0\,nm$ reveals two resonances at $V^- = -0.7\,V$ and $V^+ = 1.4\,V$ (blue graph in Figure 2.1b) corresponding to resonant band transport. Repeating the experiment at identical z with a ribbon with a single diboron dopant (3.8-2B-GNR, Figure 2.1a), we find two resonances at identical V^+ and V^- (red curve in Figure 2.1b). On the borylated GNR, the differential conductance is two orders of magnitude higher and appears with an in-gap structure, that we focus on in the following.

Inside the gap between the band-transport peaks, two resonances appear at $V_{2B}^- = -0.5\,V$ and $V_{2B}^+ = 1.07\,V$ for transport through the 3.8-2B-GNR. We attribute these two peaks to resonant transport through a lo-
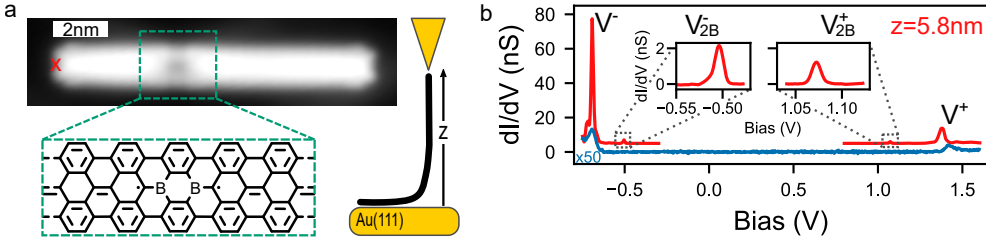
Figure 2.1: Differential conductance spectroscopy of a free-standing 2B-GNR: a STM topography image of the 3.8-2B-GNR ($V = -300\,\mathrm{mV}$, $I = 30\,\mathrm{pA}$) and Lewis structure of borylated segment. The red cross indicates the position from where the ribbon was lifted. The 2B-site is $3.8\,\mathrm{nm}$ away from the termination used for lifting. Right: Sketch of the ribbon suspended between tip and substrate with the tip retraction z indicated. **b** $\mathrm{d}I/\mathrm{d}V$ spectra for a 7aGNR with a single 2B-dopant (3.8-2B-GNR, red, $z = 5.8\,\mathrm{nm}$) and a pristine ribbon without doping (blue, $z = 6\,\mathrm{nm}$). The peaks V^- and V^+ are associated with resonant band transport through carbon bands. Two states V_{2B}^- and V_{2B}^+ appear in the gap between V^- and V^+ in the doped system, as shown enlarged in the inset.

calized state induced by the boron moiety[96,97]. Since the band-transport resonances of the borylated and pristine ribbon appear at identical bias, the presence of the boron state does not perturb the band structure of the ribbon, as predicted theoretically[96]. Importantly, the boron induced state is strongly localized around the 2B moiety. The 2B moiety is separated by $3.8\,\mathrm{nm}$ from the tip-ribbon bond, and, therefore, it is well separated from tip and substrate at a tip-retraction of $z = 6.0\,\mathrm{nm}$. In this configuration, the boron state provides a single molecular orbital inside the junction, creating a double barrier configuration as discussed in Section 1.2.1.

The positions V_{2B}^- and V_{2B}^+ of resonant transport through the 2B-state moves towards more negative values upon increasing z, as can be seen in the colorplot of $\mathrm{d}I/\mathrm{d}V$ spectra in Figure 2.2a, recorded in the range of $2.1\,\mathrm{nm} < z < 8.3\,\mathrm{nm}$. Both V_{2B}^- and V_{2B}^+ stay consistently between the peaks of resonant band transport (labelled V^- and V^+). The relative movement of V_{2B}^- and V_{2B}^+ with respect to their position at $z = 4\,\mathrm{nm}$ reveals that V_{2B}^+ moves faster to negative bias than V_{2B}^- (Figure 2.2b), *i.e.* their separation decreases. This effect is especially pronounced at lower z.

To model this behaviour, we approximate the tip-substrate junction by a plate capacitor and the 2B-state as a quantum dot (QD) separated
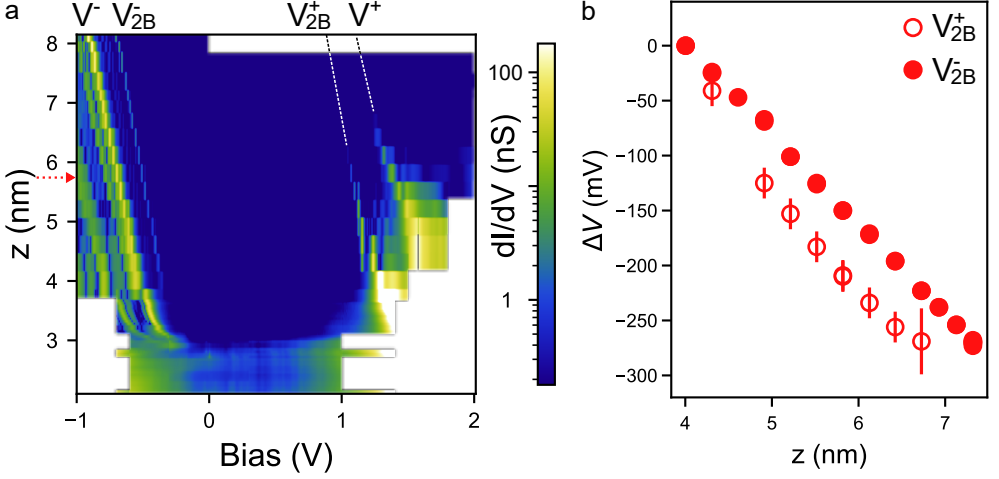
Figure 2.2: Resonant transport through 2B-state: a Colorplot of $\mathrm{d}I/\mathrm{d}V$ spectra at different tip sample separation z in logarithmic scale. The band-resonant transport and the 2B-states are clearly identified in the spectra for $z > 3\,\mathrm{nm}$. The red arrow indicates the position of the spectra in Figure 2.1. **b** Relative movement of $V_{2\mathrm{B}}^-$ and $V_{2\mathrm{B}}^+$ with respect to their reference value at $z = 4\,\mathrm{nm}$. $V_{2\mathrm{B}}^+$ shifts faster to negative values than $V_{2\mathrm{B}}^-$, which is the fingerprint of bipolar transport.

by tunneling barriers from both tip and substrate (Figure 2.3a). The tip-2B-state separation $d \sim 3.8\,\mathrm{nm}$ is constant and does not depend on z, meaning that any change in z is directly reflected in a change of the 2B-state-substrate separation. This configuration resembles the one of a molecule used for scanning quantum dot microscopy[53]. Here, resonant transport through the 2B-state is enabled when the energy level of the quantum dot aligns with the Fermi level of tip or substrate, instead of the change of the molecular charge state. If $V_{2\mathrm{B}}^-$ and $V_{2\mathrm{B}}^+$ correspond to unipolar transport through one occupied and one unoccupied state, we can use directly the equations provided by Wagner *et al.*[53]

$$V_{2\mathrm{B}}^- = \frac{\varepsilon_-}{e\alpha} = \frac{z\varepsilon_-}{ed} \text{ and} \tag{2.1}$$

$$V_{2\mathrm{B}}^+ = \frac{\varepsilon_+}{e\alpha} = \frac{z\varepsilon_+}{ed}, \tag{2.2}$$

with the elementary charge e and the two energies ε_- and ε_+ of the occupied and unoccupied state, respectively. And α is the fraction of voltage dropping between tip and QD. From geometrical considerations on the linear voltage drop in the plate capacitor follows $\alpha = d/z$. The
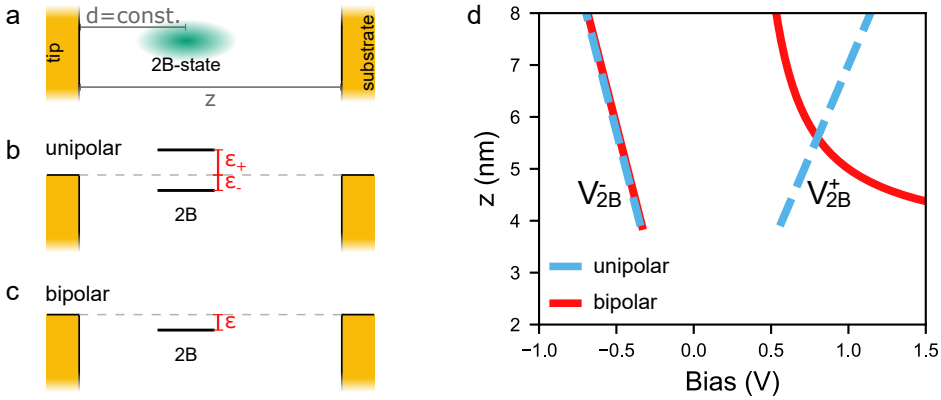
Figure 2.3: Comparison of uni- and bipolar transport models: a Sketch of the assumed plate capacitor geometry of the tunneling junction. The 2B-state is separated by the constant distance d from the tip. The tip-substrate separation z is sufficiently large that the 2B-state is isolated from both electrodes. **b** Sketch of the equilibrium position for unipolar transport through two energy levels ε_- and ε_+, resembling the configuration observed by Wagner *et al.*[53]. **c** Sketch of the equilibrium position for bipolar transport through the single level ε. The conditions for resonant transport are given in Figure 2.4a, b. **d** Simulated V_{2B}^- and V_{2B}^+ as functions of z for the unipolar model (blue, dashed line) and the bipolar model (red, solid line). Here we assumed $\alpha = d/z$ following from the plate capacitor model. The curves were modelled with $d = 3.5\,\mathrm{nm}$, $\varepsilon_- = -0.31\,\mathrm{eV}$, $\varepsilon_+ = 0.5\,\mathrm{eV}$, $\varepsilon = -0.3\,\mathrm{eV}$.

position of V_{2B}^- and V_{2B}^+ in this scenario is plotted as a function of z as a blue, dotted line in Figure 2.3d. For increasing z, both peaks shift to larger absolute values, increasing the separation between the two states. Our observations are clearly in contradiction of this scenario.

Instead, we propose a one-level bipolar transport model to explain the appearance and relative shift of V_{2B}^- and V_{2B}^+, where only the occupied boron state governs the resonant transport for both voltage polarities (Figure 2.3c).The onset of resonant transport in this scenario occurs at

$$\varepsilon = \alpha e V_{2B}^-, \tag{2.3}$$

$$-\varepsilon = (1 - \alpha)e V_{2B}^+ \text{ and} \tag{2.4}$$

with the energy $\varepsilon < 0$ of the unoccupied state. Figure 2.4a depicts onset of bipolar conduction at positive bias (Equation 2.4) and Figure 2.4b at

negative bias (Equation 2.3). Solving this set of equations for V_{2B}^- and V_{2B}^+ yields

$$V_{2B}^- = \frac{z\varepsilon}{ed} \text{ and} \tag{2.5}$$

$$V_{2B}^+ = \frac{-\varepsilon z}{e(z-d)}. \tag{2.6}$$

Interestingly, the term $(1-\alpha)$ induces a non-linear behaviour in V^+. This bipolar transport scenario is plotted as the red solid line in Figure 2.3d. Both V_{2B}^- and V_{2B}^+ shift towards more negative values. While V_{2B}^- shifts linearly, the $\sim 1/z$ trend of V_{2B}^+ moves it faster towards negative values at small z with this trend levelling off at larger z. This model reproduces qualitatively the experimentally observed peak movement.

Bipolar transport through an unoccupied level corresponds to an electron-hole inversion in the model resulting in an exchange of V_{2B}^- and V_{2B}^+, *i.e.* mirroring their positions at $V = 0$. From this consideration, we can exclude bipolar transport through an unoccupied state.

Equation 2.3 and 2.4 allow us to extract values for α and ε from the experimental V_{2B}^- and V_{2B}^+. The analytical solutions of this set of equations are

$$\alpha = \frac{V^+}{V^+ - V^-} \text{ and} \tag{2.7}$$

$$\varepsilon = \frac{eV^-V^+}{V^+ - V^-}, \tag{2.8}$$

where the index 2B was omitted for clarity.

We find that α obtained from the experimental V_{2B}^- and V_{2B}^+ decreases monotonously with increasing z (Figure 2.4d) as is expected for a quantum dot in constant separation of the tip[53]. The finding is also observed for a GNR with the 2B-dopant site ~ 0.9 nm closer to the tip (orange symbols). This ribbon is referred to as 2.9-2B-GNR. Remarkably, the two curves of α are laterally offseted by ~ 0.9 nm with respect to each other. This offset is in agreement with the different separation of 2B-state and substrate at identical tip-sample distances caused by the different position of the 2B-state in the ribbon. The energy ε of the state is ~ -300 to -400 meV, slowly moving away from the Fermi level with increasing z. We attribute this to a reduced p-doping of the GNR upon
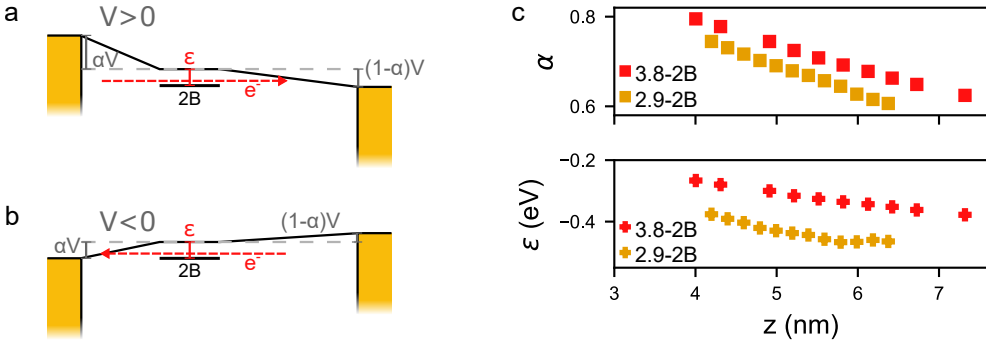
Figure 2.4: Resonant transport in the bipolar transport model: a, b Sketch of the tunneling at V_{2B}^- and at V_{2B}^+. The 2B-state is separated spatially from both electrodes, but maintains a fixed distance to the tip. **c** Gating efficiency α and 2B-state energy ε for the 3.8-2B-GNR (red) and 2.9-2B-GNR (orange). Note the lateral offset of α of $\Delta z \approx 0.9\,\mathrm{nm}$ corresponding precisely to the different tip 2B-site separation for the two ribbons.

reducing the hybridization with the electron-accepting Au(111) while lifting the ribbon from the surface[126].

Vibronic Excitations

The resonances V_{2B}^- and V_{2B}^+ are accompanied by several satellite peaks (Figure 2.5a). The equidistant energy spacing of the satellite peaks is a typical fingerprint of vibronic excited states[129]. For both polarities, the second and third resonance are the most intense, whereas the first is very weak and the fourth disappears in the onset of the band-transport resonance. The peak intensities are governed by the Franck-Condon coefficients. Their apparently identical values are another indicator that the resonance belongs to the same state accessed *via* bipolar transport.

We extract the corresponding gated vibrational energies E_ν by a linear regression fitted to the energy of the vibrations (Figure 2.5b) and obtain $E_\nu^- = 31 \pm 1\,\mathrm{meV}$ for the negative and $E_\nu^+ = 57 \pm 1\,\mathrm{meV}$ for the positive vibration. Since the resonance conditions for the vibronic excitations are equivalent to the ones for the band transport, we obtain $\alpha = 0.65 \pm 0.01$ from the two values of E_ν measured for the same vibronic mode at $z = 5.82\,\mathrm{nm}$ assuming bipolar transport. This value is in close quantitative agreement with values obtained from resonant transport through the 2B-state.
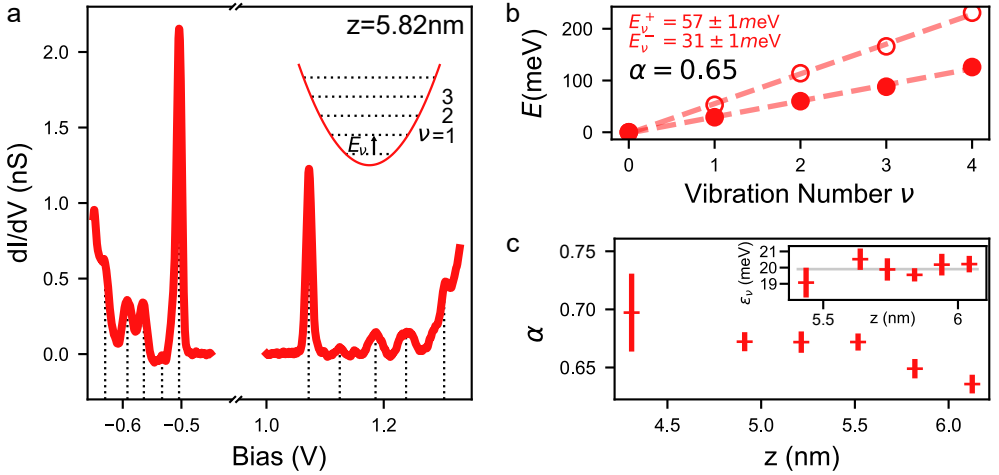
Figure 2.5: Vibrational Modes of the 3.8-**2B-GNR: a** V_{2B}^- and V_{2B}^+ with their satellite structure for the same ribbon as in Figure 2.1. The equidistant spacing is the fingerprint of vibrational modes. The inset depicts the parabolic potential resulting in equidistant energy level spacing. Note, that the relative peak intensities for both bias polarities are almost identical in agreement with bipolar transport. **b** Linear regression fitted to the relative peak energies for negative (filled circles) and positive (open circles) bias. The ratio between the gated vibrational energies yields $\alpha = 0.65 \pm 0.01$ in good quantitative agreement with the value obtained from the peak position of $\nu = 0$. **c** α as obtained in **b** for different z. The overall trend of decreasing α with increasing z is reproduced. The inset shows a constant fundamental vibrational energy of $\varepsilon_\nu = 19.9 \pm 0.5\,\mathrm{meV}$.

Extending the analysis to spectra recorded at different z reproduces that α decreases for increasing z (Figure 2.5c) similar to the values shown in Figure 2.3d. The fundamental vibrational energy $\varepsilon_\nu = 19.9 \pm 0.5\,\mathrm{meV}$ does not vary significantly over the observed range (inset Figure 2.5c). This energy does not match with internal vibronic modes of the 7aGNR[130] or the 2B-7aGNR[98]. Its constant nature excludes an external vibration of the complete free standing segment. The absence of the vibrational satellite peaks in the pristine ribbon indicates a connection of the vibration to the boron atoms.

41

2.3 Bipolar Transport Through the Valence Band

Interestingly, we observe in Figure 2.2a that both V^- and V^+ shift towards more negative values with increasing z. In the 2.9-2B-GNR (Figure 2.6a, b), V^- and V^+ move parallel to V_{2B}^- and V_{2B}^+ towards more negative values with increasing z. We find that even for the pristine GNR (Figure 2.6c, d, also see Figure 2.10 in the Appendix to this Chapter) the positive resonant transport peak V^+ moves towards negative values with increasing z. V^- remains approximately at the same bias voltage.

The relative shift of V^- and V^+ with respect to their initial position is presented in Figure 2.6e. Strikingly, we observe the same behaviour as before for V_{2B}^- and V_{2B}^+. In all three investigated ribbons, V^+ shifts faster to negative values than V^-. We consider this as indicative that bipolar transport also occurs through the ribbon's VB. This is further supported by the gaps between V^- and V^+ of lifted pristine and 3.8-2B-GNR (Figure 2.2), which are significantly smaller than reported band gaps for ribbons on Au(111)[48,97]. The hybridization with the metal substrate reduces electron correlations, which results in a reduction of the gap between valence and conduction band in the absorbed ribbon. If any change were to be expected, it would be a larger band gap.

We employ the same two-barrier model as before to analyze the bipolar transport through the VB. The results for α are presented in Figure 2.6f. For the pristine ribbon, we obtain $\alpha \approx 0.68$, independent of z. This value is in very good agreement with bipolar transport in other molecular wires suspended in an STM junction[18]. The constant value indicates that decreasing hybridization with the substrate does not affect the electronic gating of the ribbon.

The gating efficiency of the borylated nanoribbons (red and orange squares) reduces from ~ 0.7 to ~ 0.6 in the observed interval. We observe that the curves of α are offsetted by $0.8\,\mathrm{nm}$ with respect to each other, similar to the α of the 2B-states in Figure 2.4c.

Furthermore, we observe satellite peaks to V^+ in equidistant energy spacing (Figure 2.6g). Comparing their energy spacing to ε_ν^+ obtained from V_{2B}^+ we find an almost perfect match between their energies. Even their relative intensities are approximately reproduced.
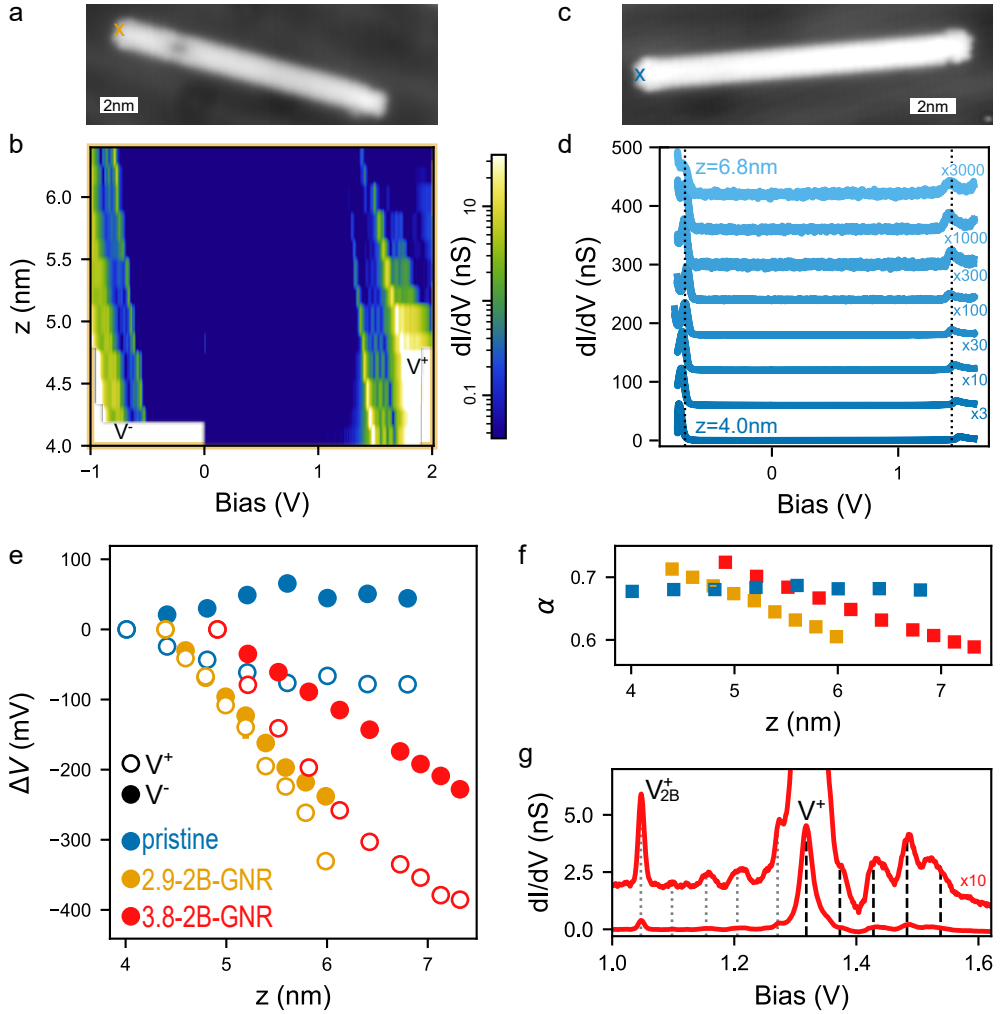
Figure 2.6: Bipolar transport through the valence band: a STM topography image of the 2.9-2B-GNR ($V = -300\,\mathrm{mV}$, $I = 30\,\mathrm{pA}$). The colored cross indicates the lifting position. **b** Colorplot of $\mathrm{d}I/\mathrm{d}V$ spectra at different tip sample separation z in logarithmic scale. The band resonant transport (V^- and V^+) and the 2B-states are clearly identified throughout the whole range. **c** Same as in **a**, but for a pristine GNR. **d** Waterfall of $\mathrm{d}I/\mathrm{d}V$ spectra in steps of $\Delta z = 0.4\,\mathrm{nm}$ with the pristine ribbon suspended in the junction. The spectra are scaled offset by $55\,\mathrm{nS}$ for clarity. The vertical lines are meant as a guide to the eye. **e** Relative movement of V^- and V^+ with respect to their reference values. In all cases V^+ shifts faster to negative values than V^-, indicating bipolar transport through the VB. **f** Gating efficiency α of for the pristine (blue), 2.8-2B-GNR (orange) and 3.9-2B-GNR (red) as a function of tip-sample separation z. The decrease of α with z for the boron doped systems is related to the interaction of VB and boron moiety. **g** $\mathrm{d}I/\mathrm{d}V$ spectrum of the 3.8-2B-GNR at $z = 6.1\,\mathrm{nm}$. The energy spacing between satellite peaks above $V_{2B}^+ = 1.047\,\mathrm{V}$ and above $V^+ = 1.318\,\mathrm{V}$ is identical, indicating that they correspond to the same vibronic states.
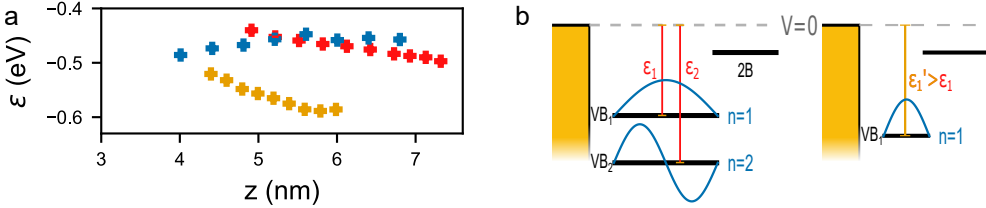
43

Valence Band Quantization

Figure 2.7: Valence band quantization by the diboron moiety: a VB energy ε of the pristine (blue), 2.9-2B-GNR (orange) and 3.8-2B-GNR (red). **b** Particle-in-a-box model for the band quantization of the VB, sketched for the 3.8-2B-GNR (left) and 2.9-2B-GNR (right). The boron moiety creates a high energy barrier for the VB resulting in a quantization of the band. The different confinement length for the VB results in the different ε of the boron doped ribbons in **a**.

In Figure 2.7a, we show the evolution of the VB energies ε_{VB} with z. For all three ribbons, we observe a weak shift of ε_{VB}. Strikingly, the VB of the 2.9-2B-GNR (orange symbols) lies significantly lower in energy, while the valence bands of the other two ribbons are in close quantitative agreement. This different VB energy is a consequence of valence band confinement in a shorter segment between tip and 2B-site. Figure 2.7b depicts a sketch of the situation. As will be shown later in Chapter 3, the diboron moiety is a high energy barrier for VB electrons[97] which are then confined in the space between tip and diboron, as in a particle-in-a-box potential. Reducing the length of the box increases the energy of the state, i.e. shifts it away from the Fermi level.

This finding has a significant implication for the observed bipolar transport related to the double barrier configuration. The observed peaks V^- and V^+ stem from resonant transport through the segment of the VB confined between tip and 2B-unit (confined VB). The diboron moiety "barrier" decouples the confined VB from the remaining VB, at the other part of the ribbon. In this way, we may treat the confined VB as an isolated quantum dot in constant separation to the tip (a similar case to the situation of the 2B-state in Figure 2.3a). From that consideration, we can understand the origin of the decrease of α with increasing z. The tip retraction process does not modify the VB quantum well at the tip side, but instead increases its separation with the substrate. Therefore,

the potential drop $(1 - \alpha)$ between 2B-unit and substrate increases with z, and consequently, α decreases, as we see in the experiment

Owing to the quantum well character of the confined valence band, higher order resonant states of the valence band might be accessible for transport. We did particle-in-a-box calculations of the energy difference between the first and second quantum well states (VB_1 and VB_2) and their expected spectral resonant energy for the 3.8-2B-GNR, considering $\alpha(z)$, a confinement length of $L = 3.8 \, \text{nm}$ and the effective electron mass of $m_{\text{eff}} = 0.4 m_{\text{e}}$[131]. Figure 2.8 presents a series of $\text{d}I/\text{d}V$ spectra with the experimentally obtained resonances and the calculated VB_2 resonances indicated by arrows. The spectral resonances found above V^- and V^+ in the $\text{d}I/\text{d}V$ spectra reproduce perfectly the positions obtained in these simple particle-in-a-box calculations.
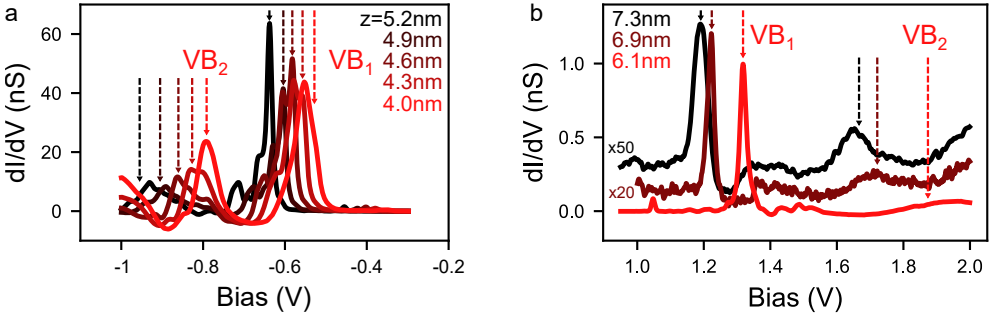

Figure 2.8: **Quantum well modes in resonant transport: a, b** $\text{d}I/\text{d}V$ spectra of the 3.8-2B-GNR at different z. The expected voltages for quantum well resonances of the confined VB are indicated by vertical lines. Transport through the excited state is suppressed quickly at negative bias while it persists up to large z for positive bias. Spectra at positive bias are offset for clarity. Note the strong coupling to vibronic states at negative bias for small z.

These resonant quantum well states of a dilute 2B-doped 7aGNR's VB are predicted to exhibit perfect transmission comparable to a Fabry-Perot resonator[97]. We find that the conductance is constant with z for the first quantum well resonance of the 3.8-2B-GNR at negative bias ($\beta^- = -0.02 \pm 0.02 \, \text{nm}^{-1}$, Figure 2.9a). At positive bias voltage, however, the bipolar resonance for the same quantum well state reduces with a decay constant of $\beta^+ = 3.5 \pm 0.1 \, \text{nm}^{-1}$. A similar behaviour is observed for the 2B-state (Figure 2.9b). This behaviour is typical of asymmetric two level systems[9,132,133]. The on-substrate-hybridized segment of the VB
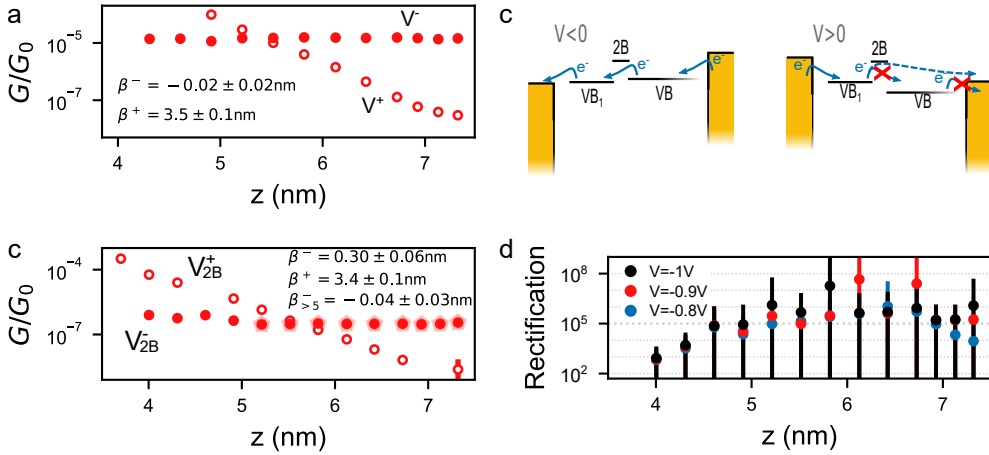
Figure 2.9: Diode-like transport: a, b Linear conductance G through the VB (**a**) and 2B-state (**b**) of the 3.8-2B-GNR at negative (filled circles) and positive bias (open circles). The decay constant β is indicated for both polarities. The decay constant $\beta_{>5}^-$ was calculated considering only the values for $z > 5\,\mathrm{nm}$. **c** Sketch of the two-level extension of the one-level bipolar transport model. At negative bias, electrons can tunnel from the non-quantized valence band through the quantum well resonance into the tip, resulting in a constant electron transmission. For positive bias, the non-quantized valence band is occupied and not available for electron transport. The electron transmission depends on the changing tip-sample separation. **d** The rectification ratio $|G(V)/G(-V)|$ for $V = -1\,\mathrm{V}$ (black circles), $V = -0.9\,\mathrm{V}$ (red circles) and $V = -0.8\,\mathrm{V}$ (blue circles). The large error bar stems from the error on the conductance at positive bias voltage. The corresponding values lie within the noise limit of the measurements, resulting in relative errors of $\sim 100\%$.

needs to be included in the model for a more complete understanding. A tentative sketch of the situation is given in Figure 2.9c. At negative voltage, transport through the (right) segment of the VB between substrate and 2B-state remains possible, resulting in the constant conductance with z, $i.e.$ ballistic resonant transport through suspended ribbon. However, this segment is not available for transport at positive voltage and electrons need to tunnel directly into metal substrate, resulting in the exponential suppression of conductance. We define the rectification ratio $|G(V)/G(-V)|$ to quantify the diode character of the borylated GNR. For $z > 5\,\mathrm{nm}$, a rectification ratio $> 10^5$ is reached consistently, on par with the highest values so far reported for molecular diodes[133,134].

2.4 Conclusion

In conclusion, we have shown bipolar resonant band transport in free-standing 7aGNRs suspended between two metallic electrodes. Inducing dilute substitutional 2B-doping in the ribbon creates an occupied in-gap state that also is available for bipolar transport. Due to its localization around the 2B-unit, the state behaves as a quantum dot. Furthermore, the presence of the boron moiety quantizes the valence band, creating a quantum well in the ribbon. Both ground and excited states of the quantized band are available for resonant electron transport. We find consistently throughout all experiments that around $60 - 70\%$ of the applied voltage drops over the tip-ribbon bond, quantifying a source of ambiguity in STM transport experiments. The diboron moiety separates the valence band into one segment that is hybridized with the substrate and one fully freestanding, quantized segment. Our experiments suggest a very high electron transmission through the freestanding segment determined mostly by the transparency of the tip-ribbon bond. This proves the concept of high-conductance graphene nanoribbons based on a Fabry-Perot resonator principle.

2.5 Appendix

Here, we present the complete conductance map for the transport experiments through the pristine GNR. The band resonant transport is almost hidden in the diffuse onset of co-tunneling conductance. The apparent gap-opening observed from the co-tunneling conductance was reported before[27].
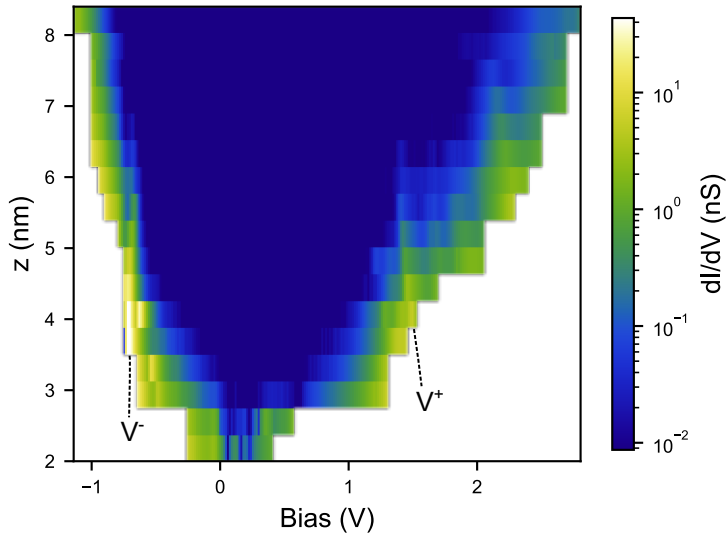

Figure 2.10: **Conductance map of the pristine 7aGNR** Colorplot of $\mathrm{d}I/\mathrm{d}V$ spectra at different tip sample separation z in logarithmic scale.

3 Magnetism of Topological Boundary States Induced by Boron Substitution in Graphene Nanoribbons

Graphene nanoribbons, low-dimensional platforms for carbon-based electronics, show the promising perspective to also incorporate spin polarization in their conjugated electron system. However, magnetism in GNRs is generally associated with localized states around zigzag edges, difficult to fabricate and with high reactivity. Here we demonstrate that magnetism can also be induced away from physical GNR zigzag edges through atomically precise engineering topological defects in its interior. A pair of substitutional boron atoms inserted in the carbon backbone breaks the conjugation of their topological bands and builds two spin-polarized boundary states around. The spin state was detected in electrical transport measurements through boron-substituted GNRs suspended between the tip and sample of a scanning tunneling microscope. First-principle simulations find that boron pairs induce a spin 1, which is modified by tuning the spacing between pairs. Our results demonstrate a route to embed spin chains in GNRs, turning them basic elements of spintronic devices.

- *Magnetism of Topological Boundary States Induced by Boron Substitution in Graphene Nanoribbons*

  Niklas Friedrich, Pedro Brandimarte, Jingcheng Li, Shohei Saito, Shigehiro Yamaguchi, Iago Pozo, Diego Peña, Thomas Frederiksen, Aran Garcia-Lekue, Daniel Sánchez-Portal, and José Ignacio Pascual

  Phys. Rev. Lett. **125**, 146801 – Published 28 September 2020

  https://journals.aps.org/prl/abstract/10.1103/PhysRevLett.125.146801

3.1 Introduction

In spite of being a diamagnetic material, graphene can develop a special class of magnetism via the polarization of its π-electron cloud. Such π paramagnetism is less localized than the more conventional d or f magnetism, and can interact over longer distances. Magnetic graphene nanostructures thus offer promising perspectives for *à la carte* engineering of interacting spin systems with applications in quantum spintronics devices[91,135–137].

Substituting one carbon atom of the graphene lattice by heteratoms is a potential route to induce magnetism[138,139]. A representative case is the doping of graphene with substitutional boron atoms (Figure 3.1), because it can be idealized as the removal of one electron from the conjugated bipartite lattice plus the energy upshift of a p_z state. However, boron atoms do not induce any spin imbalance around, but simply behave as a point potential[138]. A prerequisite for the emergence of π paramagnetism is that the point defect also causes a sufficiently large rupture of the conjugated electron system, for example by completely removing lattice sites or saturating p_z orbitals[140–142], resulting in the localization of radical states.
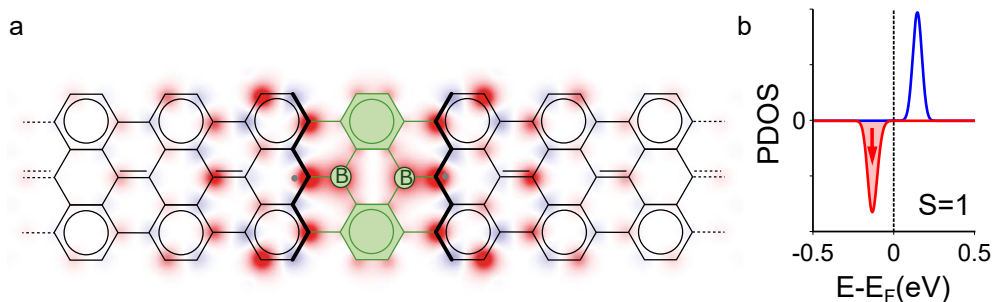

Figure 3.1: Spin polarization around a 2B-unit in a 7aGNR: a Lewis structure of the 2B-7aGNR shown over a color map representing the spin polarization density map, computed by density functional theory simulations (green represents the boron moiety). **b** Spin-resolved projected density of states (PDOS) over carbon atoms around the boron dimer. A net spin polarization of one kind confirms the ferromagnetic alignment of the two magnetic moments.

Here we show that inserting a pair of boron atoms in the carbon lattice of graphene nanoribbons enables a magnetic ground state. Density Functional Theory (DFT) simulations (3.1) show that, while magnetism is completely absent around a pair of such substitutional B atoms in different sublattices of extended graphene, in a 7-carbon-wide armchair GNR the boron pair builds up a net magnetic moment of $2\mu_B$ (two Bohr magnetons). The spin polarization, shown in Figure 3.1a, decays towards the pristine segments with the characteristic shape of the 7aGNR end states[143] (see Supplementary Information (SI) in[127] for a comparison). In fact, the spin cloud emerges from the rupture of the conjugated system imposed by the 2B-doped ring and the two neighbouring Clar sextets (green in Figure 3.1a). This moiety behaves as a highly reflective barrier for valence band electrons[96,97], thus inducing localized end states associated with the termination of the topological 7aGNR valence band[20]. This striking result offers the vision of combining band topology of nanoribbons[20,21,26] and heteroatoms for shaping spin textures in graphene ribbons.

3.2 The Kondo Resonance of a Topological Edge State

In our experiments, we substitutionally inserted boron pairs (2B) inside 7aGNRs (2B-7aGNRs) by adding a small fraction of 2B-doped trianthracene organic precursors (**1** in Figure 3.2a)[94–98,144] during the OSS of 7aGNRs using precursor **2**[23] (as schematically shown in Figure 3.2a, see Methods in SI in[127]). Scanning tunneling microscopy (STM) images of the fabricated ribbons (Figure 3.2b) resolved the 2B unit as a topography depression at varying positions inside the GNR[94,95,145]. Tunneling spectra showed no fingerprint of magnetism around the 2B moieties due to the strong interaction between boron and metal states[96,98], which quenches the eventual magnetic ground state. Therefore, to detect their intrinsic magnetic state the 2B moieties had to be removed from the metal substrate.

We used the STM tip to pick individual 2B-7aGNRs from one end (cross in Figure 3.2b) and lift them off to lie free-standing between tip and sample[17,146]. The (two-terminal) electrical transport through the
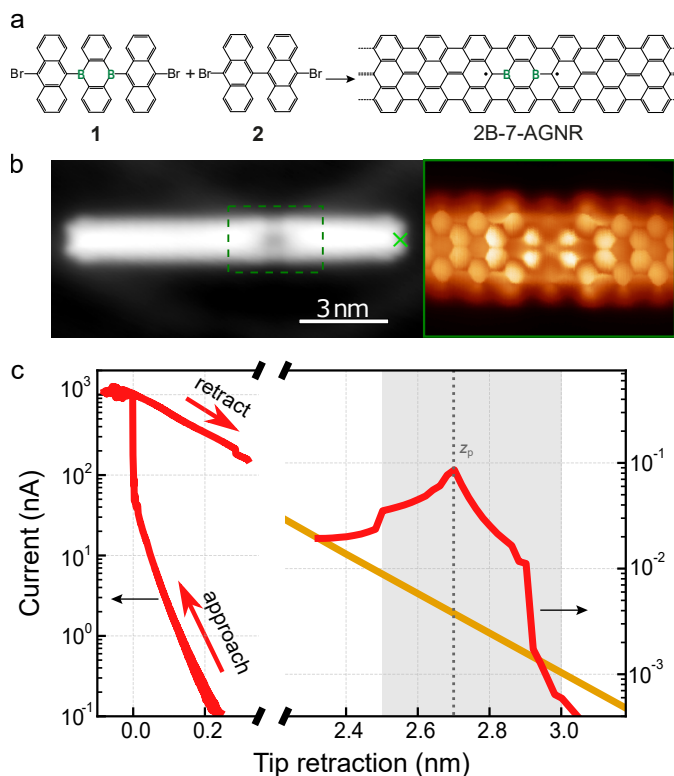
Figure 3.2: Conductance through a 2B-7aGNR: a Organic precursors mixed in the experiments. **b** STM constant current topography image of a 2B-7aGNR ($V_b = -300\,\mathrm{mV}$, $I = 30\,\mathrm{pA}$). The green cross indicates the position from where the GNR is lifted. (right) Constant height current scan ($V_b = 2\,\mathrm{mV}$) using a CO-functionalized tip[35] of the region indicated by the dashed rectangle. **c** Tunneling current I at $V_b = 25\,\mathrm{mV}$ as a function of z for a borylated (red) and a pristine (orange) GNR, for comparison. The grey region indicates where spectra in Figure 3.3(b) was measured. The background shows results of atomistic simulations of a retraction stage shown in Figure 3.4, for illustration.

suspended 2B-7aGNR was monitored during tip retraction z. At the initial stages of suspension (2B unit still on the surface), the current through the ribbon showed a weak exponential decrease with z (Figure 3.2c), as for pristine GNRs[17]. However, at a certain retraction length z_p, the current exhibited a pronounced peak, returning afterwards to the previous exponential decay. The peak and its position z_p were reproduced for several retraction/approach cycles of the same ribbon, and appeared in all

2B-7aGNRs studied. In every case, the value of z_p correlated with the distance between the 2B site and the contacted GNR-end (see SI in[127]), proving that the current peaks were caused by the detachment of a 2B moiety from the surface.
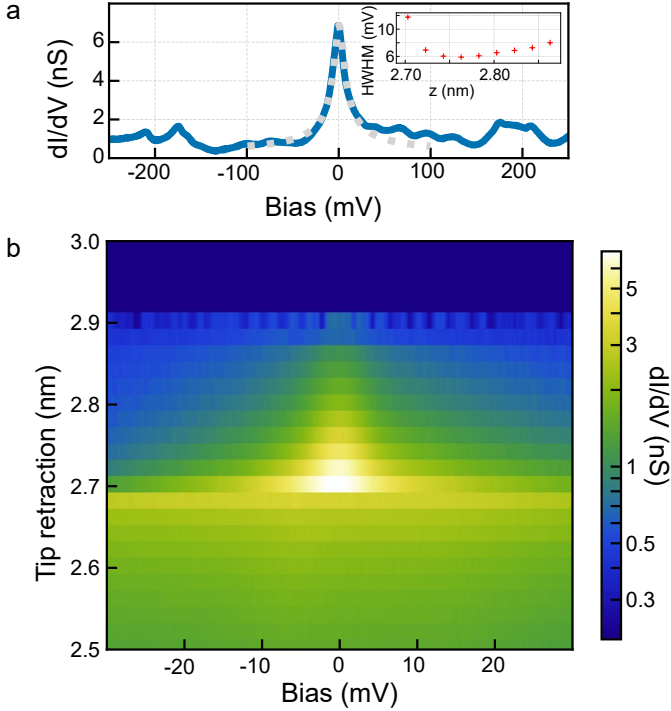

Figure 3.3: Emerging Kondo resonance in the suspended ribbon: a Spectrum over a larger bias interval, taken at $z = 2.70\,\mathrm{nm}$. The dotted grey line is a fitted Frota function[115] with HWHM $= 12 \pm 0.8\,\mathrm{mV}$. The fitting interval is $|V_b| < 20\,\mathrm{mV}$. The inset shows the evolution of the resonance's HWHM as a function of z. **b** Conductance through the GNR as a function of V_b and z. The corresponding height interval is the gray region indicated in Figure 3.2c. A zero-bias, narrow resonance is observed for $2.7\,\mathrm{nm} < z < 2.9\,\mathrm{nm}$.

To explore the origin of the anomalous current peak, we measured differential conductance $(\mathrm{d}I/\mathrm{d}V)$ spectra at positions around z_p (Figure 3.3). The $\mathrm{d}I/\mathrm{d}V$ plots show the emergence of a narrow zero-bias resonance in the spectra at $z_p = 2.7\,\mathrm{nm}$, which gradually decreases its amplitude with tip retraction, and disappears for $z > 2.9\,\mathrm{nm}$. The resonance remained pinned at zero bias in all the z range observed. Its
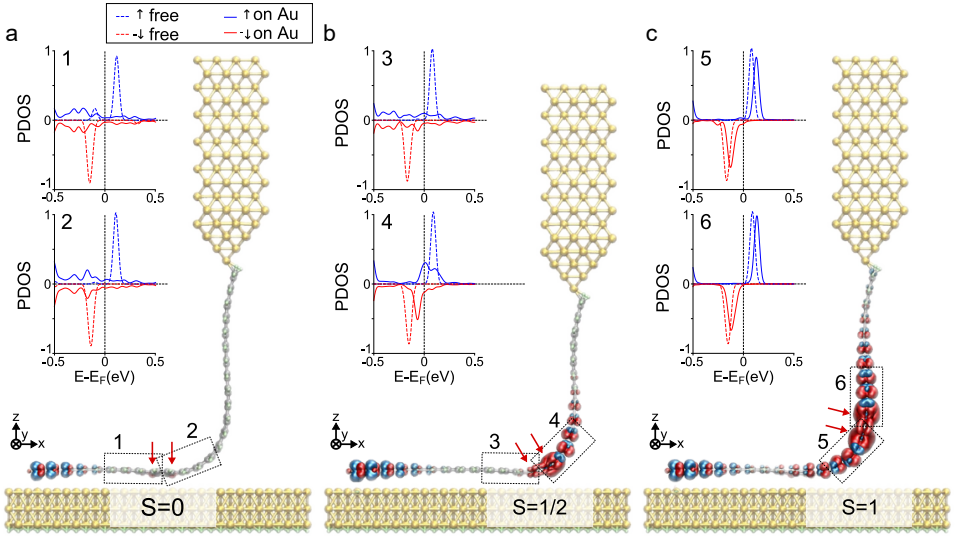
Figure 3.4: Spin-polarized density functional theory calculations of the suspended ribbon a-c Relaxed structures of three different configurations of a 2B-7aGNR bridging a gold tip and a Au(111) surface (red arrows indicate the position of the B heteroatoms). Constant spin density isosurfaces are shown over the atomic structure $(1.7 \times 10^{-3} \, e/\text{Å}^3$, spin up in blue and down in red). Insets compare spin PDOS over C atoms within the boxed regions around each boron atom for each bridge geometry (solid lines), with the corresponding one of a free 2B-7aGNR (dashed lines). The GNR zigzag termination on the surface holds a spin-polarized radical state, absent at the contacted end due the bond formed with the tip's apex[89]. The equivalent PDOS are provided for a wider energy window in the SI.

narrow line width reached a maximum value of $\Gamma_{\text{HWHM}} \approx 12.0 \pm 0.8 \, \text{mV}$ at z_p, and evolved non-monotonously with retraction z (Figure 3.3a) until disappearing. When the tip was approached below z_p, the resonance vanished abruptly, but it was recovered by increasing z back above the $z_\text{p} = 2.7 \, \text{nm}$ onset. From its narrow line shape and fixed zero-bias alignment, we conclude that the resonance is a manifestation of the Kondo effect[15,108,116]. A Kondo-derived resonance appears in $\text{d}I/\text{d}V$ spectra when a spin polarized state weakly interacts with the conduction electrons of an underlying metal[147].

To correlate these observations with the 2B-induced spin polarization predicted in Figure 3.1, we performed DFT simulations of a finite 2B-7aGNR suspended between a model gold tip and the surface of a Au(111)

slab (SI in[127]). Figure 3.4 shows the relaxed atomic structures of the GNR junctions before, while, and after detachment of a 2B unit, and includes the computed constant spin density isosurfaces. Before 2B-detachment from the surface ($z < z_p$, Figure 3.4a), the intrinsic magnetism around the 2B units is quenched: the PDOS in the regions 1 and 2 around each boron atom is broad and spin unpolarized, contrasting with the clear spin polarization of free ribbons (shown as dashed plots). This is caused by the strong hybridization of the B atoms with the gold surface[95,96], which appear $0.6\,\text{Å}$ closer to the surface than the carbon backbone.

The detachment of the 2B moieties from the metal surface causes the emergence of a net spin polarization, clearly reflected in their PDOS and spin density isosurfaces (Figure 3.4b, c). At the intermediate snapshot of Figure 3.4b, only one of the two B heteroatoms is detached from the surface, and the ribbon hosts a net spin $S = 1/2$ extending towards the free-standing segment (region 4). For the fully detached 2B case (Figure 3.4c), both regions around the two B atoms (regions 5 and 6) are spin polarized, recovering the $S = 1$ state of the isolated 2B-7aGNR (Figure 3.1b). Based on these simulations, we interpret that the most probable origin of the experimental Kondo resonance is the intermediate configuration pictured in Figure 3.4b. There, the Kondo effect is caused by the spin $1/2$ of region 4 interacting weakly with the surface when the first boron atom is detached. Although the $S = 1$ state of 3.4c could also produce a Kondo state[119], one would expect that it shows a larger extension and is accompanied by inelastic triplet-singlet side bands. Instead, the zero-bias resonance in the experiments disappears abruptly after a second kink $\sim 2\,\text{Å}$ higher (Figures 3.2c and 3.3b) that we associate with the cleave of the second B atom, in consistency with the B–B distance. The experimental results are thus consistent with the spin polarization around free-standing 2B moieties.

Although the Kondo signal vanishes quickly with retraction, DFT finds that the $S = 1$ state of the free ribbon remains, and is clearly favored over an antiparallel alignment by $\sim 14\,\text{meV}$ per isolated 2B pair. The presence of a triplet state is striking. The two spin clouds at each side of the 2B center extend symmetrically over opposite sublattices of the 7aGNR, what usually favors an antiparallel kinetic exchange[142]. A detailed analysis reveals that the hopping matrix elements between the two localized states at the sides of one 2B unit are very small ($t_{\text{intra}} \sim 18\,\text{meV}$,

see SI in[127]). Consequently, the moiety formed by a 2B-doped ring surrounded by two Clar sextets is a very stable element that blocks conjugated electrons from hopping across. This explains the presence of a magnetic state because the borylated element acts as a barrier for valence band electrons of the 7aGNR segments[97], and induces spin polarized boundary states due to the non-trivial topology of this band[20]. Additionally, the 2B barrier also disconnects the boundary states at each side, and hinders the (antiparallel) kinetic exchange between them. The stabilization of the triplet configuration is then the result of the weak direct overlap between both spin-polarized boundary states through the 2B barrier, which, due to the tiny hopping between them, dominates the exchange interaction and induces the ferromagnetic alignment of the spins according to Hund's rule.

3.3 Interacting Spins

We also studied GNRs with two consecutive 2B moieties like in Figure 3.5a, b, spaced by 1.2 nm. Transport experiments through these GNRs as a function of tip-sample distance (Figure 3.5c) also reveal deviations from an exponential decay with z, but now showing two peak features at retraction distances $z_{p1} \approx 1.60$ nm and $z_{p2} \approx 3.05$ nm. These values are related to the positions of the 2B units (nominally ~ 2.0 and ~ 3.2 nm from the contact point, respectively). A map of (normalized) differential conductance as a function of bias and z (Figure 3.5d) shows that both current features are also caused by narrow zero-bias dI/dV resonances appearing at ranges $z < 1.9$ nm and 2.9 nm $< z < 3.5$ nm, respectively. Their line shape (Figure 3.5e) is similar to the resonances observed for the single 2B case, and can also be attributed to Kondo states, which reflect the emergence of spin-polarization in the ribbon as each 2B unit is detached from the surface.

Although these results apparently suggest that each 2B behaves as an independent spin center, DFT simulations of free $(2B)_2$-7aGNRs (Figure 3.5b) find that the two singly-occupied boundary states between neighboring 2B elements interact strongly and open a large hybridization gap[96], forcing them into a closed shell configuration. As a consequence, the spin polarization vanishes between two 2B sites, but persists outside this region as two uncompensated spin 1/2 clouds (Figure 3.5b) with
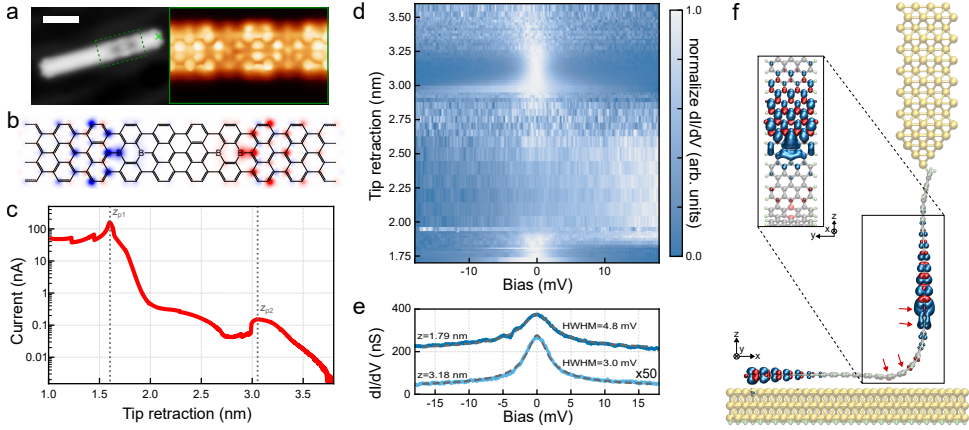
Figure 3.5: Interaction of two 2B-unis: a (Left) Constant current STM image of a borylated GNR ($V_b = -300\,\mathrm{mV}$, $I = 30\,\mathrm{pA}$). (Right) Constant height current image of the marked rectangular region ($V_b = 2\,\mathrm{mV}$) using a CO-functionalized tip. **b** DFT simulation of the magnetization of a $(2B)_2$-7aGNR. **c** Co-tunneling current I against z through the ribbon in **a** suspended between tip and sample. **d** Normalized differential conductance of the suspended $(2B)_2$-7aGNR as a function of V_b and z (see SI in[127]). Two zero-bias resonances are observed. **e** Representative $\mathrm{d}I/\mathrm{d}V$ spectra measured at the indicated z positions, with fits (dashed) using Frota functions[115]. **f** DFT relaxed structure of a suspended $(2B)_2$-7aGNR. Constant spin-density isosurfaces are shown over the atomic structure. Red arrows indicate the position of the B atoms. The inset shows the indicated region of the suspended GNR from a different angle.

barely no preferred relative spin alignment. From our electronic structure calculations ([96], SI in[127]) we can characterize this hybridization by a relatively large effective hopping term t_{inter} between boundary states of neighboring 2B units, which contrasts with the weak hopping t_{intra} across each 2B unit. In fact, the electronic structure close to the Fermi level of a sequence of borylated units can be mapped onto the Su-Schrieffer-Heeger (SSH) model[105], characterized by two alternating hoppings along a 1D wire. Since $t_{\mathrm{inter}} > t_{\mathrm{intra}}$, an alternative way to understand the spin-polarized states in Figure 3.5b is as zero-energy topological modes of a very short SSH chain. These simulations allows us to predict that an $S = 1$ spin chain will emerge for larger inter-2B spacing, when both hopping terms become smaller than the Coulomb charging energy U of the boundary states (SI in[127]).

To explore if inter-2B interactions survive in the experimental geometry, we simulated a $(2B)_2$-7aGNR suspended between tip and sample.

Figure 3.5f shows the spin polarization of a snapshot with one 2B moiety completely detached and the second partially bound to the surface. In contrast with the large spin cloud around the lifted single 2B in Figure 3.4c, here there is no spin density between the two 2B moieties, but a net $S = 1/2$ cloud above, confirming the presence of interactions between 2B units. The second $S = 1/2$ boundary cloud is expected to appear below the lower 2B only after the last boron atom is detached, being this responsible for the more extended Kondo effect observed in the experiment above z_{p2}. These results confirm the spin polarization predicted at the interface between $(2B)_2$ units and pristine 7aGNR segments[20], which in essence are zero-energy modes of the 7aGNR valence band of similar nature than those created by a single 2B unit at every side.

3.4 Conclusion

The peculiar spin polarization of single 2B units and dimers is a remarkable consequence of the large and long-range exchange interactions present in GNRs[20,89,148]. Our results support that spins survive in free-standing GNRs and can form $S = 1$ spin chains for low concentrations. Tuning the separation between 2B units is a promising strategy to control spin polarization through a change in the correspondence between inter-2B and intra-2B interactions. Furthermore, the stronger sensitivity of substitutional boron heteroatoms to chemical bonding endows these systems with ideal properties to manipulate complex spin states in chains.

4 Topological Phase Reversal of a Borylated Graphene Nanoribbon on a Metal Substrate

Graphene nanoribbons are potential platforms for π magnetism. Recent results have shown that uncompensated spin-polarized states may appear at the edges or the interior of ribbons due to non-conventional band topology effects. Here, we report on the induction of spin polarization in a semiconducting ribbon when it is detached from a metal support. A combination of density functional theory calculations, mean-field Hubbard simulations and low temperature STM transport experiments through a borylated GNR demonstrate that spin states appear at the boundary between a free standing and a on-surface GNR. These spin states are the result of substrate mediated hopping processes. The otherwise blocked movement of the valence band electrons is enabled resulting in the formation of a spin polarized topological state emerging in close proximity to the substrate. These results support that borylated ribbon can be treated as an SSH chain, where spin states emerge by selective cutting the chain at specific sites.

- *Topological Phase Reversal of a Borylated Graphene Nanoribbon on a Metal Substrate*

  Niklas Friedrich, Pedro Brandimarte, Jingcheng Li, Lorenz Meyer, Eduard Carbonell-Sanromà, Martina Corso, Iago Pozo, Diego Peña, Thomas Frederiksen, Aran Garcia-Lekue, Daniel Sánchez-Portal, and José Ignacio Pascual

  Manuscript in preparation

4.1 Introduction

In the previous Chapter the topological origin of spin-polarized states in 7aGNR with dilute 2B doping was discussed. Topological protected states in graphene nanoribbons are particularly interesting for spintronic applications, as these states are stable against small, external perturbations. The substitutional boron doping of a 7aGNR by a single 2B-unit removes two electrons from the π conjugation of the valence band (VB) electrons and stabilizes two Clar sextets at the sides of the boron moiety. As a result, VB electrons are effectively blocked in their free propagation at the boron doping position and a topological end state forms inside the ribbon. As we saw in the previous Chapter, the two states on each side of a diboron (2B) unit couple ferromagnetically due to Coulomb exchange. Dilute doping creates a one dimensional chain of $S = 1$ states that only weakly interact.

At slightly increased doping densities, the single $S = 1$ spins interact stronger and form an antiferromagnetically coupled spin chain (SI in[127]). The spin polarization is quenched, when the coupling between the different sites becomes larger than the on-site Coulomb correlations. Spins of adjacent 2B-units form a closed shell configuration, the ribbon becomes topologically trivial and two extended impurity induced flat bands form in the GNR[96]. They do not host any potential for building up magnetism due to their large energy spacing by $\sim 1\,\text{eV}$. On a metal substrate, the boron derived flat bands broaden due to hybridization, but their alignment remains essentially the same and no spin texture builds up.

In this Chapter, we show that a spin-polarized state with $S = 1/2$ can be induced inside a GNR with dense boron doping (referred to as $(2B)_d$-GNR)[94–98,127,149,150] at the interface between a free-standing segment and one that is absorbed on a metal substrate. The spin-polarized state is detected as an emerging Kondo signal in two-terminal transport experiments with a GNR suspended between tip and substrate of a low temperature scanning tunnelling microscope. We reproduce this behaviour by density functional theory (DFT) calculations and rationalize the findings within a mean-field Hubbard (MFH) model.

The presence of the spin-polarized state can be interpreted in a simple SSH-model[105]: The hybridization with the substrate enables additional hopping channels surpassing the boron induced barrier. This allows the

π-electrons to move freely along the ribbon backbone, a behaviour resembling the one of an undoped 7aGNR. The boron doping in the free-standing segment of the ribbon blocks the electronic conjugation, an effect comparable to a topological transition. A protected edge state emerges at the interface between the two segments. The edge state's position inside the $(2B)_d$-GNR moves sequentially through different position in the ribbon during the retraction process.

4.2 A Kondo Resonance Measured in a Topologically Trivial Ribbon

The GNRs analyzed in this Chapter were prepared using only the borylated precursor molecules (see Section 1.1.4), resulting in one 2B-unit per three anthracene units of the 7aGNR[94–96,149]. Figure 4.1a presents the STM topography image of a seven unit long $(2B)_d$-GNR and its Lewis structure. The 2B sites appear as depressions along the GNR[95]. The cross at the termination indicates the position where we approached to lift the ribbon following the procedure described in Section 1.1.3. The successful lifting trajectory followed approximately a 45° angle with respect to the surface plane. Most likely, this large angle is caused by the strong interaction of the 2B-units with the substrate making it more favorable to break the single tip-ribbon bond than to reconfigure all diboron-surface absorption positions[16,18,95,96].

The low-bias linear conductance G through the ribbon decreases exponentially with increasing z as seen in Figure 4.1b. Superimposed on this, three local maxima of conductance are located at 0.9 nm, 1.9 nm and 2.8 nm (as indicated by the dashed, vertical lines). The equidistant spacing with $\Delta z \approx 1$ nm is compatible with the spacing of the 2B-units in the GNR and suggests that they are induced by the detachment of borylated units from the substrate. Between the maxima, several step features are attributed to mechanical relaxations of the GNR-substrate bonding during the lifting process[16,18].

Measuring dI/dV spectra at the local conductance maxima reveals a zero-bias resonance that can be described by a Frota lineshape (Figure 4.1c). As mentioned in Section 1.2.4, this type of resonance is a fingerprint of a Kondo resonance stemming from the weak interaction of
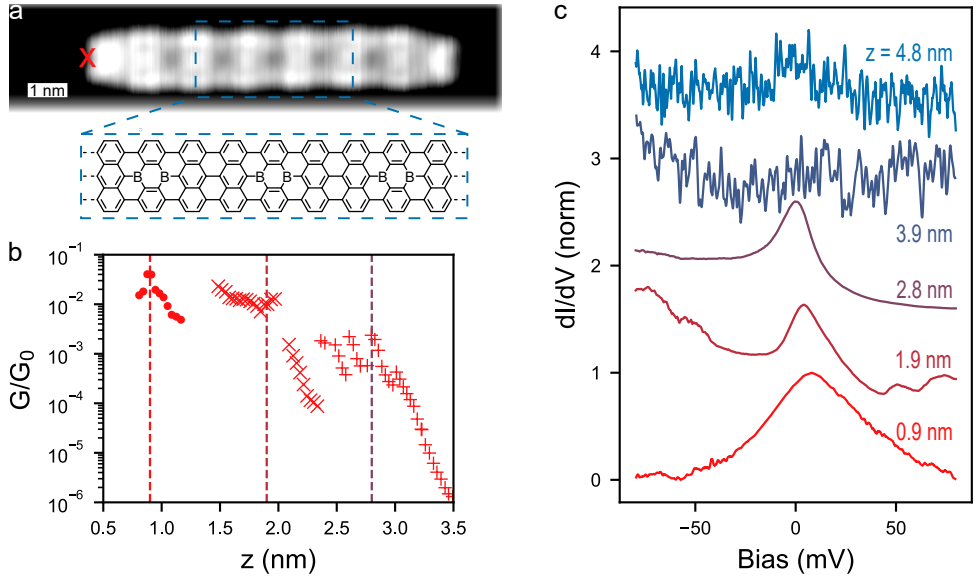
Figure 4.1: Three Kondo resonnaces in two-terminal transport a STM constant current topography image of the $(2B)_d$-GNR ($V_b = -300\,\mathrm{mV}$, $I = 30\,\mathrm{pA}$). The red cross indicates the position where the tip was approached for cleaving. **b** $G(V = 5\,\mathrm{mV})$ as a function of z. The values are extracted from $\mathrm{d}I/\mathrm{d}V$ spectra taken during the lift of the ribbon in **a**. Three local maxima in G are identified at $z \approx 0.9\,\mathrm{nm}$, $2\,\mathrm{nm}$ and $2.8\,\mathrm{nm}$. **c** Normalized $\mathrm{d}I/\mathrm{d}V$ spectra taken at different z showing Fano-shaped Kondo resonances, z values are indicated in the figure. The separation of $z \approx 1\,\mathrm{nm}$ matches the separation of 2B sites in the $(2B)_d$-GNR. Spectra are vertically offset for clarity.

a spin-polarized state with an electron bath[108]. The zero-bias resonance disappears from the $\mathrm{d}I/\mathrm{d}V$ spectra at intermediate z. The combination of a zero-bias resonance and increased low-bias conductance in a two-terminal transport configuration mimics the fingerprint of a topological edge state inside a 7aGNR with one or two embedded 2B-units presented in the previous Chapter and in[127]. The $\mathrm{d}I/\mathrm{d}V$ spectra recorded at $z > 3.5\,\mathrm{nm}$ show very low conductance and therefore are not conclusive about the presence of a Kondo resonance.

First Principles Simulations of the Retraction of the Ribbon

Neither the fully free-standing, nor the fully absorbed GNR show any spin polarization. Therefore, the emergent spin polarization is intrinsically associated to the interface between the free-standing and absorbed segment of the ribbon and appears periodically during the retraction of the ribbon. To investigate the origin of the spin polarization we perform density functional theory calculations using a simplified geometry grasping the important physics.

First, we analyze the emergence of spin polarization around a single 2B-unit in the $(2B)_d$-GNR during detachment from a surface. We model the lifting process by the stepwise removal of a gold slab below the ribbon without relaxing the structure. Figure 4.2a shows four different stages of removal. In a_1, the diboron unit is about to detach from the surface, but one boron atom is still above the last gold atoms. In the next step (a_2), there is one free-standing anthracene unit between the last gold atoms and the first free-standing boron atom. Neither of these structures develops a spin polarization. In the structure in Figure 4.2a_3, two free-standing anthracene units are located between the gold slab and the free-standing boron atoms. In this scenario, a spin polarization resembling the form the topological edge state of the pristine 7aGNR emerges in the two free-standing anthracene units between gold slab and 2B-unit. Removing another single row of atoms from the gold slab, and thus detaching one boron atom from the slab, quenches the spin polarization again.

Reproducing what we observe in experiment, the spin polarization appears periodically when removing the gold slab step by step below the GNR. Figure 4.2b–f presents the DFT model of the cleaving process. The relative alignment of slab and last absorbed 2B-unit is identical in all cases where spin polarization is observed. Two free-standing anthracene units need to be available between the gold slab and the closest free-standing 2B-unit to host spin polarization in the $(2B)_d$-GNR. Other absorption geometries do not result in spin polarization in the ribbon.

The spatial distribution of the spin polarization found by DFT calculations resembles the one of topological end states in 7aGNR[20,127]. DFT calculations show no charge transfer between a $(2B)_d$-GNR and a Au(111)[96], excluding a band (de-) population that might change the
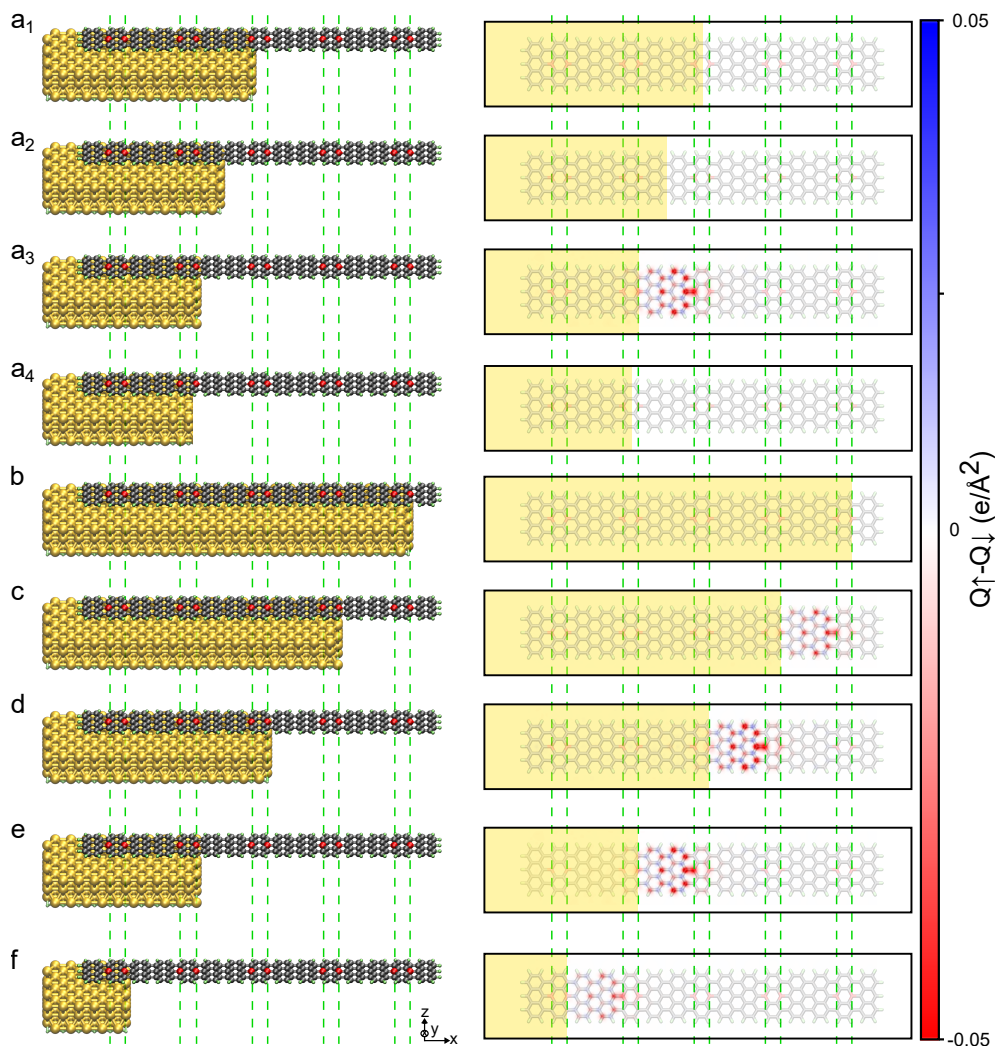
Figure 4.2: Spin polarization in DFT simulations of the retraction a DFT calculations model the cleaving process by removing an Au(111) slab atomic layer-by-layer below a $(2B)_d$-GNR. The spin-polarization emerges in the configuration where two antracene units are free-standing between the last 2B and the Au slab. Detaching the next boron atom from the substrate completely quenches the spin. **b-f** The spin-polarization re-emerges for each 2B-unit in the ribbon, exactly when there are two free-standing anthracene units, explaining the periodic presence of a Kondo resonance during the cleaving process.

ribbon's Berry phase. Nevertheless, the appearance of the end state at the interface between the free-standing and absorbed segments suggests a recovery of the pristine valence band in the absorbed segment of the ribbon. In the previous Chapter, we found that the high energy barrier of the boron moiety for VB electrons is responsible for the topological end state. The hybridization induced band broadening[96] lowers this energy barrier sufficient for valence band electrons to surpass the boron moiety and propagate through the ribbon. This might cause the emerging end state at the interface to the free-standing segment of the ribbon.

4.3 Mean-Field Hubbard Model of the Substrate Hybridization

We simulate the effect of the Au(111) substrate in the framework of a mean-field Hubbard model, where the additional electronic channels introduced by the hybridization of ribbon and substrate are modelled directly by modifying the corresponding hopping amplitudes connecting different atomic sites. To identify the hopping amplitudes that affect the low-energy boron states strongest, we start with a finite 7aGNR with a single 2B-dopant in its center. First, we obtain its energy spectrum in a pure tight-binding picture (in the absence of Coulomb repulsion U) and identify the two boron states (left panel in Figure 4.3a). We see a small hybridization of the two end states on either side of the 2B-unit, opening a small gap between them. Next, the energy of the two states is modified slightly (indicated by the arrows in Figure 4.3a), simulating the increased hybridization by the substrate. A unitary basis transformation propagates the change of eigenenergies into real space and we obtain a template set $\{\tilde{t}_i\}$ of modified hopping amplitudes $\tilde{t}_i$. We restrict the calculations to the $\tilde{t}_i$ with the three largest values, corresponding to the black lines in Figure 4.3b and assume them to have identical value $\tilde{t}_i = \tilde{t}$ (see Section 4.5 for details).

Having identified the hopping amplitudes $\{\tilde{t}\}$ that reproduce the substrate induced changes to the bandstructure on a single 2B-unit, we return to a ribbon with dense 2B doping and simulate its partial absorption on a Au substrate (Figure 4.3c). We start from the tight binding Hamiltonian of a finite $(2B)_d$-GNR and add the template set $\{\tilde{t}\}$ at two of the
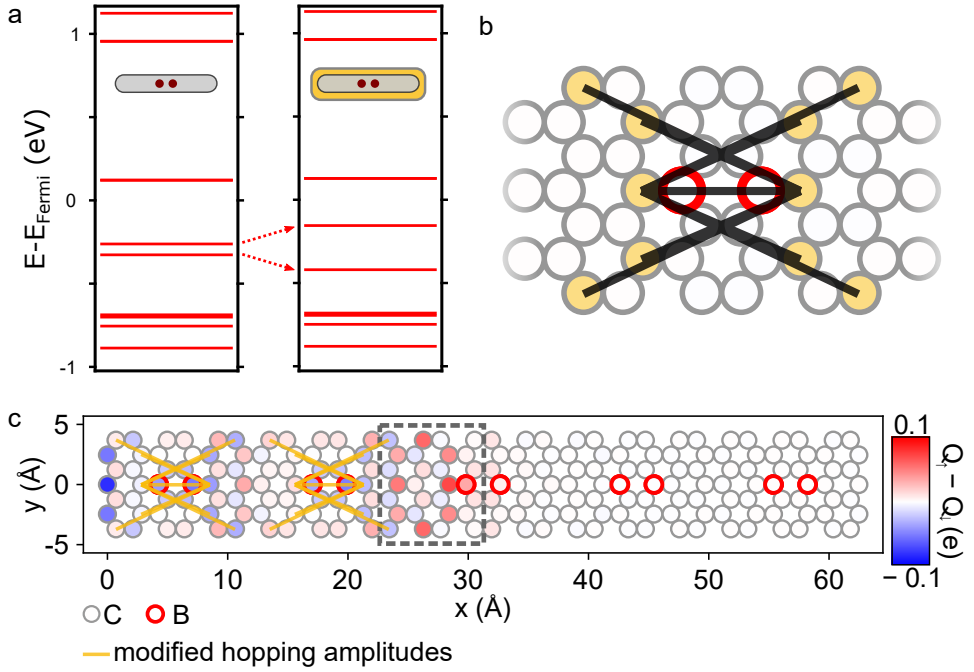
Figure 4.3: Substrate mediated hopping processes simulated in the MFH model:
a Energy spectrum of the kinetic part of the Hubbard Hamiltonian ($U = 0$) of a 7aGNR with a single 2B-unit for the free-standing (left) and hybridized case (right). **b** Segment of a 2B-7aGNR. The boron atoms are indicated in red. The black lines represents $\{\tilde{t}\}$, *i.e.* the set of hopping amplitudes that are affected strongest by the hybridization. Yellow circles highlight the carbon atoms associated to $\{\tilde{t}\}$. **c** MFH calculations of a partially lifted ribbon. Hopping elements around the two left 2B-units were modified by $\tilde{t} = 0.8\,\mathrm{eV}$ using the template shown in **b**. A spin polarization resembling the one of topological edge states in 7aGNR appears at the interface region indicated by the dashed line.

five 2B-units (yellow lines in Figure 4.3c), before constructing the MFH Hamiltonian. Upon slowly increasing the value of the hopping amplitude $\tilde{t}$, a spin polarization emerges at $\tilde{t} \sim 500\,\mathrm{meV}$. The localization of the spin polarization, indeed, resembles the one of the spin-polarized topological end states in dilute 2B-doped GNRs[20,127].

Topological Character of the Spin Polarization

To confirm the topological character of the spin polarization, we map the topological states associated to the 2B-units and ribbon termini on an

SSH model[105] (Figure 4.4a). The states form a one dimensional chain of singly occupied sites that are connected by hopping parameters of alternating strength (t_{2B} and t_{GNR}). The relation between the t_{2B} and t_{GNR} defines the topological character of the ribbon as being trivial ($t_{GNR}>t_{2B}$) or non-trivial ($t_{2B}>t_{GNR}$). We extract values for the two hopping parameters by fitting an SSH-bandstructure to the two frontier bands of the ribbon obtained by MFH calculations of the periodic $(2B)_d$-GNR (see Section 4.5) and study their evolution with the hopping amplitude $\tilde{t}$.
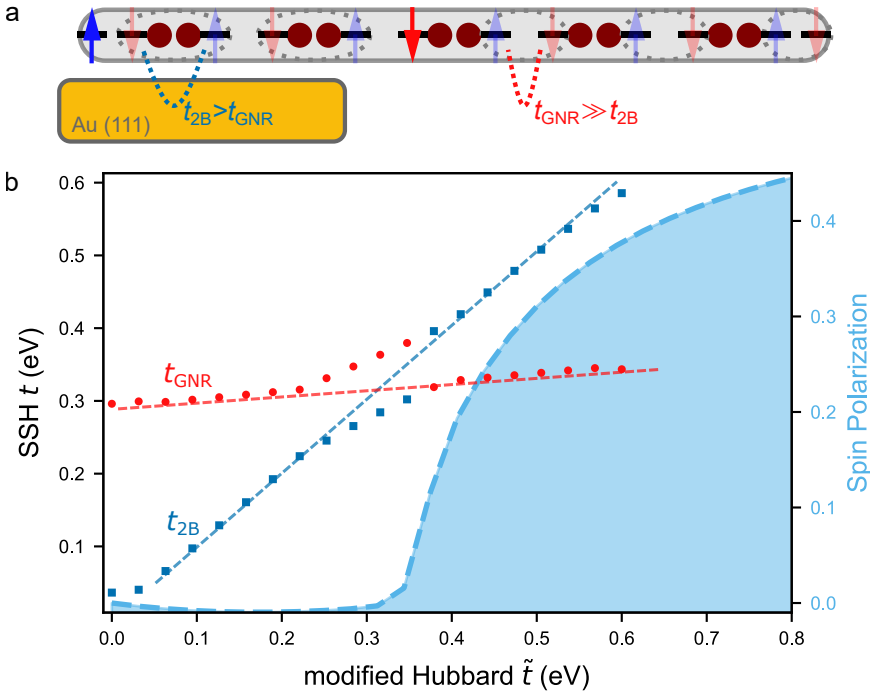

Figure 4.4: Mapping the MFH onto an SSH model: a SSH model of partially absorbed ribbon. For each boron atom (dark red circle) one additional single electron site (black line) is available. The different sites are connected by the two hopping amplitudes t_{GNR} and t_{2B}. Two electrons form a closed shell configuration in a single 2B-unit in the region where $t_{2B} > t_{GNR}$, and in the short, undoped segment of the GNR where $t_{GNR} > t_{2B}$, as indicated by the dotted circles. One unpaired spin at the interface of the two regions gives rise to a topologically protected edge state. **b** SSH model hopping parameters t_{GNR} and t_{2B} as a function of $\tilde{t}$ extracted from MFH calculations of a periodic $(2B)_d$-GNR. The dashed lines serve as a guide to the eye. A topological transition takes place at $\tilde{t} \sim 300\,\text{meV}$. The dashed line corresponds to the integrated spin polarization in the interface region (grey, dashed rectangle in Figure 4.3c) of a long $(2B)_d$-GNR (presented on the right axis).
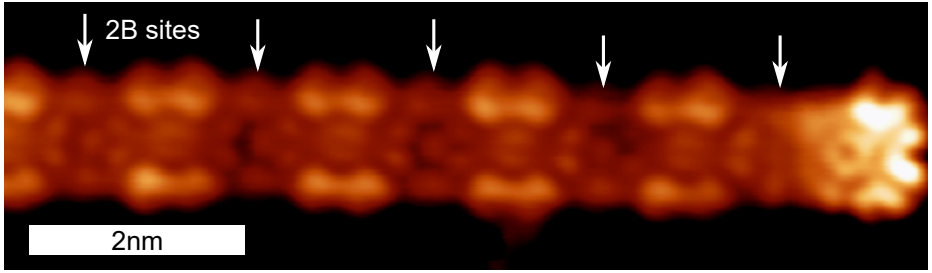
Figure 4.5: Edge state in a (2B)$_d$-GNR: STM constant height current image of the edge state of a densely 2B-doped GNR. ($V_b = 5\,\mathrm{mV}$).

We find that the perturbation of the surface simulated by increasing $\tilde{t}$ increases the hopping across the 2B-unit t_{2B} approximately linearly (blue symbols in Figure 4.4b), while t_{GNR} remains constant (red symbols). This trend results in a topological transition taking place at $\tilde{t} \sim 300\,\mathrm{meV}$. Combining the findings from the SSH model and the MFH model simulations, we can explain the physical reasons behind the observed spin polarization. The free-standing segment of the ribbon (right end in Figures 4.3c, 4.4a) is determined by $t_{GNR} > t_{2B}$ and the electrons from closed shell configurations in the short, pristine segments between two 2B-units (dotted circles in Figure 4.4a). The relation between the hopping amplitudes inverts to $t_{2B} > t_{GNR}$ for electrons in the absorbed segment of the ribbon (left end in Figures 4.3c, 4.4a). Now, the closed shell configuration is formed by electrons on the same 2B-unit. The change between the two configurations leaves one unpaired electron at the interface of the free-standing and absorbed segment, resulting in the observed spin-polarization.

The dashed curve in Figure 4.4b presents the spin polarization in region indicated by the dashed rectangle of the short GNR shown in Figure 4.3c. The onset of spin polarization appears to be slightly delayed with respect to the topological transition at $\tilde{t} \sim 300\,\mathrm{meV}$. This difference is caused by Coulomb interaction between the two topological end states of this short GNR. In a much longer system, such interaction is negligible and the spin polarization coincides with the topological transition of the periodic system (Figure 4.4b, see also Section 4.5, Figure 4.10).

In addition, both the MFH model and the SSH model predict a second topological end state forming at the absorbed termination of the ribbon. This state cannot be probed by transport experiments on the suspended

ribbon, but should be detectable as a low bias feature in STM images of the absorbed ribbon. Indeed, as we shown in Figure 4.5, we observe a low energy state located at the termination of a borylated GNR absorbed on a Au(111) substrate that resembles the low-bias end state observed in undoped 7aGNRs[151].

4.4 Conclusions

In this Chapter, we have shown the possibility to form a spin-polarized state within a single GNR, which is not expected to host any spin polarization. We observe the presence of a Kondo resonance for specific tip-substrate distances while slowly lifting a $(2B)_d$-GNR from a Au(111) substrate using the tip of a scanning tunneling microscope and associate this to a periodically emerging spin polarization. DFT calculations of a partially absorbed $(2B)_d$-GNR reproduce the periodic presence of spin-polarized states during the lifting process. To study the role of substrate hybridization on the band structure, we modelled the behaviour in a MFH model, where substrate hybridization is simulated by additional hopping channels. We found that the interaction of the boron dopants with the substrate enables the propagation of electrons across diboron units of the ribbon which otherwise is blocked in the free-standing segment of the GNR. As a result, the adsorbed and free-standing segments of the ribbon behave as with different topological character and a spin-polarized edge state builds up at the interface. The electron motion in the partially absorbed ribbon can be mapped on an SSH model, further supporting the topological interpretation of the results. Therefore, we provided a route to arbitrarily alter the position of a spin-polarized topological edge state inside a graphene nanoribbon.

4.5 Appendix

Modelling the Au(111) Substrate in the Mean-Field Hubbard Model

In the following we discuss details on the mean-field Hubbard (MFH) calculations. The general details of the MFH model are presented in

Section 1.2.5. We used the parameters $U = 3.5\,\mathrm{eV}$, $t_1 = 2.7\,\mathrm{eV}$, $t_2 = 0.2\,\mathrm{eV}$, $t_3 = 0.18\,\mathrm{eV}$.
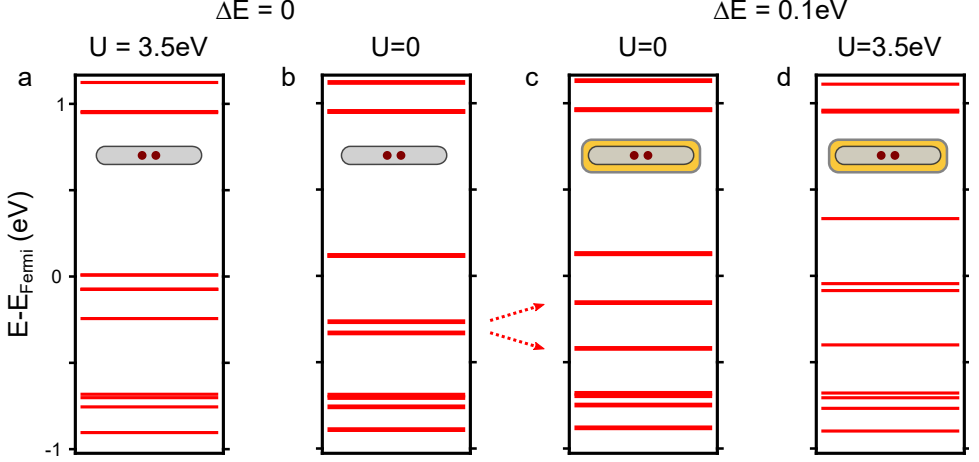

Figure 4.6: **Substrate hybridization of the 2B-state:** Energy spectrum of the 15 anthracene unit long, singly 2B-doped 7aGNR obtained in the MFH model. **a, b** MFH calculations using $U = 3.5\,\mathrm{eV}$ and $U = 0$. **c** MFH energy spectrum ($U = 0$) after shifting them by $\Delta E = 0.1\,\mathrm{eV}$ to model the increased interaction due to substrate hybridization. **d** MFH calculations using $U = 3.5\,\mathrm{eV}$ of the system in **c**. The hybridization is sufficient to change the ground state spin-polarization of the ribbon. The spectra in **b** and **c** are shifted vertically for easier comparison.

The hybridization of ribbon and substrate is simulated by a modification of the standard MFH calculation. We obtain the energy spectrum of a finite 15 anthracene unit long 7aGNR with a single 2B-dopant in its central anthracene unit by diagonalizing the kinetic tight-binding part, *i.e.* $U = 0$ (Figure 4.6b). We refer to the diagonalized Hamiltonian as H_E. Next, we identify the two states associated to the 2B-unit and shift their energies in H_E by $\pm\Delta E$ (Figure 4.6c). The modified real-space Hamiltonian $H' = V^T H'_E V$, where V is the unitary matrix transforming the Hamiltonian from the eigenspectrum in energy-space to real-space, represents the hybridization caused by the substrate in real space.

The difference $H - H'$ yields a set of hopping amplitudes $\{\tilde{t}^*\}$ that is the real space equivalent of the modification of the energy spectrum. Figure 4.7 shows the reduced set $\{\tilde{t}\}$ corresponding to the three largest values in the set $\{\tilde{t}^*\}$. In the following calculations, we use the reduced set $\{\tilde{t}\}$ to simulate the substrate hybridization, omitting any numeri-
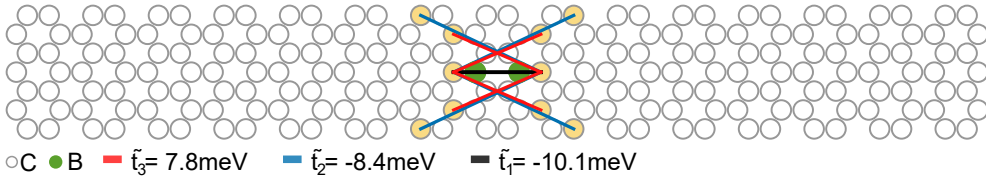
○C ● B ▬ $\tilde{t}_3$= 7.8meV ▬ $\tilde{t}_2$= -8.4meV ▬ $\tilde{t}_1$= -10.1meV

Figure 4.7: Hopping amplitudes modified by the hybridization wit the substrate:
Subset $\{\tilde{t}\}$ of the modified hopping amplitudes $\{\tilde{t}^*\}$ for a 15 anthracene unit long, singly 2B-doped 7aGNR. Only the three largest values of $\tilde{t}_i$ are included. The numerical values are given for a hybridization of $\Delta E = 0.1\,\mathrm{eV}$.

cal differences between the individual $\tilde{t}_i$. We found empirically, that more complex models including a larger subset of $\{\tilde{t}^*\}$ or considering the numerical differences between $\tilde{t}_i$ does not improve the results of the simulation significantly.

To simulate the partially absorbed $(2B)_d$-GNR, we constructed the MFH Hamiltonian with $U = 0$ and added the set of real-space hopping amplitudes $\{\tilde{t}\}$ to the Au-absorbed 2B-units. Afterwards, the mean-filed terms are included using $U = 3.5\,\mathrm{eV}$ and the eigenvalue problem of the resulting Hamiltonian is solved self-consistently. The effect of U is detailed in Figure 4.6. The four states around E_{Fermi} reorganize when solving the MFH Hamiltonian with finite U (Figure 4.6a, d) as compared to evaluating it with $U = 0$ (Figure 4.6b, c) both in the absence (a, b) and presence (c, d) of substrate hybridization. These four states are the ones responsible for spin-polarized low-energy states in the ribbon.

Mapping From the Mean-Field Hubbard Model to the SSH Model

The following Section discusses the construction of the SSH model presented in this Chapter in greater detail. A general introduction to the SSH model is found in Section 1.2.3. We start by considering a pristine 7aGNR. There will be two electron sites available, which correspond to the topological end states located at the termini of the ribbon. Every 2B-unit that is induced provides another set of two electron sites, again, arising from the two topological states at each side of the 2B-unit as we saw in Chapter 3. The electrons located at the different sites are allowed to move freely from site to site. The probability of the electron move-

ment is parametrized by the two hopping amplitudes t_{2B} and t_{GNR} (see Figure 4.4).
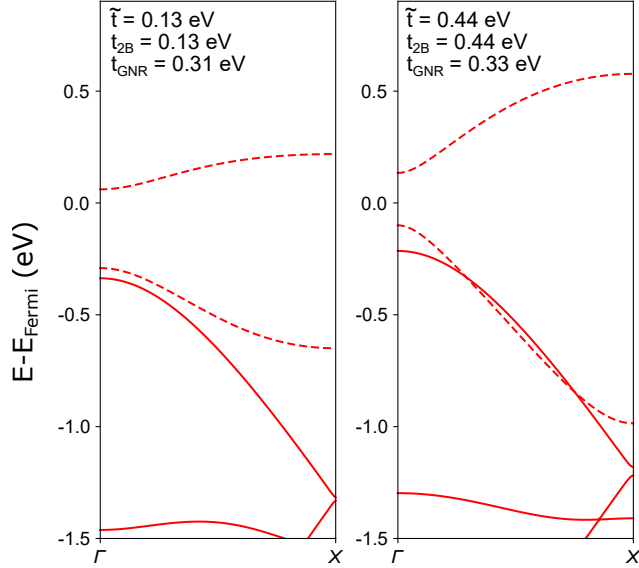

Figure 4.8: MFH band structures used for fitting the SSH model: Band structure of the periodic 2B-7aGNR obtained by MFH calculations with a hybridization of $\tilde{t} = 0.13\,\text{eV}$ (left) and $\tilde{t} = 0.44\,\text{eV}$ (right). The frontier bands are indicated by the dashed lines. The SSH parameters extracted from the band structure are given in the plot.

We calculate the band structure of a periodic ribbon with a three anthracene unit long unit cell containing one 2B-unit in the central anthracene of the unit cell in the MFH model. The hybridization of the substrate is simulated as described above, constructing first the kinetic part of the Hamiltonian, adding $\{\tilde{t}\}$ and then evaluating the MFH Hamiltonian including finite U. The two frontier bands have approximately sinusoidal shapes (Figure 4.8 and we can obtain the two parameters of the SSH model *via*

$$t_1 = E_\Delta$$
$$t_2 = E_{\text{gap}}/2 + E_\Delta,$$

where E_Δ is the averaged width of the two bands and E_{gap} is the gap between the two bands. *A priori*, it is not possible to assign t_1 and t_2 to t_{2B} and t_{GNR} considering only a single calculation. However, it is

possible to correctly assign the hopping amplitudes when studying their behaviour as the hybridization $\tilde{t}$ is slowly turned on. The presence of the Au substrate affects t_{2B} directly (by construction in the MFH model), but will have relatively little influence on t_{GNR}.

Figure 4.9 shows the onset of spin polarization in the short ribbon presented in Figure 4.3c together with the SSH hopping amplitudes extracted from the calculations of the periodic system. The onset of spin polarization is delayed with respect to the topological transition in the periodic system. This is due to the finite Coulomb interaction between the two end states. The spin polarization in the ribbon emerges more quickly, when the states are separated further from each other, as Figure 4.10 shows.
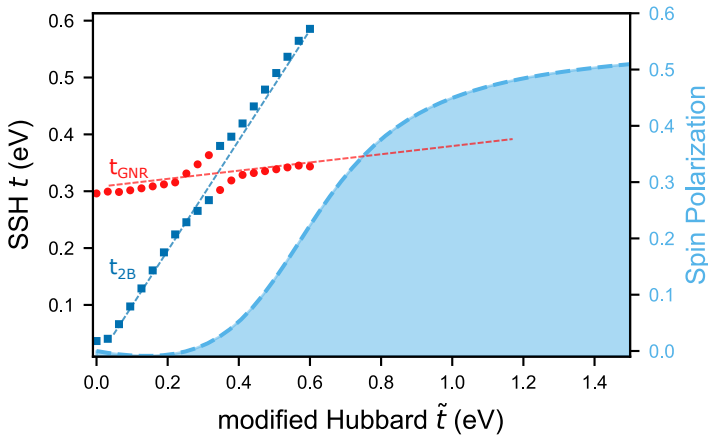
Figure 4.9: SSH hoping parameters and spin polarization: SSH model hopping parameters t_{GNR} and t_{2B} as a function of $\tilde{t}$. A topological transition takes place at $\tilde{t} \sim 300\,\mathrm{meV}$ (same as Figure 4.4b). The cyan, dashed line presents the integrated spin polarization in the interface region of a short densly 2B-doped GNR (indicated by the dashed rectangle in Figure 4.3c). The onset of spin polarization is delayed with respect to the topological transition due to the Coulomb interaction between the two end states.
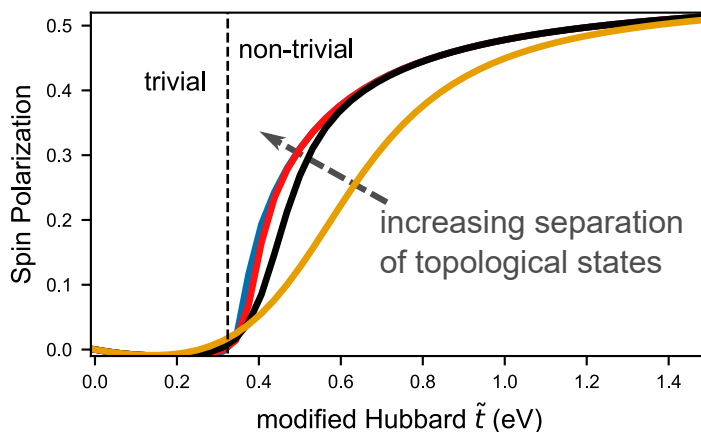
Figure 4.10:   Spin polarization for ribbons with different hybridization lengths: Integrated spin-polarization in the interface region of a 60 anthracene units (20 2B-units) long ribbon as a function of $\tilde{t}$. The hopping elements crossing the left most two (yellow), five (black), ten (red) and 17 (blue) 2B-units were modified. A sharper onset of spin polarization is observed due to the reduced Coulomb interaction between the two end states. The topological transition is indicated by the dashed vertical line at $\tilde{t} = 324\,\mathrm{meV}$.

5 Addressing Electron Spins Embedded in Metallic Graphene Nanoribbons

Spin-hosting graphene nanostructures are promising metal-free systems for elementary quantum spintronic devices. Conventionally, spins are protected from quenching by electronic bandgaps, which also hinder electronic access to their quantum state. Here, we present a narrow graphene nanoribbon substitutionally doped with boron heteroatoms that combines a metallic character with the presence of localized spin 1/2 states in its interior. The ribbon was fabricated by on-surface synthesis on a Au(111) substrate. Transport measurements through ribbons suspended between the tip and the sample of a scanning tunnelling microscope revealed their ballistic behavior, characteristic of metallic nanowires. Conductance spectra show fingerprints of localized spin states in form of Kondo resonances and inelastic tunnelling excitations. Density functional theory rationalizes the metallic character of the graphene nanoribbon due to the partial depopulation of the valence band induced by the boron atoms. The transferred charge builds localized magnetic moments around the boron atoms. The orthogonal symmetry of the spin-hosting state's and the valence band's wavefunctions protects them from mixing, maintaining the spin states localized. The combination of ballistic transport and spin localization into a single graphene nanoribbon offers the perspective of electronically addressing and controlling carbon spins in real device architectures.

The following Chapter is published as an article in the journal **ACS Nano**. Adopted under CC-BY 4.0.

5.1   Introduction

Graphene nanoribbons (GNRs) are narrow stripes of graphene a few nanometer wide. In spite of graphene being inherently a semimetallic material, electronic correlations and confinement of their electrons into one dimension generally result in gapped band structures[82,83]. Since the bandgap depends on the GNR's orientation, edge and width[83–87], precise control of their semiconducting character can be achieved by on-surface synthesis methods[21,23,26,87,152].

In the last years it has been proposed that GNRs can also host localized spin states at specific positions of their carbon lattice, turning them into potential candidates for metal-free spintronic devices[20,88,153,154]. Spin states have been found in GNRs and in graphene nanoflakes, mostly localized around zig-zag edges and various defects[89,119,126,127,148,155–170]. Two-terminal electronic transport measurements using a scanning tunnelling microscope (STM) have demonstrated that spins can be addressed by electrons tunnelling through the GNR's bandgap[127,146]. Although a bandgap favors spin localization, it restricts low-energy electron movement to distances of a few angstroms. This limits the integration of spin-hosting GNRs into spintronic devices. Ballistic transport through metallic graphene nanoribbon[171–173] would ease the implementation by facilitating the read out of the embedded spins.

Here, we report on the detection of localized spins in metallic GNRs realized by substitutionally doping a narrow-bandgap GNR with boron atoms in its interior. The boron heteroatoms turn the ribbon metallic and, at the same time, acquire a net magnetic moment. Density functional theory (DFT) calculations reveal that the spin is protected from the partially filled valence band (VB) by the different symmetry of the VB and the boron bands. Pentagonal defects, as those observed in the experiment, break the structural symmetry and open small hybridization gaps in the VB close to the Fermi level. We combined two-terminal transport experiments with differential conductance (dI/dV) spectroscopy to probe the electronic and magnetic properties of individual GNRs. Ballistic transport was stable over distances of several nanometers. The presence of a Kondo resonance proves access to the spin at a transport length of more than 3 nm.

5.2 Fingerprints of Magnetism in Ballistic Transport Through 2B-575-aGNRs

The atomic structure of the investigated ribbon is derived from that of a 7-atom wide armchair GNR (7aGNR) with substitutional boron doping at periodic intervals[94–98,149,150,166]. Here, we modified the edge structure and width of the undoped 7aGNR by periodically alternating five and seven carbon atom wide segments (575-aGNR, Figure 5.1a). DFT calculations of the electronic band structure, shown in Figure 5.1b, predict that the undoped GNR has a small bandgap, with no spin polarization. Interestingly, the wavefunction of both valence and conduction bands are antisymmetric with respect to the central axis of the ribbon (Figure 1c), in contrast with the symmetric character of frontier bands in the related 7aGNR[96]. This change in the bands' symmetry turns out to be crucial to understand the effect of boron substitution inside the GNR.
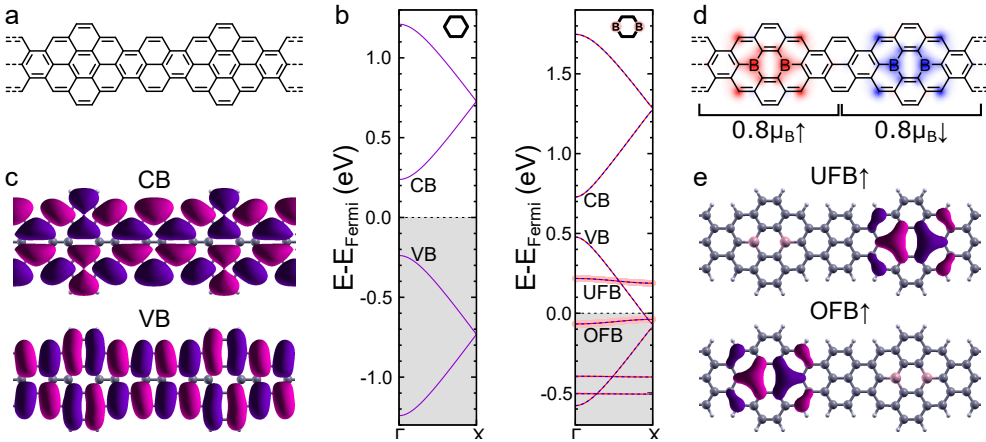
Figure 5.1: DFT calculated band structure of the 2B-575-aGNR a Lewis structure of the proposed 575-aGNR without boron doping. **b** Spin-polarized DFT calculated band structure of the 575-aGNR and the 2B-575-aGNR using a doubled supercell like shown in panel **a**. Boron character of the bands is indicated by a pink shadow. **c** DFT calculated wavefunctions at Γ of the CB and VB of the 575-aGNR. **d** Lewis structure of the 2B-575-aGNR shown on top of a color map representing the calculated spin-polarization density. **e** DFT calculated wavefunctions at Γ of the spin-up unoccupied (UFB) and occupied (OFB) boron flat band of the 2B-575-aGNR.

Substituting the two central carbon atoms in the wider segments with boron atoms (as shown in Figure 5.1d) creates two boron-rich flat bands. These bands originate from pure boron orbitals and have no topological character, unlike the flat bands of 2B-7aGNRs[96,127]. The band structure of the 2B-575-aGNR, also shown in Figure 5.1b, reveals a significant charge transfer from its VB to the boron bands, resulting in an occupied flat band (OFB), hosting approximately 2 electrons, and an unoccupied flat band (UFB). The VB is partially depopulated and becomes metallic.

The boron flat bands and VB cross without opening a gap, as shown in Figure 5.1b, revealing a negligible mixing. This is a consequence of the different symmetries of their wavefunctions (Figure 5.1c, e). The boron flat bands, localized around the boron atoms, are symmetric with respect to the central ribbon axis, while the VB is anti-symmetric. The orthogonality between VB and boron flat bands allows electrons in the VB to propagate unperturbed along the ribbon[97], resulting in a metallic band and maintaining the boron states localized around the diboron impurities. DFT finds a magnetic moment of $0.8\mu_B$, close to spin $S = 1/2$, associated with the OFB that is localized around each 2B-unit. Spin moments in adjacent 2B-units tend to anti-align, as shown in Figure 5.1d, so the periodic system shows no net spin-polarization.

Two-Terminal Transport Measurements

Based on the intriguing properties predicted by DFT calculations, we decided to explore the on-surface synthesis and characterization of this boron-doped GNR. A retrosynthetic analysis identified the compound shown in Figure 5.2a as the ideal molecular precursor, which might lead to the formation of 2B-575-aGNRs by sequential Ullmann coupling and cyclodehydrogenation reactions on a Au(111) substrate. The molecular precursor was obtained by solution chemistry in one step from easily available starting materials (see SI[127] for details) and sublimated *in situ* on Au(111). Polymerization occurs at 250 °C, a higher temperature than for other systems[23,95], and close to the onset of cyclodehydrogenation of the polymer. The presence of the precursor's bulky methyl groups increases the energy barrier for the formation of metal organic complexes[174], which have been shown to facilitate the on-surface Ullmann coupling[175]. As a consequence, the Ullmann coupling requires a higher
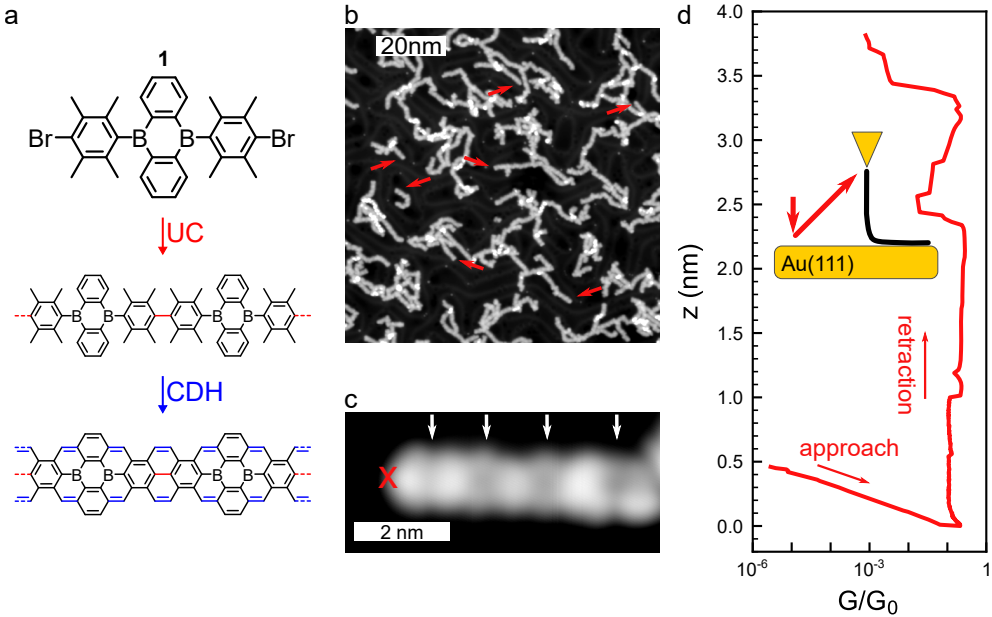
Figure 5.2: Ballistic transport through a 2B-575-aGNR: a Molecular precursor **1** and the targeted two step reaction for synthesizing 2B-575-aGNRs *via* Ullmann coupling and cyclodehydrogenation. **b** STM topography image ($V = 1\,\mathrm{V}$, $I = 30\,\mathrm{pA}$). Straight 2B-575-aGNRs are indicated by red arrows. **c** STM topography image ($V = -300\,\mathrm{mV}$, $I = 30\,\mathrm{pA}$) of a four precursor unit long 2B-575-aGNR. The positions of boron doping are indicated by white arrows. The red cross indicates the position from where the GNR is lifted for the transport experiment. **d** $G(z, V = 10\,\mathrm{mV})$ for the GNR presented in **c**. The conductance is independent of z up to $z \approx 2.2\,\mathrm{nm}$. The inset is a schematic drawing of the experimental setup.

temperature for activation. We annealed the sample to $300\,°\mathrm{C}$ to achieve a high amount of planar ribbons. The resulting structures were mostly curved and interlinked ribbons, as seen in Figure 5.2b, with a few short and straight segments (red arrows). Figure 5.2c shows an STM image of a single straight 2B-575-aGNR segment, where four boron doping sites can be identified as wider and darker segments of the ribbon.

We studied the electronic transport through a GNR suspended between the tip and sample of an STM[16,17,27,126,127,146]. To reach this two-terminal configuration, we positioned the tip above the apex of the 2B-575-aGNR (red cross in Figure 5.2c) and approached the tip towards the substrate until a sudden increase in the current indicated the formation of a bond between tip and ribbon. Then, we retracted the tip following

a leaned trajectory along the backbone of the ribbon (see Section 1.1.3). This procedure lifts the 2B-575-aGNR partially from the Au(111) and electronically decouples the free-standing segment from the metal.

Electronic transport measurements through the lifted ribbons confirm that they behave as ballistic conductors. As shown in Figure 5.2d, the linear conductance $G(z)$ of the ribbon remains constant for several nanometers while the tip is retracted. The constant conductance contrasts with the exponentially decaying conductance found for semiconducting ribbons[16,124,127,146]. In a ballistic conductor, the electron transmission $\mathcal{T}$ remains constant as a function of its length, and the conductance per channel amounts to $\mathcal{T}G_0$, where $G_0 = e^2/\pi\hbar = 77.5\,\mu S$ is the conductance quantum. In the results shown in Figure 5.2, we observe high conductance values around $\sim 0.2G_0$ remaining constant for more than $2\,nm$ of GNR elevation. The electron transmission smaller than G_0 is probably caused by the finite contact resistance between tip and GNR[176,177]. At some points we find small variations of the conductance around $0.1G$, which are consistent with atomic-scale rearrangements of the GNR-electrode contacts when additional borylated units detach from the surface[16,18]. The ballistic electron transport found here reflects the existence of scattering free transmission channels in free-standing 2B-575-aGNRs, in agreement with the boron induced metallic character revealed by our DFT calculations in Figure 5.1.

Observation of the Kondo Effect in Ballistic Ribbons

Figure 5.3a shows a $dI/dV(V, z)$ spectral map obtained by measuring dI/dV spectra during the lift of a 2B-575-aGNR (inset Figure 5.3b). A narrow zero-bias resonance (HWHM = $8.0\,mV$) appears suddenly at $z = 1.2\,nm$ and prevails up to $\Delta z \geq 3.5\,nm$ during the lifting procedure. We interpret this resonance as a manifestation of the Kondo effect in the electronic transport through the ribbon[108]. The Kondo resonance is the fingerprint of a spin state weakly coupled to an electron bath[89,116,119,126,127,178,179]. Here, it is observed for more than $2\,nm$ during the GNR elevation, hinting that the Kondo screening is not simply mediated by electrons at the surface[127]. We suggest that the metallic band of the ribbon is responsible for the screening of the localized magnetic moments.
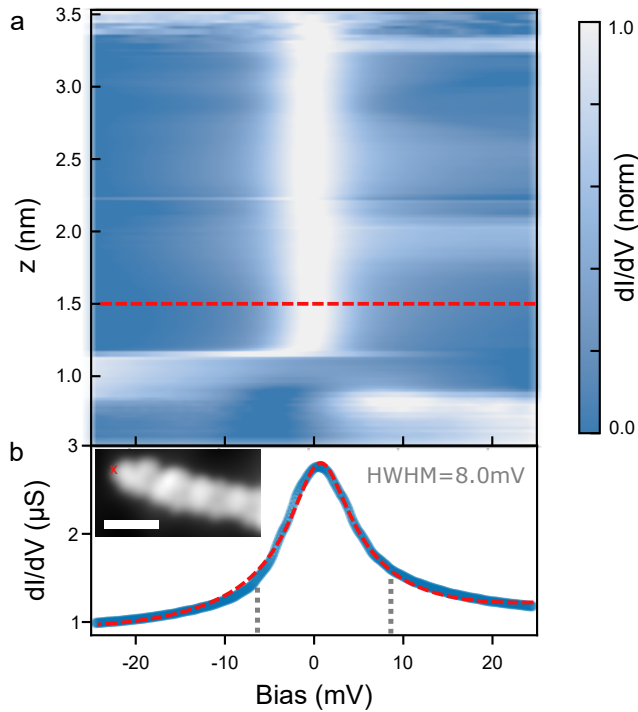
Figure 5.3: Fingerprints of magnetism in the lifted ribbon: **a** Normalized $dI/dV(V, z)$-map (see methods for details on normalization procedure). A zero-bias resonance appears in the spectra for $z > 1.2\,$nm. **b** One example dI/dV-spectrum (blue) fitted with a Frota function[115] (red dashed line). The spectrum was taken at $z = 1.5\,$nm. Inset: STM topography image ($V = -300\,$mV, $I = 30\,$pA, scale bar is $2\,$nm). The red cross indicates the position from where the GNR is lifted.

In the transport experiments presented in Figure 5.2 and 5.3 we found electronic and magnetic fingerprints that are consistent with our DFT calculations of the 2B-575-aGNR. All the 19 ribbons explored in this manner show similar results, in every case reproducing segments of constant conductance associated to ballistic transport, and Kondo resonances. However, many ribbons also showed a step-wise decrease in their conductance plots at some elongations, which we attribute to the presence of defects in their structure.

5.3 Role of Atomic Defects in the Nanoribbons

To detect the presence of atomic-scale defects in 2B-575-aGNRs, we measured constant height current images using a CO-functionalized tip[34,35]. The image of a nanoribbon composed of 4 molecular units (*i.e.* 4 boron dimers) is shown in Figure 5.4a. It is consistent with a ribbon containing a sequence of pentagonal rings in its carbon backbone at the position of Ullmann coupling (white arrows in Figure 5.4a). The extracted Lewis structure of the ribbon (referred to as 2B-575*-aGNR) is shown in Figure 5.4b. Pentagonal rings are known to appear when methyl groups of the precursor detach during the polymerization reaction[155,167,180]. This type of defect at the linking position is the most common structure we find in an analysis of 16 ribbons.

To unravel the effect of the atomic defects on the electronic transport of 2B-575-aGNRs, we performed two-terminal transport measurements on the ribbon shown in Figure 5.4 in a suspended geometry. As depicted in Figure 5.4c, the conductance $G(z)$ decreases step-wise with increasing z. The conductance steps are spaced by $\Delta z \sim 1.4\,\mathrm{nm}$, matching with the distance between two diboron sites. This suggests that they appear when a new precursor unit is inserted in the free-standing part of the ribbon[18].

Between conductance steps, constant conductance plateaus unveil that some ballistic behavior is retained. However, now, we found three qualitatively different regimes, depicted in Figure 5.4d. First, we observed a metallic like behavior, with flat $\mathrm{d}I/\mathrm{d}V \sim 0.3G_0$ signal persisting until $z = 0.6\,\mathrm{nm}$, where the first conductance steps appears. Upon further tip retraction, a zero-bias resonance similar to the one shown in Figure 5.3 appears in the spectra. Again, this indicates that a localized spin appears in the free-standing segment of the ribbon. This Kondo feature disappears at $z = 1.75\,\mathrm{nm}$, coinciding with a second step in the linear conductance plot of Figure 5.4c. Above this z value, spectra exhibit two bias-symmetric $\mathrm{d}I/\mathrm{d}V$ steps, characteristic of inelastic electron tunnelling (IET) excitations.

To follow the IET spectral evolution during the retraction, we show in Figure 5.4e a normalized $\mathrm{d}^2I/\mathrm{d}V^2(V, z)$-map. We observe that at $z = 1.75\,\mathrm{nm}$ the Kondo resonance splits gradually in $\leq 1\,\mathrm{\AA}$ and converts into
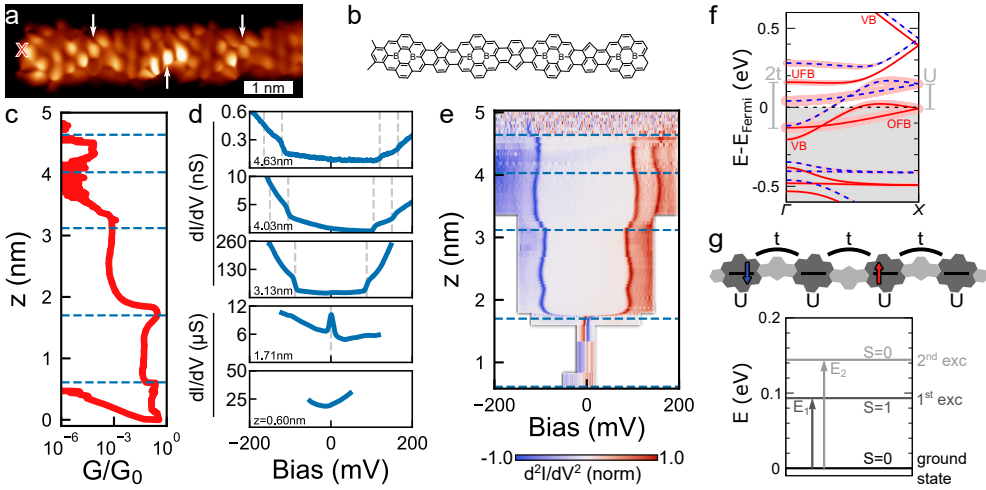
Figure 5.4: Two-terminal transport experiments in a 2B-575*-aGNR: a Bond-resolved constant height current image ($V = 5\,\mathrm{mV}$). The 2B-units alter the contrast due to buckling of the ribbon. Pentagons are indicated by white arrows. The red cross indicates the position from where the ribbon is lifted. **b** Lewis structure of the 2B-575*-aGNR in **a**. **c** Linear conductance $G(z, V = 10\,\mathrm{mV})$ obtained while lifting the ribbon presented in **a**. Some ballistic behavior is retained. **d** $\mathrm{d}I/\mathrm{d}V$-spectra at selected z. The values are indicated and correspond to the blue, dotted lines in **c** and **e**. A single Kondo-resonance at $z = 1.71\,\mathrm{nm}$ indicates the presence of a spin $S = 1/2$. For larger z inelastic excitations dominates the spectra. **e** Normalized $\mathrm{d}^2I/\mathrm{d}V^2(V, z)$-map obtained by numerical differentiation (see methods for details on normalization procedure). **f** DFT calculated band structure of periodic 2B-575*-aGNR. Notice that in this case the unit cell necessarily contains two 2B-units. Red and blue bands correspond to spin up and down. Boron character of the bands is indicated by a pink shadow. The corresponding band from the 2B-575-aGNR is indicated for the spin up band. **g** Hubbard-model used to calculate spin-excitations of the finite sized system and its energy spectrum for two electrons that are delocalized across four hopping sites. $U = 155.9\,\mathrm{meV}$, $t = 133.9\,\mathrm{meV}$, obtained from **f**.

IET steps (see Section 5.5). Above this value, the steps are observed for more than 3 nm retraction with small variations of their excitation energy. A fainter $\mathrm{d}I/\mathrm{d}V$-step, at approximately 45 mV larger bias voltage, can also be observed in the spectra above 3 nm. The continuous evolution from Kondo to IET excitations suggests that a complex spin texture exists in the 2B-575*-aGNR.

DFT calculations for periodic 2B-575*-aGNRs revealed that the presence of the pentagonal rings in the ribbon has two important implications. First, they break the structural symmetry of the GNR, mixing

the wavefunctions of boron flat bands and VB. Now, the band structure in Figure 5.4f shows avoided crossings of both UFB and OFB with the VB, characteristic of a small hybridization. Second, the removal of a carbon atom from the ribbon effectively injects another hole and lowers the occupation of both the VB and the OFB. Since the VB still crosses the Fermi level, the ribbon preserves its metallic character. DFT pictures the depopulation of the OFB as a mean delocalization of an electron over several 2B-units and a smaller net magnetic moment associated with each diboron unit ($\sim 0.5\mu_B/2B$).

To interpret the experimental IET signal, we explored different magnetic states obtained by DFT simulations of finite ribbons, like the one presented in Figure 5.4g. The DFT results indicate that the system cannot be simply treated as Heisenberg-like Hamiltonian due to the electron delocalization. In fact, DFT significantly underestimates the excitation energies as compared to the measured IET spectra and did not fully capture the relevant physical mechanisms behind the inelastic steps.

Given that the hybridization between the VB and the boron flat bands is small (notice in Figure 5.4f the 1 to 10 ratio between the size of the hybridization gaps and the VB band width), a valid approximation is treating VB and OFB as two different subsystems, disregarding excitations that imply charge-transfer between them. The observed spectral steps can then be attributed to inelastic excitations in the OFB/UFB subsystem induced by conduction electrons propagating through the VB. To describe the excitation spectrum of the boron flat bands, we use a Hubbard model with parameters t and U obtained from the DFT band structure in Figure 5.4f (see Section 5.5 for more details). This simple model can be exactly solved and approximately accounts for electron correlations in the excitation spectrum. Based on the OFB's occupation observed in DFT calculations (see Figure 5.4f), we consider the probable case of two electrons distributed over four electron sites.

Exact diagonalization of the Hubbard Hamiltonian leads to the energy spectrum presented in Figure 5.4g. The ground state is a singlet combination of the two spins. The first excited state is a triplet state located at $E_1 = 94\,\mathrm{meV}$, which matches reasonably well with the energy of the first excitation step in our experiments. Furthermore, the model also finds an excited singlet state at $E_2 = 145\,\mathrm{meV}$, in strong coincidence with the second spectral IET step. The observed agreement between the

calculated and experimentally observed excitation energies indicates the IET signals can be due to electron-hole pair excitations of a partially populated flat band, a similar excitation process to the one recently observed on small molecules on insulating layers[181]. This interpretation is supported by the fact that the excitation energies in the model are dominated by the hopping parameter between two 2B-sites t and are stable against changes of U (see Section 5.5, Figure 5.6) or electron occupation (see Section 5.5, Figure 5.7). This explains why the step values are relatively independent from the length of the free-standing segment. The model unveils a probable source of scattering phenomena in the electronic transport, which, also, can be responsible for the step-wise decrease of the linear conductance found when a new diboron unit is lifted from the surface (Figure 5.4c).

5.4   Conclusions

We have presented a graphene nanoribbon that combines a metallic transport band with localized spins inside, and described experimental fingerprints of both the metallic character and the spin-polarized states. The ribbon is fabricated by substitutionally doping the narrow-bandgap 575-aGNR with diboron units. DFT simulations unveiled that the dispersive VB becomes partially depopulated by donating electrons to flat bands formed by the diboron units. As a result, single spins emerge localized at every diboron unit, protected from the VB by their different wavefunction symmetry. Two-terminal transport experiments through free-standing GNRs placed between tip and sample of an STM demonstrated ballistic electron transport, transmitting electrons with a constant value of $0.2G_0$ for a free-standing segment length of a few nanometers. Simultaneously, the differential conductance spectroscopy in the transport configuration unraveled the spin localization by revealing a Kondo resonance that was stable during the elevation of the GNR from the surface.

In addition to the ideal case, we found that atomic defects such as pentagonal rings in the structure, frequently found in our experiments, enable a small wavefunction mixing between VB and the boron flat bands and partially depopulate both bands. The effect of these pentagonal defects in the transport is drastic, because it enables a finite interaction between adjacent diboron units and delocalizes the electrons along the

partially occupied flat band. We found that the ballistic character of the ribbon partly survives in the presence of pentagonal defects, but a new inelastic excitations appears in the spectra, accompanying a step-wise decrease of the linear conductance with ribbon elevation. Through a simple Hubbard model, parameterized with results from the DFT simulations, we found that the inelastic spectral features can be attributed to excitation of the many-body states of the partially depopulated flat band. These results thus demonstrate that the 2B-575-aGNR represent an ideal molecular system to import flat band phenomena into one-dimensional graphene nanoribbons, envisioning the study of the underlying electron transport phenomena present in these correlated systems.

5.5   Appendix

Transition from Kondo to IET-regime

The ribbon presented in Figure 5.4 undergoes a transition from the Kondo regime to an IET regime upon tip retraction starting from $z \sim 1.7\,\mathrm{nm}$. Figure 5.5 presents the transition taking place smoothly during few tens of pm.
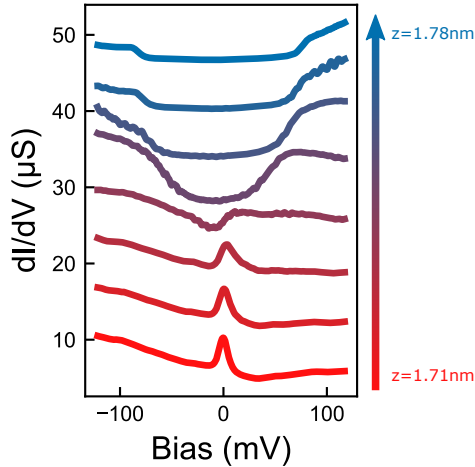

Figure 5.5: Transition from Kondo to IET regime: A Stack of differential conductance spectra taken in steps of $\Delta z = 10\,\mathrm{pm}$ shows the continuous transition from the Kondo resonance to a IET excitation. Data corresponding to Figure 5.4e. The spectra are offset by $6.6\,\mu\mathrm{S}$ for clarity.

The Four Sites Fermi-Hubbard Model

The finite-size Fermi-Hubbard model with n sites has the following Hamiltonian:

$$\hat{H} = \sum_{j=1}^{n-1} \sum_{\sigma=\downarrow}^{\uparrow} t \left(\hat{c}_{j+1,\sigma}^{\dagger} \, \hat{c}_{j,\sigma} + \hat{c}_{j,\sigma}^{\dagger} \, \hat{c}_{j+1,\sigma} \right) + \sum_{j=1}^{n} U \, \hat{n}_{j,\uparrow} \, \hat{n}_{j,\downarrow}$$

where each $\hat{c}_{j,\sigma}^{\dagger}$ ($\hat{c}_{j,\sigma}$) is the fermionic creation (annihilation) operator of site j and spin σ, $\hat{n}_{j,\sigma} = \hat{c}_{j,\sigma}^{\dagger} \, \hat{c}_{j,\sigma}$, U is the Hubbard on-site repulsion between two electrons and t is related to the kinetic energy of an electron hopping from one site to an adjacent site. A schematic illustration of the structure is shown in Figure 5.4g. Approximate values of the two parameters were obtained from the band structure shown in Figure5.4f. The energy spectrum and eigenstates of the system were obtained through exact diagonalization.

To analyze the stability of the Fermi-Hubbard model with respect to changes of U, we have considered U values ranging from 0 to $2t$. The results are presented in Figure 5.6. Within this energy range, no qualitative change of behaviour is observed. The energy difference between the ground state and the two excited states remains in the order of t, indicating that this is the relevant energy scale for the experimentally observed excitations. Furthermore, the energy scale of the first excited states of the model is robust against changes in the number of electrons. Excitation energies were calculated for one, two and three electrons in the model (Figure 5.7). We find that the excitation energies match reasonably well with the experimental data in all cases.
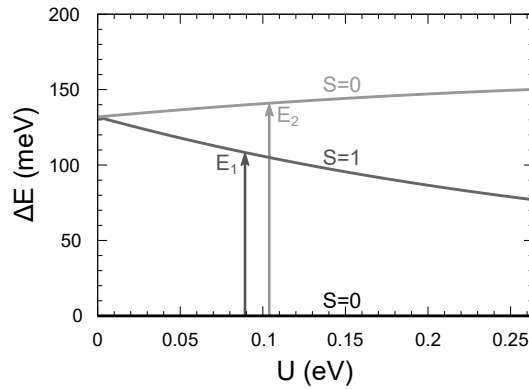
Figure 5.6: Hubbard energy spectrum for different U: Excitation energy ΔE obtained from the energy spectrum of the Fermi-Hubbard model as a function of U in the two electron model with $t = 133.9\,\text{meV}$.
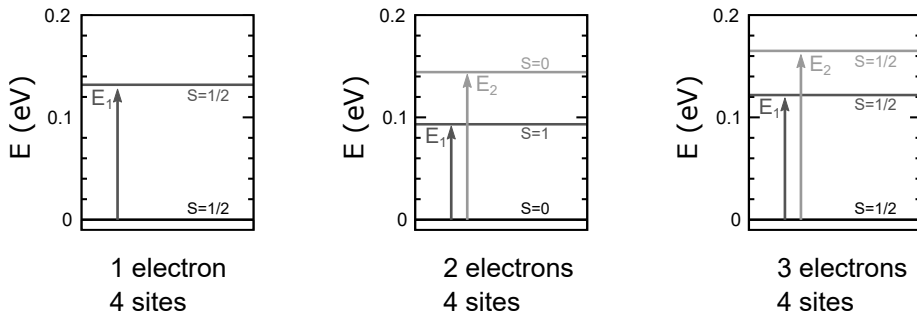
Figure 5.7: Comparison between Hubbard models containing different numbers of electrons: Excitation spectrum obtained from the four-site model Hamiltonian with one, two and three electrons (left to right) for $U = 155.9\,\text{meV}$ and $t = 131.9\,\text{meV}$. For an odd number of electrons, there are only doublet-doublet excitations in this energy range. For an even number of electrons, there are both singlet-triplet and singlet-singlet excitations. Note that the excitation energy increases when going from two to three electrons.

6 Electrically Addressing the Spin of a Magnetic Porphyrin through Covalently Connected Graphene Electrodes

We report on the fabrication and transport characterization of atomically precise single molecule devices consisting of a magnetic porphyrin covalently wired by graphene nanoribbon electrodes. The tip of a scanning tunneling microscope was utilized to contact the end of a GNR-porphyrin-GNR hybrid system and create a molecular bridge between tip and sample for transport measurements. Electrons tunneling through the suspended molecular heterostructure excited the spin multiplet of the magnetic porphyrin. The detachment of certain spin-centers from the surface shifted their spin-carrying orbitals away from an on-surface mixed-valence configuration, recovering its original spin state. The existence of spin-polarized resonances in the free-standing systems and their electrical addressability is the fundamental step for utilization of carbon-based materials as functional molecular spintronics systems.

The following Chapter is published as a letter in the journal **Nano Letters**. Adapted with permission from *Nano Lett.* 2019, 19, 5, 3288–3294. Copyright 2019 American Chemical Society.

- *Electrically Addressing the Spin of a Magnetic Porphyrin through Covalently Connected Graphene Electrodes*

  Jingcheng Li, **Niklas Friedrich**, Nestor Merino, Dimas G. de Oteyza, Diego Peña, David Jacob and Jose Ignacio Pascual

  Nano Lett. 19, **5**, 3288-3294, Published 9 April 2019

  `https://doi.org/10.1021/acs.nanolett.9b00883`

6.1   Introduction

Single molecule spintronics envisions utilizing electronic spins of single molecules for performing active logical operations. The realization of such fundamental quantum device relies on the accessibility of electronic currents to the active molecular element, and on the existence of efficient electron-spin interaction enabling writing and reading information. Single molecule (SM) electrical addressability has been achieved in break junctions experiments[182–184], which generally find that the ultimate SM functionality is dominated by the nature of its contacts to source-drain electrodes[185]. To ensure stable and reproducible behaviour of the SM device, robust and atomically precise molecule electrode contacts with optimal electronic transmission are required[186,187]. Aromatic carbon systems such as nanotubes, and graphene flakes are considered ideal electrode materials[188,189] because of their structural stability and flexibility, and the large electronic mobility they exhibit. Graphene electrodes also offer the perspective of covalently bonding to a single molecule at specifically designed sites[190], thus creating robust systems for electrical measurements.

While methods to fabricate graphene-SM systems are being developed[92,151], the spin addressability by electronic currents through them remains to be demonstrated. Attractive predictions on the role of graphene-SM hybrids as spin valves, diodes, or rectifiers[13,191] are proposed to strongly depend on the coupling of electronic currents with spin-polarized molecular states and, hence, on the precise contact geometry. Furthermore, spins are sensitive to electronic screening[192] and to electrostatic and magnetic fields[193] in its local environment. Therefore, precise strategies for spin detection and manipulation in atomically controlled hybrid structures are needed[89] to determine the magnetic functionality of the hybrids and the possible operation mechanisms.

In this work, we electrically address the spin of an iron porphyrin molecule covalently wired to graphene nanoribbon electrodes. To perform two-terminal transport measurements with atomic-scale control on the GNR-SM connections, we fabricated a linear GNR-SM-GNR hybrid system utilizing on-surface synthesis[22,194,195]. In OSS, pre-designed organic precursors on a flat metal surface are thermally activated to react along specific polymerization pathways, steering the formation of a targeted molecular extended systems with atomic-scale precision. The

obtained linear hybrids were characterized by high-resolution STM images and compared with results of two-terminal transport measurements of free standing systems bridging the tip and sample electrodes. We demonstrate that the iron spin can be addressed by electronic currents injected into the free standing ribbons. From the transport results, we unveil an intriguing dependence of the spin excitation's spectral fingerprint on the connecting patterns between GNR and SM. For some contact structure, the molecular species lie in a mix-valence state on the surface, which vanishes as soon as they are brought into a free-standing configuration. Controlling the alignment of spin-polarized states thus permit operating on the transport mechanisms through such magnetic systems.

6.2 Fabrication and Study of GNR-Porphyrin Systems

The linear GNR-porphyrin-GNR hybrid systems were created by mixing the two molecular precursors shown in Fig. 6.1a and thermally activating a step wise reaction on a Au(111) surface. The 2,2'-dibromo-9,9'-bianthracene (DBBA) molecule produces narrow (3,1)-chiral GNRs (chGNRs)[196], which are semiconductors with a band gap of 0.7 eV on the Au(111) surface[100]. As magnetic species we chose the $Br_2FeTPP(Cl)$ molecule with trans-halogenated configuration to produce linear connections to the chGNRs through a surface-mediated Ullmann-like reaction. Both molecules were co-deposited onto an atomically clean Au(111) substrate kept at 200 °C to induce dehalogenation and co-polymerization of the mixture. Subsequently, the substrate was annealed to 250 °C to induce the cyclodehydrogenation step that forms the planar ribbon structure and, additionally, fuses the tetraphenyl substituents with the porphine pyrroles (Figure 6.1b) into a fully planar structure[92,197] with atomically precise and robust connections.

The overview STM image in Figure 6.1c confirms that the on-surface reaction proceeds as depicted in Figure 6.1b, and most FeTPP centers (arrows in Figure 6.1c) appear connected to two chGNRs in a trans-configuration. However, not all fabricated structures appear as straight systems, but in many the terminal chGNRs appear bent with varying angles between them. As we explain in the Figure S1 of the SI in[146], the
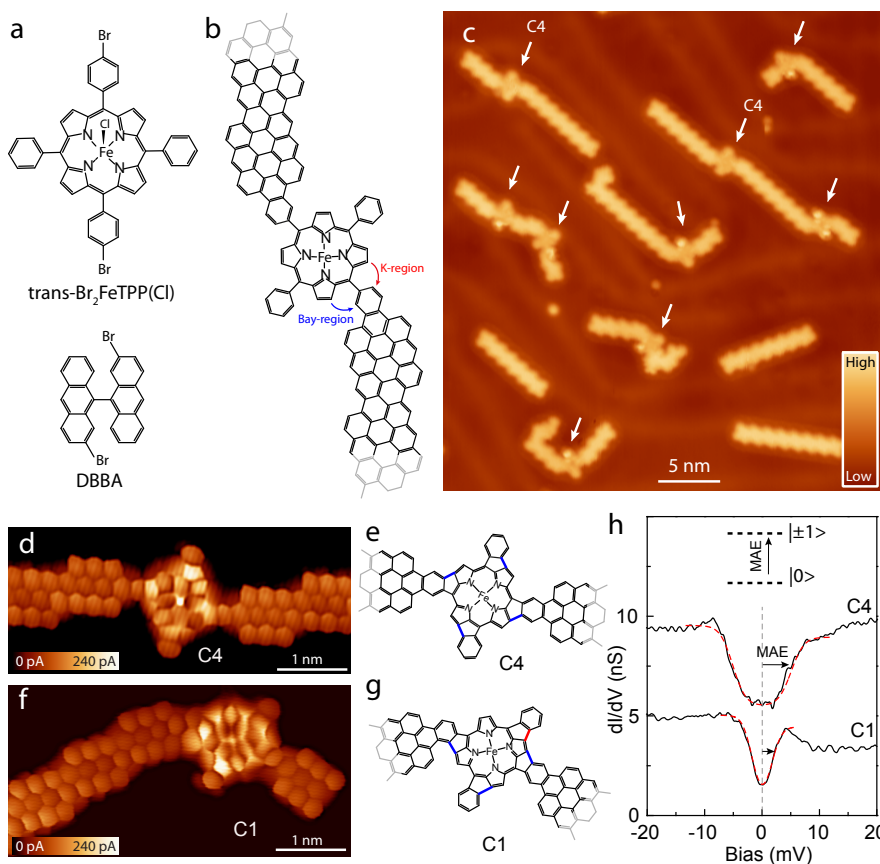
Figure 6.1: Synthetic strategy and characterization of magnetic FeTPP contacted by two GNR electrodes in a linear manner: a Structures of trans-Br_2FeTPP(Cl) (up) and DBBA (down) as the molecular building blocks. **b** Structure of a molecular devices after the polymerization and CDH of the two molecular building blocks in **a**. The CDH can additionally fuse the porphyrin core in a clockwise (K-region, red arrow) or anticlockwise (Bay-region, blue arrow) manner to the contact phenyl. **c** STM overview image shows several molecular devices created on a Au(111) surface. The arrows indicate the porphyrins fused to GNR electrodes. **d,f** Constant height current images measured with a CO-functionalized tip ($V = 2\,\mathrm{mV}$) of a linear and a bent hybrid structure with a $C4$- and $C1$-FeTPP cores, respectively, as shown in the models **e,g**, respectively. **h** Differential conductance spectra over the Fe center of each species, showing inelastic spin excitation steps at the magnetic anisotropy energy (MAE) of the Fe magnetic moment. The inset shows the expected spin excitation for the pristine $S = 1$ FeTPP molecule. Red dashed lines show the fitting to the spectra using the model from[147].

different angles appear due to a combination of two structural characteristics: the existence of two different chiral GNR enantiomers on the surface[100] and of two bonding configurations of the contacted phenyl with the core pyrroles, either through a K-region or through a Bay-region, as depicted by red and blue arrows in Figure 6.1a[92,197], respectively. Straight systems such as the ones labelled $C4$ in Figure 6.1c, combine two chGNRs with the same enantiomeric form, both contacting the pyrrole corolla through CDH in the K-region (red arrow in Figure 6.1b). Bent structures are obtained when different chGNR enantiomers and/or different contact directions (K or Bay) are mixed.

To precisely determine the chGNR-FeTPP bonding configuration in every case, we measured high-resolution current images using CO functionalized tips[34,35,198] (Figure 6.1d, f). Most of the straight species appear with all their phenyl rings rotated in the same direction (*i.e.* $C4$-symmetric, resulting in characteristic four-fold intra-FeTPP patterns (Figure 6.1e). Bent structures frequently show one phenyl ring fused in the opposite direction than the others (*i.e.* $C1$-symmetric, Figure 6.1g). The precise symmetry of the FeTPP core determines the magnetic properties of the Fe center on the Au(111) surface[92]. Differential conductance (dI/dV) spectra measured over the FeTPP core (Figure 6.1h) show two symmetric steps around zero bias due to inelastic excitation of the FeTPP spin 1 multiplet. As reported previously[199], the ground state of the FeTPP species on the gold surface maintains the easy-plane magnetic anisotropy ($S_z = 0$) of the free molecule, and the dI/dV steps mark the onset of inelastic electron excitation into an out-of-plane spin configuration ($S_z = \pm 1$). On the straight $C4$ species, the steps appear around $\pm 5.0\,\mathrm{mV}$, corresponding to a magnetic anisotropy energy (MAE) of $5.0\,\mathrm{meV}$. On the bent $C1$ species, the MAE is smaller (around $1.0\,\mathrm{meV}$), and frequently accompanied by pronounced spectral asymmetries[92].

6.3   Spin Excitations in Two-Terminal Electronic Transport Measurements

We measured the electronic transport through these hybrid GNR-FeTPP-GNR systems by forming junctions as sketched in Figure 6.2a. These
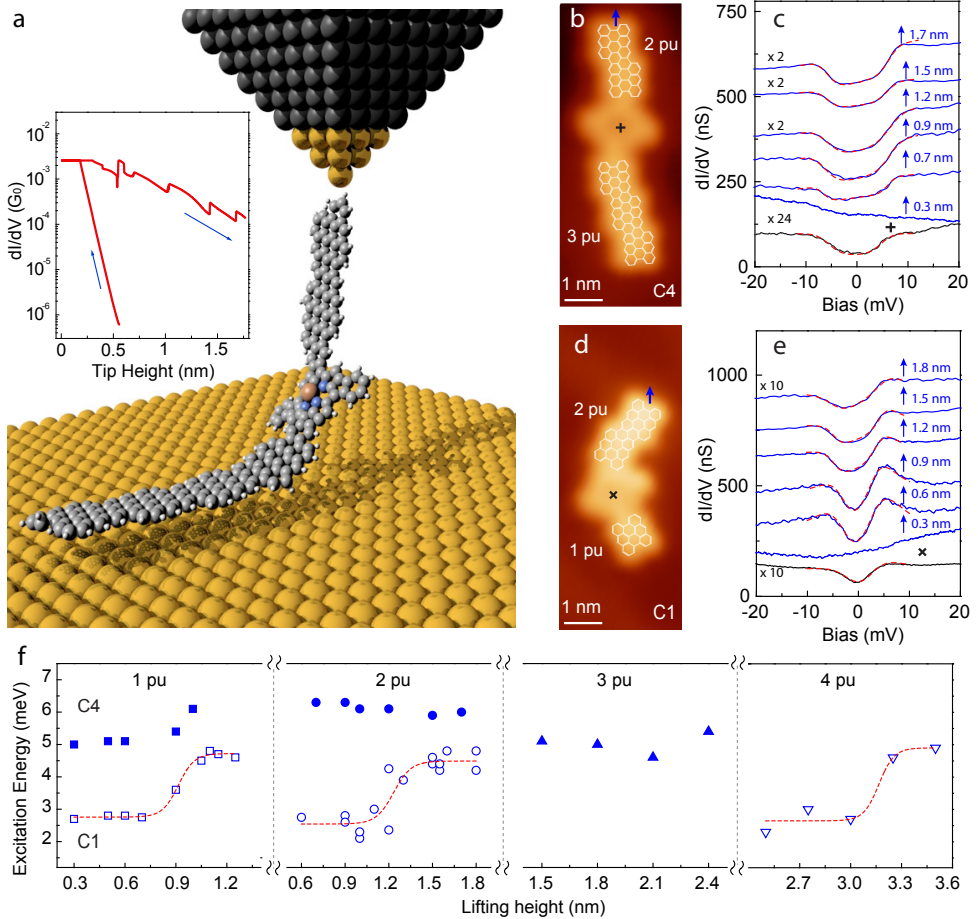
Figure 6.2: Transport measurements on FeTPP-GNR systems a Illustration of the aimed experimental geometry. Inset shows a typical conductance-distance plot simultaneously recorded during tip approach and retraction. **b,d** Constant current STM images of $C4$- and $C1$-FeTPP-GNR systems ($V = 0.5\,\mathrm{V}$, precursor units (pu) overlays the figure). **c, e** $\mathrm{d}I/\mathrm{d}V$ spectra at different lifting heights (labels) for the two molecular junctions (spectra vertically shifted for clarity, blue arrows in **b,d** indicate the contacting points). The bottom spectra (in black) were measured over the Fe centers, prior to the retraction. Red dashed lines simulate the spectra using the model from[147], from which spin excitation energies were obtained. **f** Spin excitation energies of the $C4$- (filled) and $C1$- (open) FeTPP-GNR systems as a function of lifting heights. The four panels show data from three contacting experiments of each kind, with different GNR lengths (precursor units annotated in the figure). Data points of $C1$-FeTPP with 1 pu and 2 pu are from several different lifting experiments of the same hybrid system. Red dashed lines are guides to highlight the increase in excitation energy for $C1$-FeTPP systems.

were created by approaching the STM tip to contact the termination of a chGNR (e.g. blue arrow in Figure 6.2b, d), and then retracting to lift up the ribbon from the metal substrate[17]. This procedure successfully elevated the systems to several nanometers[200]. To investigate the effect of electronic currents through the ribbon on the spin states of the FeTPP, we acquired dI/dV spectra during the lifting processes.

Figure 6.2 shows the evolution of dI/dV plots with tip retraction height for both the straight, $C4$-symmetric (Figure 6.2b, c) and the bent, $C1$-symmetric (Figure 6.2d, e) GNR-FeTPP-GNR systems. For the $C4$-symmetric case in Figure 6.2c, the initial featureless spectrum of the contacted GNR termination remains until a lifting height of about 0.7 nm. From this point on, step features emerge in the spectra, resembling the inelastic steps measured over the FeTPP core (black curve in Figure 6.2c), and remain with this shape during all the retraction expedition. For comparison, similar dI/dV spectra measured on a bare chGNR are featureless regardless of the lifting heights (see Figure S2 in[146]). Hence, we attribute these features to the inelastic excitation of the FeTPP spin multiplet by inelastic electrons tunneling through the chGNR contacts. We note that the narrow (3,1) chGNRs are semiconducting[100]. As soon as direct tunneling between tip and sample becomes weak, co-tunneling through the 0.7 eV chGNR band gap dominates the electrical transport and can reach the FeTPP core, exciting its spin multiplet.

Similar measurements on the bent $C1$ species also show step-like spectral features for lifting heights larger than ~ 0.6 nm (Figure 6.2d, e). However, in this case the step-like features become wider than the reference spectrum (black curve in Figure 6.2e), and develop an asymmetric component for several retraction values. To quantify this effect, we fitted the spectra around zero bias using a scattering phenomenological model[147], assuming the characteristic spin 1 with easy plane magnetic anisotropy of FeTPP[199]. Figure 6.2f summarizes the MAE values extracted from fits to spectra at different lifting heights, for both $C1$-FeTPP and $C4$-FeTPP lifted by GNRs of varying lengths (quantified by the number of precursor units (pu)). Focusing on the system presented in Figure 6.2d with 2 pu, the MAE (empty symbols) shows a step-wise increase from the original ~ 2.5 meV to ~ 4 meV at a retraction height of ~ 1.2 nm, and remains constant around this value henceforth. A similar step-wise increase of the MAE was found in lifting experiments of other

$C1$-FeTPP systems with different ribbon lengths' (*e.g.* 1 pu, and 4 pu in Figure 6.2f). They appear at lift heights scaling with the length of the ribbons (*e.g.* 3 nm for ribbons consisting of four precursor units), indicating that they are caused by the upraise of the FeTPP core from the metal surface, to bridge the tip and sample (Figure 6.2g). In contrast, the MAE of $C4$-FeTPP systems remains constant throughout the whole lifting process, thus not being affected by the FeTPP detachment. These results indicate a hidden mechanism controlling the MAE for the case of the asymmetric $C1$-FeTPP cores.

To shed light on the origin of the different MAE evolution with elevation of the $C4$- and $C1$-FeTPP species, we investigated the effect of lifting on the spin carrying orbitals by recording the dI/dV spectra over wider bias range. The magnetic moments of transition metal porphyrins are distributed in a set of d orbitals, split according to the ligand field around the Fe ion. For pristine FeTPP, two spin-polarized frontier orbitals around E_F account for the $S = 1$ magnetic ground state on a Au(111) surface[199,201,202]. Figure 6.3a compares dI/dV spectra of pristine FeTPP (chGNR contacted) molecules with that of $C4$- and $C1$-FeTPP hybrids on the bare surface. The spectrum on $C4$-FeTPP reproduces the frontier states of pristine FeTPP, but with the state at positive bias (attributed to the singly unoccupied (SU) state[199]) shifted towards the Fermi level (E_F). On the $C1$-FeTPP system, the SU resonance is shifted further to overlap with E_F. Wide-range spectra measured while lifting the FeTPP-GNR hybrids show that the SU state of the $C4$-FeTTP remains around similar values during the whole tip retraction process (Figure 6.3b). In contrast, the resonance centred at E_F in the $C1$-FeTPP species shifts away from the Fermi level with the lifting height, until a value of around 100 mV is reached (Figure 6.3c). Interestingly, the MAE values extracted in Figure 6.2f show a linear dependence with the energy values of SU peaks (Figure 6.3d), suggesting that both effects are related.

Theoretical Modelling of MAE Renormalization

The shift of a molecular state away from the Fermi level as the ribbon is lifted up indicates a change in the filling of the spin-carrying d orbitals of the $C1$-FeTPP core. Thus, a plausible explanation for the observed dependence of excitation energy on resonance alignment is the renormal-
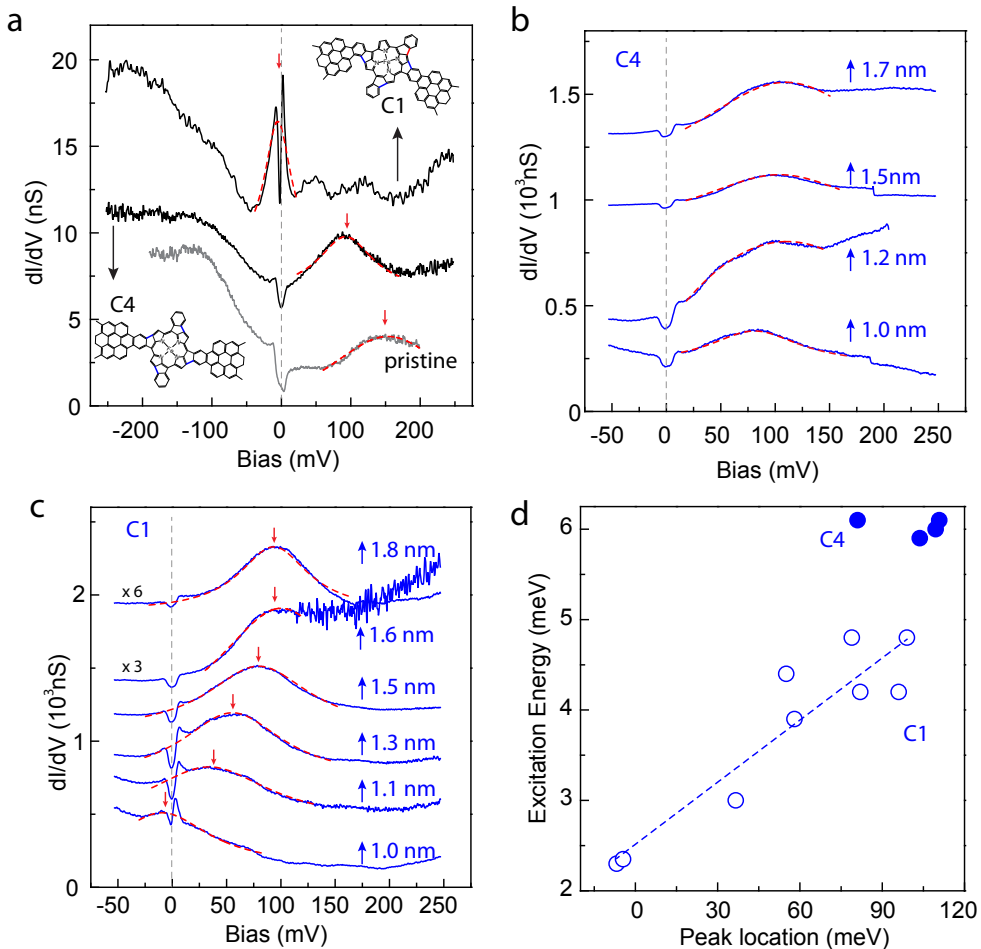
Figure 6.3: Effect of d orbital filling on the MAE of FeTPP. **a** dI/dV spectra recorded on a pristine FeTPP (saddle shaped, contacted to chGNRs), planar $C4$- and $C1$-FeTPP species on the bare surface. **b,c** dI/dV spectra recorded at different lifting heights of $C4$- and $C1$-FeTPP respectively. The lifted hybrid systems are the same as the ones in Figure 6.2c, e. The spectra in **a-c** are shifted for clarity, and the red dashed lines show the Lorentz fitting to the resonances of different types of FeTPP. Red arrows indicate the center of the peaks. **d** Excitation energy (*i.e.* MAE) extracted from the inelastic features using the model from[147] as the function of energy location of resonances in **b,c**.
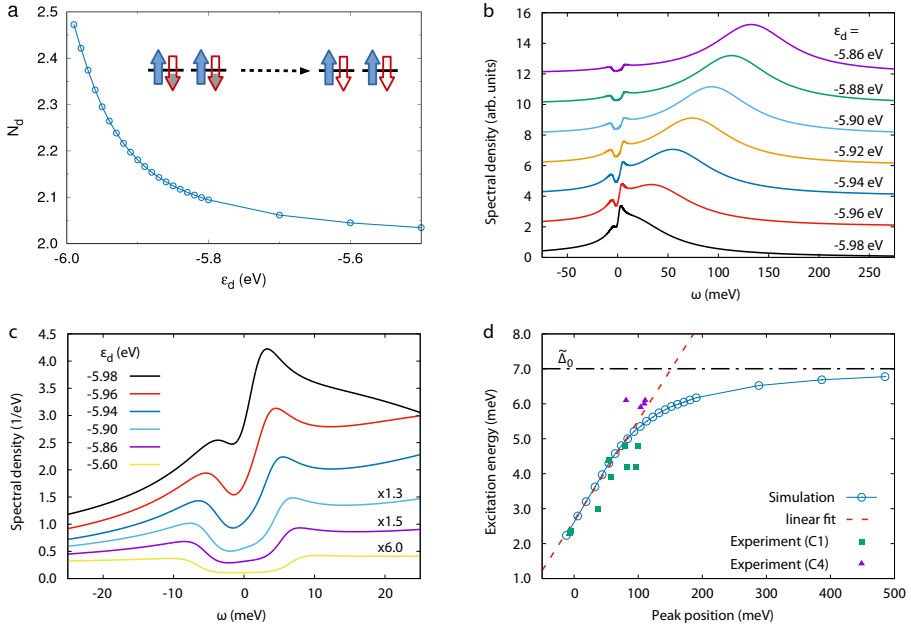
Figure 6.4: **Two-orbital Anderson model simulations a** Impurity occupancy N_d as a function of the on-site energy ε_d. **b,c** Spectral functions for different on-site impurity energies ε_d show the upper Coulomb peak shifting (**b**) and in a smaller energy window around E_F, the resulting inelastic step features (**c**). **d** Excitation energy as a function of the Coulomb peak position. The experimental data from Figure 6.3d are also included here for comparison. All simulations were done with uni-axial magnetic anisotropy $D = 7.14\,\text{meV}$, single-particle broadening $\Gamma = 30\,\text{meV}$, intra- and inter-orbital Coulomb repulsion $U = 3.5\,\text{eV}$ and $U' = 2.5\,\text{eV}$, respectively, and Hund's rule coupling $J_H = 0.5\,\text{eV}$.

ization of the MAE by charge fluctuations[203]. In order to verify this scenario we modelled the spin excitations of the $S = 1$ system coupled to the surface by solving a two-orbital Anderson impurity model (2AIM) close to half-filling, including a uni-axial magnetic anisotropy term[203] in the one-crossing approximation (OCA)[204]. Changes in orbital filling can be simulated by shifting the impurity levels ε_d downwards, resulting in the increase of electron occupation N_d of the d orbitals (Figure 6.4a). The model spectra (Figure 6.4b) show a pronounced peak at positive energies that moves towards E_F as the impurity levels are lowered in energy and their filling increases. This peak is the upper Coulomb peak

in the Anderson model, corresponding to the SU state of our spectra. For $\varepsilon_d \sim -6\,\text{eV}$ the resonance lies directly over E_F and the system enters the mixed-valence regime ($N_d \sim 2.5$). This state is characterized by strong charge fluctuations that lead to a strong renormalization of the bare MAE (Δ_0). The resulting spin excitation features around zero (black line in Figure 6.4c) are fainter and narrower, and with asymmetric components, similar to the experimental plots on $C1$-FeTTP species on the surface (*cf.* Figure 6.2e).

The lift-up process gates the SU resonance of the $C1$-FeTPP core away from E_F, driving the system towards half-filling ($N_d \sim 2$), and thus reducing the charge fluctuations. This leads to an increase in the MAE, as the renormalization by charge fluctuations is reduced, and more symmetric inelastic steps. The variation of spectral features with the alignment of the impurity level shown in Figure 6.4c reproduces the evolution of spin excitation spectra of $C1$-FeTPP species with the lift height observed in the experiments (*cf.* Figure 6.2e).

The 2AIM also reproduces the correlation between MAE and orbital alignment found in the experiments (Figure 6.4d). The MAE shows a linear behavior for peak positions up to $100\,\text{meV}$, while for larger values the MAE develops a sublinear behavior, approaching the upper limit given by $\tilde{\Delta}_0$ at the particle-hole symmetric point ($\varepsilon_d = -4\,\text{eV}$). At this point, charge fluctuations are fully suppressed ($N_d = 2$). Still, the value $\tilde{\Delta}_0$ is slightly smaller than the bare MAE of $\Delta_0 = D = 7.14\,\text{meV}$ due to renormalization by Kondo exchange coupling with the conduction electrons[192,203].

The excellent agreement between calculations and experimental results suggests that changes in the filling of the d orbitals are responsible for the variations of MAE in planar FeTPP cores embedded in chGNRs[92]. The fairly constant MAE value of the $C4$-FeTPP species at all lift heights is explained by the small variation of their d orbitals during retraction and, consequently, in the degree of charge fluctuations. However, the MAE of lifted $C1$-FeTPP systems can still be smaller than in $C4$-FeTPP species with similar orbital alignment (*cf.* Figure 6.2f). The lower axial symmetry of the asymmetrically fused species, which causes a larger degree of orbital mixing, is a probable additional mechanism accounting for a lower intrinsic MAE of $C1$-FeTPP systems[205,206].

6.4 Conclusions

The survival of the molecular spin in the free-standing graphene systems, together with the presence of spin-polarized orbitals around the Fermi level, are key ingredients for realizing an organic spin-filter device[207]. We envision that, combined with spin-polarized currents (*e.g.* from magnetic metal electrodes) and magnetic fields, many of the predicted functionalities of these model platforms as molecular spintronics elements could be experimentally tested, benefiting from the high degree of reliability of its covalent construction.

7 Conclusion

In this Thesis, I presented spectroscopic two-terminal transport experiments through three different types of spin-hosting graphene nanoribbons in a low-temperature scanning tunneling microscope. I mechanically lifted individual ribbons partially from a Au(111) substrate using the tip of the scanning tunneling microscope such that the free-standing segment of the nanoribbon bridges tip and substrate, creating the transport configuration. The free-standing segment does not hybridize with the substrate and thus, allows probing the pristine properties of the suspended GNR. The ribbons were fabricated *in situ* with atomically precise on-surface synthesis strategies under ultra-high vacuum conditions and their atomic structures were confirmed *via* bond resolved scanning tunneling microscopy.

This work demonstrates the access to spin-polarized states in graphene nanoribbons in coherent electron transport through the ribbons. The spin polarization of the states was confirmed experimentally in spectroscopic measurements of the differential conductance by either Kondo resonances or inelastic step excitations in the $S = 1/2$ and $S = 1$ systems, respectively.

In a dilute-diboron-doped seven armchair graphene nanoribbon a localized state emerges around dopant sites. Lifting the nanoribbon, this localized state creates a quantum-dot like double barrier configuration for electrons tunneling from tip to substrate. We have demonstrated that resonant transport through this state occurs in a bipolar fashion, with the occupied diboron state enabling resonant transport for either bias voltage polarity. Furthermore, we observe vibronic satellite peaks and quantized band states in transport experiments.

A Kondo resonance emerges in the two-terminal transport experiments through a 7aGNR with a single substitutional diboron dopant,

when the diboron unit is positioned in close proximity to the Au(111) substrate, suggesting a spin polarization of the 2B-state. Our combined *ab inito* and mean-field Hubbard simulations show that the removal of two p_z electrons at the diboron moiety together with the stabilization of two Clar sextets around it ruptures the continuous conjugation of the valence band electrons. Consequently, two topologically protected edge states form inside the ribbon on either side of the 2B-unit. We found that the finite Coulomb exchange between the states leads to ferromagnetic coupling resulting in an $S = 1$ triplet ground state.

Surprisingly, we also observed a similar Kondo resonance emerging in ribbons with dense 2B doping, where no topological state is expected. By a combination of density functional theory and mean-field Hubbard simulations we rationalized the origin of this spin polarization. The metallic substrate mediates hopping processes through the 2B-units that enable the valence band electrons to propagate freely in the ribbon. This leads to an apparent recovery of the topological VB in the on-surface segment of the ribbon and the spin-polarized topological-like end state emerges close to the substrate in the non-free-standing segment of the ribbon.

Density function theory found that a modification of the edge structure of the dense boron-doped GNR, namely the removal of eight carbon atoms per unit cell, creates a ribbon that unifies a spin-polarized flat band close to the Fermi level and a dispersing band, crossing E_{Fermi}, thus endowing the system with a metallic character. The different wave function symmetries of flat and dispersive bands enable the coexistence of spin polarization in the former and metallic character due to the latter. In transport experiments through this ribbon, we found ballistic transport with high conductance values reaching $\sim 0.2 G_0$ combined with a stable Kondo resonance over retraction lengths of several nanometers. This confirmed the theoretical predictions of the 2B-575-aGNRs behaving as a metallic and spin hosting ribbon. We also found that defects frequently found in the atomic structure of the ribbon enable a perturbative interaction between transport and flat band resulting in electron-hole pair excitations between different spin states that we modelled using an underfilled Hubbard model.

Finally, we also studied two-terminal transport though hybrid GNRs formed by an iron prophyrine contacted with two chiral GNRs. We have demonstrated the electrical access to a *d*-shell spin in a hybrid device by

charge injection through the connecting chiral graphene nanoribbons. We found that the magnetic anisotropy energy of the *d*-shell spin obtained from inelastic tunneling spectroscopy is identical for direct tunneling injection from the STM tip and for injection *via* the nanoribbon. For specific porphyrin molecules, the magnetic anisotropy energy increases upon lifting the molecule. Modelling the system with a two orbital Anderson impurity model, we explain this effect as a renormalization of the magnetic anisotropy energy on the surface induced by charge fluctuations in the spin-hosting *d* orbital. Thus, fluctuations disappeared when the Fe ion was in the suspended part of the hybrid.

The results presented here provide a more profound understanding of the origin, mechanisms and detection schemes of spin-polarized states in graphene nanoribbons. The electronic access to these states in a transport configuration demonstrated in this Thesis answers first fundamental questions regarding emergence, persistence and excitation of spins by electron transport currents, paving the way towards the implementation of graphene nanoribbons in single-molecule spintronics. Our results benefited by the fact that the free-standing segments of the GNRs do not hybridize with the substrate, allowing us to study the rich physics of the unperturbed molecule.

Bibliography

[1] NobelPrize.org. "The Nobel prize in physics 1986." (2022), [Online]. Available: https://www.nobelprize.org/prizes/physics/1986/summary/.

[2] A. Aviram and M. A. Ratner, "Molecular rectifiers," *Chem. Phys. Lett.*, vol. 29, no. 2, pp. 277–283, 1974. DOI: 10.1016/0009-2614(74)85031-1.

[3] J. W. G. Wildöer, L. C. Venema, A. G. Rinzler, R. E. Smalley, and C. Dekker, "Electronic structure of atomically resolved carbon nanotubes," *Nature*, vol. 391, no. 6662, pp. 59–62, 1998. DOI: 10.1038/34139.

[4] T. W. Odom, J.-L. Huang, P. Kim, and C. M. Lieber, "Atomic structure and electronic properties of single-walled carbon nanotubes," *Nature*, vol. 391, no. 6662, pp. 62–64, 1998. DOI: 10.1038/34145.

[5] S. J. Tans, A. R. M. Verschueren, and C. Dekker, "Room-temperature transistor based on a single carbon nanotube," *Nature*, vol. 393, no. 6680, pp. 49–52, 1998. DOI: 10.1038/29954.

[6] H. Park *et al.*, "Nanomechanical oscillations in a single-C_{60} transistor," *Nature*, vol. 407, no. 6800, pp. 57–60, 2000. DOI: 10.1038/35024031.

[7] W. Liang *et al.*, "Fabry - Perot interference in a nanotube electron waveguide," *Nature*, vol. 411, no. 6838, pp. 665–669, 2001. DOI: 10.1038/35079517.

[8] K. Besteman, J.-O. Lee, F. G. M. Wiertz, H. A. Heering, and C. Dekker, "Enzyme-coated carbon nanotubes as single-molecule biosensors," *Nano Lett.*, vol. 3, no. 6, pp. 727–730, 2003. DOI: 10.1021/nl034139u.

[9] M. Elbing *et al.*, "A single-molecule diode," *PNAS*, vol. 102, no. 25, pp. 8815–8820, 2005. DOI: 10.1073/pnas.0408888102.

[10] H. L. Tierney *et al.*, "Experimental demonstration of a single-molecule electric motor," *Nat. Nanotechnol.*, vol. 6, no. 10, pp. 625–629, 2011. DOI: `10.1038/nnano.2011.142`.

[11] K. Tsukagoshi, B. W. Alphenaar, and H. Ago, "Coherent transport of electron spin in a ferromagnetically contacted carbon nanotube," *Nature*, vol. 401, no. 6753, pp. 572–574, 1999. DOI: `10.1038/44108`.

[12] A. R. Rocha *et al.*, "Towards molecular spintronics," *Nat. Mater.*, vol. 4, no. 4, pp. 335–339, 2005. DOI: `10.1038/nmat1349`.

[13] J. S. Miller, D. Gatteschi, and S. Sanvito, "Molecular spintronics," *Chem. Soc. Rev.*, vol. 40, no. 6, pp. 3336–3355, 2011. DOI: `10.1039/C1CS15047B`.

[14] L. Guo, X. Gu, X. Zhu, and X. Sun, "Recent advances in molecular spintronics: multifunctional spintronic devices," *Adv. Mater.*, vol. 31, no. 45, p. 1 805 355, 2019. DOI: `10.1002/adma.201805355`.

[15] R. Temirov, A. Lassise, F. B. Anders, and F. S. Tautz, "Kondo effect by controlled cleavage of a single-molecule contact," *Nanotechnology*, vol. 19, no. 6, p. 065 401, 2008. DOI: `10.1088/0957-4484/19/6/065401`.

[16] L. Lafferentz *et al.*, "Conductance of a single conjugated polymer as a continuous function of its length," *Science*, vol. 323, no. 5918, pp. 1193–1197, 2009. DOI: `10.1126/science.1168255`.

[17] M. Koch, F. Ample, C. Joachim, and L. Grill, "Voltage-dependent conductance of a single graphene nanoribbon," *Nat. Nanotechnol.*, vol. 7, no. 11, pp. 713–717, 2012. DOI: `10.1038/nnano.2012.169`.

[18] G. Reecht *et al.*, "Electroluminescence of a polythiophene molecular wire suspended between a metallic surface and the tip of a scanning tunneling microscope," *Phys. Rev. Lett.*, vol. 112, no. 4, p. 047 403, 2014. DOI: `10.1103/PhysRevLett.112.047403`.

[19] K. Nakada, M. Fujita, G. Dresselhaus, and M. S. Dresselhaus, "Edge state in graphene ribbons: nanometer size effect and edge shape dependence," *Phys. Rev. B*, vol. 54, pp. 17 954–17 961, 1996. DOI: `10.1103/PhysRevB.54.17954`.

[20] T. Cao, F. Zhao, and S. G. Louie, "Topological phases in graphene nanoribbons: junction states, spin centers, and quantum spin chains," *Phys. Rev. Lett.*, vol. 119, no. 7, p. 076 401, 2017. DOI: `10.1103/PhysRevLett.119.076401`.

[21] D. J. Rizzo *et al.*, "Topological band engineering of graphene nanorib-bons," *Nature*, vol. 560, no. 7717, pp. 204–208, 2018. DOI: `10.1038/s41586-018-0376-8`.

[22] L. Grill *et al.*, "Nano-architectures by covalent assembly of molecular building blocks," *Nat. Nanotechnol.*, vol. 2, no. 11, pp. 687–691, 2007. DOI: `10.1038/nnano.2007.346`.

[23] J. Cai *et al.*, "Atomically precise bottom-up fabrication of graphene nanoribbons," *Nature*, vol. 466, no. 7305, pp. 470–473, 2010. DOI: `10.1038/nature09211`.

[24] Y.-C. Chen *et al.*, "Tuning the band gap of graphene nanoribbons synthesized from molecular precursors," *ACS Nano*, vol. 7, no. 7, pp. 6123–6128, 2013. DOI: `10.1021/nn401948e`.

[25] P. Ruffieux *et al.*, "On-surface synthesis of graphene nanoribbons with zigzag edge topology," *Nature*, vol. 531, pp. 489–492, 2016. DOI: `10.1038/nature17151`.

[26] O. Gröning *et al.*, "Engineering of robust topological quantum phases in graphene nanoribbons," *Nature*, vol. 560, no. 7717, pp. 209–213, 2018. DOI: `10.1038/s41586-018-0375-9`.

[27] P. H. Jacobse, M. J. J. Mangnus, S. J. M. Zevenhuizen, and I. Swart, "Mapping the conductance of electronically decoupled graphene nanoribbons," *ACS Nano*, vol. 12, pp. 7048–7056, 2018. DOI: `10.1021/acsnano.8b02770`.

[28] B. Voigtländer, *Scanning probe microscopy: Atomic force microscopy and scanning tunneling microscopy*, 1st ed. Heidelberg, Germany: Springer Berlin, 2015. DOI: `10.1007/978-3-662-45240-0`.

[29] G. Binnig, H. Rohrer, C. Gerber, and E. Weibel, "Tunneling through a controllable vacuum gap," *Appl. Phys. Lett.*, vol. 40, no. 2, pp. 178–180, 1982. DOI: `10.1063/1.92999`.

[30] G. Binnig, H. Rohrer, C. Gerber, and E. Weibel, "Surface studies by scanning tunneling microscopy," *Physical review letters*, vol. 49, no. 1, p. 57, 1982. DOI: `10.1103/PhysRevLett.49.57`.

[31] J. Bardeen, "Tunnelling from a many-particle point of view," *Phys. Rev. Lett.*, vol. 6, no. 2, pp. 57–59, 1961. DOI: `10.1103/PhysRevLett.6.57`.

[32] J. Tersoff and D. R. Hamann, "Theory of the scanning tunneling microscope," *Phys. Rev. B*, vol. 31, no. 2, pp. 805–813, 1985. DOI: `10.1103/PhysRevB.31.805`.

[33] R. Temirov, S. Soubatch, O. Neucheva, A. C. Lassise, and F. S. Tautz, "A novel method achieving ultra-high geometrical resolution in scanning tunnelling microscopy," *New J. Phys.*, vol. 10, pp. 1–11, 2008. DOI: `10.1088/1367-2630/10/5/053012`.

[34] L. Gross, F. Mohn, N. Moll, P. Liljeroth, and G. Meyer, "The chemical structure of a molecule resolved by atomic force microscopy," *Science*, vol. 325, no. 5944, pp. 1110–1114, 2009. DOI: `10.1126/science.1176210`.

[35] G. Kichin, C. Weiss, C. Wagner, F. S. Tautz, and R. Temirov, "Single molecule and single atom sensors for atomic resolution imaging of chemically complex surfaces," *J. Am. Chem. Soc.*, vol. 133, pp. 16 847–16 851, 2011. DOI: `10.1021/ja204624g`.

[36] N. Pavliček *et al.*, "Atomic force microscopy reveals bistable configurations of dibenzo [a,h]thianthrene and their interconversion pathway," *Physical Review Letters*, vol. 108, no. 8, p. 086 101, 2012. DOI: `10.1103/PhysRevLett.108.086101`.

[37] L. Gross *et al.*, "Bond-order discrimination by atomic force microscopy," *Science*, vol. 337, no. 6100, pp. 1326–1329, 2012. DOI: `10.1126/science.1225621`.

[38] P. Hapala *et al.*, "Mapping the electrostatic force field of single molecules from high-resolution scanning probe images," *Nat. Commun.*, vol. 7, no. 1, p. 11 560, 2016. DOI: `10.1038/ncomms11560`.

[39] L. Gross *et al.*, "High-resolution molecular orbital imaging using a *p*-wave STM tip," *Phys. Rev. Lett.*, vol. 107, no. 8, p. 086 101, 2011. DOI: `10.1103/PhysRevLett.107.086101`.

[40] O. Krejčí, P. Hapala, M. Ondráček, and P. Jelínek, "Principles and simulations of high-resolution STM imaging with a flexible tip apex," *Phys. Rev. B*, vol. 95, no. 4, p. 045 407, 2017. DOI: `10.1103/PhysRevB.95.045407`.

[41] P. Jelínek, "High resolution SPM imaging of organic molecules with functionalized tips," *J. Phys.: Condens. Matter*, vol. 29, no. 34, p. 343 002, 2017. DOI: `10.1088/1361-648X/aa76c7`.

[42] D. M. Eigler and E. K. Schweizer, "Positioning single atoms with a scanning tunnelling microscope," *Nature*, vol. 344, no. 6266, pp. 524–526, 1990. DOI: 10.1038/344524a0.

[43] M. F. Crommie, C. P. Lutz, and D. M. Eigler, "Confinement of electrons to quantum corrals on a metal surface," *Science*, vol. 262, no. 5131, pp. 218–220, 1993. DOI: 10.1126/science.262.5131.218.

[44] P. Zeppenfeld, C. P. Lutz, and D. M. Eigler, "Manipulating atoms and molecules with a scanning tunneling microscope," *Ultramicroscopy*, vol. 42, pp. 128–133, 1992. DOI: 10.1016/0304-3991(92)90256-J.

[45] G. Meyer, B. Neu, and K.-H. Rieder, "Controlled lateral manipulation of single molecules with the scanning tunneling microscope," *Appl. Phys. A*, vol. 60, no. 3, pp. 343–345, 1995. DOI: 10.1007/BF01538415.

[46] T. A. Jung, R. R. Schlittler, J. K. Gimzewski, H. Tang, and C. Joachim, "Controlled room-temperature positioning of individual molecules: molecular flexure and motion," *Science*, vol. 271, no. 5246, pp. 181–184, 1996. DOI: 10.1126/science.271.5246.181.

[47] C. Wagner and R. Temirov, "Tunnelling junctions with additional degrees of freedom: An extended toolbox of scanning probe microscopy," *Progress in Surface Science*, vol. 90, no. 2, pp. 194–222, 2015. DOI: 10.1016/j.progsurf.2015.01.001.

[48] S. Wang *et al.*, "Giant edge state splitting at atomically precise graphene zigzag edges," *Nat. Commun.*, vol. 7, p. 11 507, 2016. DOI: 10.1038/ncomms11507.

[49] J. Repp, G. Meyer, S. M. Stojković, A. Gourdon, and C. Joachim, "Molecules on insulating films: scanning-tunneling microscopy imaging of individual molecular orbitals," *Phys. Rev. Lett.*, vol. 94, no. 2, pp. 1–4, 2005. DOI: 10.1103/PhysRevLett.94.026803.

[50] T. Esat, N. Friedrich, F. S. Tautz, and R. Temirov, "A standing molecule as a single-electron field emitter," *Nature*, vol. 558, no. 7711, pp. 573–576, 2018. DOI: 10.1038/s41586-018-0223-y.

[51] K. F. Kelly, D. Sarkar, G. D. Hale, S. J. Oldenburg, and N. J. Halas, "Threefold electron scattering on graphite observed with C_{60}-adsorbed STM tips," *Science*, vol. 273, no. 5280, pp. 1371–1373, 1996. DOI: 10.1126/science.273.5280.1371.

[52] C.-l. Chiang, C. Xu, Z. Han, and W. Ho, "Real-space imaging of molecular structure and chemical bonding by single-molecule inelastic tunneling probe," *Science*, vol. 344, no. 6186, pp. 885–888, 2014. DOI: `10.1126/science.1253405`.

[53] C. Wagner *et al.*, "Scanning quantum dot microscopy," *Phys. Rev. Lett.*, vol. 115, no. 2, pp. 1–5, 2015. DOI: `10.1103/PhysRevLett.115.026101`.

[54] C. Wagner *et al.*, "Quantitative imaging of electric surface potentials with single-atom sensitivity," *Nat. Mater.*, 2019. DOI: `10.1038/s41563-019-0382-8`.

[55] B. Verlhac *et al.*, "Atomic-scale spin sensing with a single molecule at the apex of a scanning tunneling microscope," *Science*, vol. 366, no. 6465, pp. 623–627, 2019. DOI: `10.1126/science.aax8222`.

[56] A. Gourdon, "On-surface covalent coupling in ultrahigh vacuum," *Angew. Chem. Int. Ed.*, vol. 47, no. 37, pp. 6950–6953, 2008. DOI: `10.1002/anie.200802229`.

[57] S.-W. Hla, L. Bartels, G. Meyer, and K.-H. Rieder, "Inducing all steps of a chemical reaction with the scanning tunneling microscope tip: towards single molecule engineering," *Phys. Rev. Lett.*, vol. 85, no. 13, pp. 2777–2780, 2000. DOI: `10.1103/PhysRevLett.85.2777`.

[58] F. Ullmann, "Ueber symmetrische Biphenylderivate," *Justus Liebig's Annalen der Chemie*, vol. 332, no. 1-2, pp. 38–81, 1904. DOI: `10.1002/jlac.19043320104`.

[59] J. Gaudioso, H. J. Lee, and W. Ho, "Vibrational analysis of single molecule chemistry: ethylene dehydrogenation on Ni(110)," *J. Am. Chem. Soc.*, vol. 121, no. 37, pp. 8479–8485, 1999. DOI: `10.1021/ja991218s`.

[60] N. Pavliček *et al.*, "On-surface generation and imaging of arynes by atomic force microscopy," *Nat. Chem.*, vol. 7, no. 8, pp. 623–628, 2015. DOI: `10.1038/nchem.2300`.

[61] B. Schuler *et al.*, "Reversible Bergman cyclization by atomic manipulation," *Nat. Chem.*, vol. 8, no. 3, pp. 220–224, 2016. DOI: `10.1038/nchem.2438`.

[62] N. Pavliček *et al.*, "Synthesis and characterization of triangulene," *Nat. Nanotechnol.*, vol. 12, pp. 308–311, 2017. DOI: `10.1038/nnano.2016.305`.

[63] I. Horcas *et al.*, "WSXM: A software for scanning probe microscopy and a tool for nanotechnology," *Rev. Sci. Inst.*, vol. 78, no. 1, 2007. DOI: 10.1063/1.2432410.

[64] J. D. Hunter, "Matplotlib: A 2D graphics environment," *Comput. Sci. Eng.*, vol. 9, pp. 90–95, 2007. DOI: 10.1109/MCSE.2007.55.

[65] P. Kovesi, "Good colour maps: how to design them," *arXiv preprint arXiv:1509.03700*, 2015. DOI: 10.48550/arXiv.1509.03700.

[66] S. W. Wu, G. V. Nazin, X. Chen, X. H. Qiu, and W. Ho, "Control of relative tunneling rates in single molecule bipolar electron transport," *Phys. Rev. Lett.*, vol. 93, no. 23, p. 236 802, 2004. DOI: 10.1103/PhysRevLett.93.236802.

[67] M. A. Reed, C. Zhou, C. J. Muller, T. P. Burgin, and J. M. Tour, "Conductance of a molecular junction," *Science (New York, N.Y.)*, vol. 278, no. 5336, pp. 252–254, 1997. DOI: 10.1126/science.278.5336.252.

[68] V. Mujica, M. Kemp, and M. A. Ratner, "Electron conduction in molecular wires. I. A scattering formalism," *J. Chem. Phys.*, vol. 101, no. 8, pp. 6849–6855, 1994. DOI: 10.1063/1.468314.

[69] M. Di Ventra, S. T. Pantelides, and N. D. Lang, "First-principles calculation of transport properties of a molecular device," *Phys. Rev. Lett.*, vol. 84, no. 5, pp. 979–982, 2000. DOI: 10.1103/PhysRevLett.84.979.

[70] K.-H. Müller, "Effect of the atomic configuration of gold electrodes on the electrical conduction of alkanedithiol molecules," *Phys. Rev. B*, vol. 73, no. 4, p. 045 403, 2006. DOI: 10.1103/PhysRevB.73.045403.

[71] C. Joachim and J. F. Vinuesa, "Length dependence of the electronic transparence (conductance) of a molecular wire," *Europhysics Letters (EPL)*, vol. 33, no. 8, pp. 635–640, 1996. DOI: 10.1209/epl/i1996-00391-2.

[72] M. Magoga and C. Joachim, "Conductance and transparence of long molecular wires," *Phys. Rev. B*, vol. 56, no. 8, pp. 4722–4729, 1997. DOI: 10.1103/PhysRevB.56.4722.

[73] T. Hansen, V. Mujica, and M. A. Ratner, "Cotunneling model for current-induced events in molecular wires," *Nano Lett.*, vol. 8, no. 10, pp. 3525–3531, 2008. DOI: 10.1021/nl801001q.

[74] V. Mujica, M. Kemp, and M. A. Ratner, "Electron conduction in molecular wires. II. Application to scanning tunneling microscopy," *J. Chem. Phys.*, vol. 101, no. 8, pp. 6856–6864, 1994. DOI: `10.1063/1.468315`.

[75] E. A. Weiss, M. R. Wasielewski, and M. A. Ratner, "Molecules as wires: molecule-assisted movement of charge and energy," in *Molecular Wires and Electronics. Topics in Current Chemistry*, vol. 257, 2005, pp. 103–133. DOI: `10.1007/b136068`.

[76] P. Gehring, J. M. Thijssen, and H. S. J. van der Zant, "Single-molecule quantum-transport phenomena in break junctions," *Nat. Rev. Phys.*, vol. 1, no. 6, pp. 381–396, 2019. DOI: `10.1038/s42254-019-0055-1`.

[77] W. B. Davis, M. R. Wasielewski, M. A. Ratner, V. Mujica, and A. Nitzan, "Electron transfer rates in bridged molecular systems: A phenomenological approach to relaxation," *J. Phys. Chem. A*, vol. 101, no. 35, pp. 6158–6164, 1997. DOI: `10.1021/jp970909c`.

[78] W. B. Davis, W. A. Svec, M. A. Ratner, and M. R. Wasielewski, "Molecular-wire behaviour in *p*-phenylenevinylene oligomers," *Nature*, vol. 396, no. 6706, pp. 60–63, 1998. DOI: `10.1038/23912`.

[79] S. Ho Choi, B. Kim, and C. D. Frisbie, "Electrical resistance of long conjugated molecular wires," *Science*, vol. 320, no. 5882, pp. 1482–1486, 2008. DOI: `10.1126/science.1156538`.

[80] S. H. Choi *et al.*, "Transition from tunneling to hopping transport in long, conjugated oligo-imine wires connected to metals," *J. Am. Chem. Soc.*, vol. 132, no. 12, pp. 4358–4368, 2010. DOI: `10.1021/ja910547c`.

[81] G. Foti and H. Vázquez, "Origin of vibrational instabilities in molecular wires with separated electronic states," *J. Phys. Chem. Lett.*, vol. 9, no. 11, pp. 2791–2796, 2018. DOI: `10.1021/acs.jpclett.8b00940`.

[82] Y.-W. Son, M. L. Cohen, and S. G. Louie, "Energy gaps in graphene nanoribbons," *Phys. Rev. Lett.*, vol. 97, p. 216 803, 2006. DOI: `doi/10.1103/PhysRevLett.97.216803`.

[83] L. Yang, C.-H. Park, Y.-W. Son, M. L. Cohen, and S. G. Louie, "Quasiparticle energies and band gaps in graphene nanoribbons," *Phys. Rev. Lett.*, vol. 99, p. 186 801, 2007. DOI: `10.1103/PhysRevLett.99.186801`.

[84] O. V. Yazyev, R. B. Capaz, and S. G. Louie, "Theory of magnetic edge states in chiral graphene nanoribbons," *Phys. Rev. B*, vol. 84, p. 115 406, 2011. DOI: `10.1103/PhysRevB.84.115406`.

[85] Y.-C. Chen *et al.*, "Molecular bandgap engineering of bottom-up synthesized graphene nanoribbon heterojunctions," *Nat. Nanotechnol.*, vol. 10, no. 2, pp. 156–160, 2015. DOI: 10.1038/nnano.2014.307.

[86] L. Talirz *et al.*, "Band gap of atomically precise graphene nanoribbons as a function of ribbon length and termination," *ChemPhysChem*, vol. 20, pp. 2348–2353, 2019. DOI: 10.1002/cphc.201900313.

[87] J. Li *et al.*, "Topological phase transition in chiral graphene nanoribbons: from edge bands to end states," *Nat. Commun.*, vol. 12, p. 5538, 2021. DOI: 10.1038/s41467-021-25688-z.

[88] S. Wu *et al.*, "Magnetotransport properties of graphene nanoribbons with zigzag edges," *Phys. Rev. Lett.*, vol. 120, p. 216 601, 2018. DOI: 10.1103/PhysRevLett.120.216601.

[89] J. Li *et al.*, "Single spin localization and manipulation in graphene open-shell nanostructures," *Nat. Commun.*, vol. 10, no. 1, p. 200, 2019. DOI: 10.1038/s41467-018-08060-6.

[90] R. Ortiz, N. A. García-Martínez, J. L. Lado, and J. Fernández-Rossier, "Electrical spin manipulation in graphene nanostructures," *Phys. Rev. B*, vol. 97, p. 195 425, 2018. DOI: 10.1103/PhysRevB.97.195425.

[91] M. Slota *et al.*, "Magnetic edge states and coherent manipulation of graphene nanoribbons," *Nature*, vol. 557, pp. 691–695, 2018. DOI: 10.1038/s41586-018-0154-7.

[92] J. Li *et al.*, "Survival of spin state in magnetic porphyrins contacted by graphene nanoribbons," *Sci. Adv.*, vol. 4, eaaq0582, 2018. DOI: 10.1126/sciadv.aaq0582.

[93] D. G. de Oteyza and T. Frederiksen, "Carbon-based nanostructures as a versatile platform for tunable π-magnetism," *arXiv preprint arXiv:2206.12981*, 2022. DOI: 10.48550/arXiv.2206.12981.

[94] R. R. Cloke *et al.*, "Site-specific substitutional boron doping of semiconducting armchair graphene nanoribbons," *J. Am. Chem. Soc.*, vol. 137, pp. 8872–8875, 2015. DOI: 10.1021/jacs.5b02523.

[95] S. Kawai *et al.*, "Atomically controlled substitutional boron-doping of graphene nanoribbons," *Nat. Commun.*, vol. 6, pp. 1–6, 2015. DOI: 10.1038/ncomms9098.

[96] E. Carbonell-Sanromà *et al.*, "Electronic properties of substitutionally boron-doped graphene nanoribbons on a Au(111) surface," *J. Phys. Chem. C*, vol. 122, pp. 16 092–16 099, 2018. DOI: `10.1021/acs.jpcc.8b03748`.

[97] E. Carbonell-Sanromà *et al.*, "Quantum dots embedded in graphene nanoribbons by chemical substitution," *Nano Lett.*, vol. 17, pp. 50–56, 2017. DOI: `10.1021/acs.nanolett.6b03148`.

[98] B. V. Senkovskiy *et al.*, "Boron-doped graphene nanoribbons: electronic structure and raman fingerprint," *ACS Nano*, vol. 12, pp. 7571–7582, 2018. DOI: `10.1021/acsnano.8b04125`.

[99] D. G. de Oteyza *et al.*, "Substrate-independent growth of atomically precise chiral graphene nanoribbons," *ACS Nano*, vol. 10, no. 9, pp. 9000–9008, 2016. DOI: `10.1021/acsnano.6b05269`.

[100] N. Merino-Díez *et al.*, "Unraveling the electronic structure of narrow atomically precise chiral graphene nanoribbons," *J. Phys. Chem. Lett.*, vol. 9, no. 1, pp. 25–30, 2018. DOI: `10.1021/acs.jpclett.7b02767`.

[101] J. Zak, "Berry's phase for energy bands in solids," *Phys. Rev. Lett.*, vol. 62, no. 23, pp. 2747–2750, 1989. DOI: `10.1103/PhysRevLett.62.2747`.

[102] D. Vanderbilt and R. D. King-Smith, "Electric polarization as a bulk quantity and its relation to surface charge," *Phys. Rev. B*, vol. 48, no. 7, pp. 4442–4455, 1993. DOI: `10.1103/PhysRevB.48.4442`.

[103] J.-W. Rhim, J. Behrends, and J. H. Bardarson, "Bulk-boundary correspondence from the intercellular Zak phase," *Phys. Rev. B*, vol. 95, no. 3, p. 035 421, 2017. DOI: `10.1103/PhysRevB.95.035421`.

[104] L. Fu and C. L. Kane, "Topological insulators with inversion symmetry," *Phys. Rev. B*, vol. 76, no. 4, p. 045 302, 2007. DOI: `10.1103/PhysRevB.76.045302`.

[105] W. P. Su, J. R. Schrieffer, and A. J. Heeger, "Solitons in polyacetylene," *Phys. Rev. Lett.*, vol. 42, no. 25, pp. 1698–1701, 1980. DOI: `10.1103/PhysRevLett.42.1698`.

[106] L. Kouwenhoven and L. Glazman, "Revival of the Kondo effect," *Phys. World*, vol. 14, no. 1, pp. 33–38, 2001. DOI: `10.1088/2058-7058/14/1/28`.

[107] W. J. de Haas, J. de Boer, and G. Van den Berg, "The electrical resistance of gold, copper and lead at low temperatures," *Physica*, vol. 1, no. 7-12, pp. 1115–1124, 1934. DOI: `10.1016/S0031-8914(34)80310-2`.

[108] J. Kondo, "Resistance minimum in dilute magnetic alloys," *Prog. Theor. Phys.*, vol. 32, no. 1, pp. 37–49, 1964. DOI: `10.1143/PTP.32.37`.

[109] A. A. Abrikosov, "On the anomalous temperature dependence of the resistivity of non-magnetic metals with a weak concentration of magnetic impurities," *Soviet Journal of Experimental and Theoretical Physics*, vol. 21, p. 660, 1965.

[110] K. G. Wilson, "The renormalization group: critical phenomena and the Kondo problem," *Rev. Mod. Phys.*, vol. 47, no. 4, pp. 773–840, 1975. DOI: `10.1103/RevModPhys.47.773`.

[111] P. W. Anderson, "Localized magnetic states in metals," *Physical Review*, vol. 124, no. 1, pp. 41–53, 1961. DOI: `10.1103/PhysRev.124.41`.

[112] J. R. Schrieffer and P. A. Wolff, "Relation between the Anderson and Kondo Hamiltonians," *Physical Review*, vol. 149, no. 2, pp. 491–492, 1966. DOI: `10.1103/PhysRev.149.491`.

[113] U. Fano, "Effects of configuration interaction on intensities and phase shifts," *Physical Review*, vol. 124, no. 6, pp. 1866–1878, 1961. DOI: `10.1103/PhysRev.124.1866`.

[114] M. Gruber, A. Weismann, and R. Berndt, "The Kondo resonance line shape in scanning tunnelling spectroscopy: instrumental aspects," *J. Phys.: Condens. Matter*, vol. 30, no. 42, p. 424 001, 2018. DOI: `10.1088/1361-648X/aadfa3`.

[115] H. O. Frota, "Shape of the Kondo resonance," *Phys. Rev. B*, vol. 45, no. 3, pp. 1096–1099, 1992. DOI: `10.1103/PhysRevB.45.1096`.

[116] M. Ternes, A. J. Heinrich, and W.-D. Schneider, "Spectroscopic manifestations of the Kondo effect on single adatoms," *J. Phys.: Condens. Matter*, vol. 21, no. 5, p. 053 001, 2009. DOI: `10.1088/0953-8984/21/5/053001`.

[117] K. Nagaoka, T. Jamneala, M. Grobis, and M. F. Crommie, "Temperature dependence of a single Kondo impurity," *Phys. Rev. Lett.*, vol. 88, no. 7, p. 4, 2002. DOI: `10.1103/PhysRevLett.88.077205`.

[118] A. F. Otte *et al.*, "The role of magnetic anisotropy in the Kondo effect," *Nat. Phys.*, vol. 4, no. 11, pp. 847–850, 2008. DOI: `10.1038/nphys1072`.

[119] J. Li *et al.*, "Uncovering the triplet ground state of triangular graphene nanoflakes engineered with atomic precision on a metal surface," *Phys. Rev. Lett.*, vol. 124, no. 17, p. 177 201, 2020. DOI: `10.1103/PhysRevLett.124.177201`.

[120] M. Fujita, K. Wakabayashi, K. Nakada, and K. Kusakabe, "Peculiar localized state at zigzag graphite edge," *J. Phys. Soc. Jpn.*, vol. 65, no. 7, pp. 1920–1923, 1996. DOI: `10.1143/JPSJ.65.1920`.

[121] Y. Hancock, A. Uppstu, K. Saloriutta, A. Harju, and M. J. Puska, "Generalized tight-binding transport model for graphene nanoribbon-based systems," *Phys. Rev. B*, vol. 81, no. 24, p. 245 402, 2010. DOI: `10.1103/PhysRevB.81.245402`.

[122] S. Sanz and T. Frederiksen, *hubbard v0.2.0*, `https://github.com/dipc-cc/hubbard`, 2022.

[123] K. Moth-Poulsen and T. Bjørnholm, "Molecular electronics with single molecules in solid-state devices," *Nat. Nanotechnol.*, vol. 4, no. 9, pp. 551–556, 2009. DOI: `10.1038/nnano.2009.176`.

[124] M. C. Chong *et al.*, "Bright electroluminescence from single graphene nanoribbon junctions," *Nano Lett.*, vol. 18, no. 1, pp. 175–181, 2018. DOI: `10.1021/acs.nanolett.7b03797`.

[125] H. Li *et al.*, "Electric field breakdown in single molecule junctions," *J. Am. Chem. Soc.*, vol. 137, no. 15, pp. 5028–5033, 2015. DOI: `10.1021/ja512523r`.

[126] J. Lawrence *et al.*, "Probing the magnetism of topological end states in 5-armchair graphene nanoribbons," *ACS Nano*, vol. 14, pp. 4499–4508, 2020. DOI: `doi/10.1021/acsnano.9b10191`.

[127] N. Friedrich *et al.*, "Magnetism of topological boundary states induced by boron substitution in graphene nanoribbons," *Phys. Rev. Lett.*, vol. 125, p. 146 801, 2020. DOI: `10.1103/PhysRevLett.125.146801`.

[128] N. Friedrich *et al.*, "Addressing electron spins embedded in metallic graphene nanoribbons," *ACS Nano*, vol. 16, no. 9, pp. 14 819–14 826, 2022. DOI: `10.1021/acsnano.2c05673`.

[129] K. J. Franke and J. I. Pascual, "Effects of Electron–Vibration coupling in transport through single molecules," *J. Phys.: Condens. Matter*, vol. 24, no. 39, p. 394 002, 2012. DOI: `10.1088/0953-8984/24/39/394002`.

[130] J. Overbeck *et al.*, "A universal length-dependent vibrational mode in graphene nanoribbons," *ACS Nano*, vol. 13, no. 11, pp. 13 083–13 091, 2019. DOI: 10.1021/acsnano.9b05817.

[131] H. Söde *et al.*, "Electronic band dispersion of graphene nanoribbons *via* fourier-transformed scanning tunneling spectroscopy," *Phys. Rev. B - Condensed Matter and Materials Physics*, vol. 91, no. 4, pp. 1–6, 2015. DOI: 10.1103/PhysRevB.91.045429.

[132] M. L. Perrin *et al.*, "Large negative differential conductance in single-molecule break junctions," *Nat. Nanotechnol.*, vol. 9, no. 10, pp. 830–834, 2014. DOI: 10.1038/nnano.2014.177.

[133] X. Chen *et al.*, "Molecular diodes with rectification ratios exceeding 10^5 driven by electrostatic interactions," *Nat. Nanotechnol.*, vol. 12, no. 8, pp. 797–803, 2017. DOI: 10.1038/nnano.2017.110.

[134] G.-P. Zhang *et al.*, "Large rectification ratio of up to 10^6 for conjugation-group-terminated undecanethiolate single-molecule diodes on pt electrodes," *J. Phys. Chem. C*, vol. 125, no. 38, pp. 20 783–20 790, 2021. DOI: 10.1021/acs.jpcc.1c04093.

[135] D. D. Awschalom, L. C. Bassett, A. S. Dzurak, E. L. Hu, and J. R. Petta, "Quantum spintronics: engineering and manipulating atom-like spins in semiconductors," *Science*, vol. 339, no. 6124, pp. 1174–1179, 2013. DOI: 10.1126/science.1231364.

[136] F. Lombardi *et al.*, "Quantum units from the topological engineering of molecular graphenoids," *Science*, vol. 366, no. 6469, pp. 1107–1110, 2019. DOI: 10.1126/science.aay7203.

[137] A. L. Sharpe *et al.*, "Emergent ferromagnetism near three-quarters filling in twisted bilayer graphene," *Science*, vol. 365, no. 6453, pp. 605–608, 2019. DOI: 10.1126/science.aaw3780.

[138] X. Wang *et al.*, "Heteroatom-doped graphene materials: syntheses, properties and applications," *Chem. Soc. Rev.*, vol. 43, no. 20, pp. 7067–7098, 2014. DOI: 10.1039/c4cs00141a.

[139] P. Błoński *et al.*, "Doping with graphitic nitrogen triggers ferromagnetism in graphene," *J. Am. Chem. Soc.*, vol. 139, no. 8, pp. 3171–3180, 2017. DOI: 10.1021/jacs.6b12934.

[140] E. H. Lieb, "Two theorems on the Hubbard model," *Phys. Rev. Lett.*, vol. 62, pp. 1201–1204, 1989. DOI: 10.1103/PhysRevLett.62.1201.

[141] J. J. Palacios, J. Fernández-Rossier, and L. Brey, "Vacancy-induced magnetism in graphene and graphene ribbons," *Phys. Rev. B*, vol. 77, no. 19, pp. 1–14, 2008. DOI: 10.1103/PhysRevB.77.195428,.

[142] H. Gonzalez-Herrero *et al.*, "Atomic-scale control of graphene magnetism by using hydrogen atoms," *Science*, vol. 352, no. 6284, pp. 437–441, 2016. DOI: 10.1126/science.aad8038.

[143] M. Ijäs *et al.*, "Electronic states in finite graphene nanoribbons: effect of charging and defects," *Phys. Rev. B*, vol. 88, no. 075429, pp. 1–14, 2013. DOI: 10.1103/PhysRevB.88.075429.

[144] Z. Pedramrazi *et al.*, "Concentration dependence of dopant electronic structure in bottom-up graphene nanoribbons," *Nano Lett.*, vol. 18, no. 6, pp. 3550–3556, 2018. DOI: 10.1021/acs.nanolett.8b00651.

[145] E. Carbonell-Sanromà *et al.*, "Doping of graphene nanoribbons *via* functional group edge modification," *ACS Nano*, vol. 11, pp. 7355–7361, 2017. DOI: 10.1021/acsnano.7b03522.

[146] J. Li *et al.*, "Electrically addressing the spin of a magnetic porphyrin through covalently connected graphene electrodes," *Nano Lett.*, vol. 19, pp. 3288–3294, 2019. DOI: 10.1021/acs.nanolett.9b00883.

[147] M. Ternes, "Spin excitations and correlations in scanning tunneling spectroscopy," *New J. Phys.*, vol. 17, p. 063 016, 2015. DOI: 10.1088/1367-2630/17/6/063016.

[148] S. Mishra *et al.*, "Topological frustration induces unconventional magnetism in a nanographene," *Nat. Nanotechnol.*, vol. 15, pp. 22–28, 2020. DOI: 10.1038/s41565-019-0577-9.

[149] S. Kawai *et al.*, "Multiple heteroatom substitution to graphene nanoribbon," *Sci. Adv.*, vol. 4, pp. 1–8, 2018. DOI: 10.1126/sciadv.aar7181.

[150] P. Zhang *et al.*, "π-magnetism and spin-dependent transport in boron pair doped armchair graphene nanoribbons," *Appl. Phys. Lett.*, vol. 120, no. 13, p. 132 406, 2022. DOI: 10.1063/5.0086377.

[151] X. Su, Z. Xue, G. Li, and P. Yu, "Edge state engineering of graphene nanoribbons," *Nano Lett.*, vol. 18, no. 9, pp. 5744–5751, 2018. DOI: 10.1021/acs.nanolett.8b02356.

[152] S. Clair and D. G. de Oteyza, "Controlling a chemical coupling reaction on a surface: tools and strategies for on-surface synthesis," *Chem. Rev.*, vol. 119, no. 7, pp. 4717–4776, 2019. DOI: 10.1021/acs.chemrev. 8b00601.

[153] W. L. Wang, S. Meng, and E. Kaxiras, "Graphene nanoflakes with large spin," *Nano Lett.*, vol. 8, pp. 241–245, 2008. DOI: 10.1021/nl072548a.

[154] W. L. Wang, O. V. Yazyev, S. Meng, and E. Kaxiras, "Topological frustration in graphene nanoflakes: magnetic order and spin logic devices," *Phys. Rev. Lett.*, vol. 102, p. 157201, 2009. DOI: 10.1103/ PhysRevLett.102.157201.

[155] Y. Zheng *et al.*, "Designer spin order in diradical nanographenes," *Nat. Commun.*, vol. 11, p. 6076, 2020. DOI: 10.1038/s41467-020-19834-2.

[156] A. Sánchez-Grande *et al.*, "Unravelling the open-shell character of peripentacene on Au(111)," *J. Phys. Chem. Lett.*, vol. 12, no. 1, pp. 330–336, 2020. DOI: 10.1021/acs.jpclett.0c02518.

[157] S. Mishra *et al.*, "Large magnetic exchange coupling in rhombus-shaped nanographenes with zigzag periphery," *Nat. Chem.*, vol. 13, pp. 581–586, 2021. DOI: 10.1038/s41557-021-00678-2.

[158] E. Turco *et al.*, "On−surface synthesis and characterization of supernonazethrene," *J. Phys. Chem. Lett.*, vol. 12, no. 34, pp. 8314–8319, 2021. DOI: 10.1021/acs.jpclett.1c02381.

[159] S. Mishra *et al.*, "Observation of fractional edge excitations in nanographene spin chains," *Nature*, vol. 598, pp. 287–292, 2021. DOI: 10.1038/s41586-021-03842-3.

[160] J. Hieulle *et al.*, "On-surface synthesis and collective spin excitations of a triangulene-based nanostar," *Angew. Chem., Int. Ed.*, vol. 60, pp. 25224–25229, 2021. DOI: 10.1002/anie.202108301.

[161] T. Wang *et al.*, "Magnetic interactions between radical pairs in chiral graphene nanoribbons," *Nano Lett.*, vol. 22, pp. 164–171, 2021. DOI: 10.1021/acs.nanolett.1c03578.

[162] K. Biswas *et al.*, "Synthesis and characterization of peri-heptacene on a metallic surface," *Angew. Chem., Int. Ed.*, vol. 61, no. 23, e202114983, 2022. DOI: https://doi.org/10.1002/anie.202114983.

[163] T. Wang *et al.*, "Aza-triangulene: on-surface synthesis and electronic and magnetic properties," *J. Am. Chem. Soc.*, vol. 144, pp. 4522–4529, 2022. DOI: 10.1021/jacs.1c12618.

[164] S. Karan *et al.*, "Interplay of boundary states of graphene nanoribbons with a Kondo impurity," *Phys. Rev. B*, vol. 105, p. 205 410, 2022. DOI: `10.1103/PhysRevB.105.205410`.

[165] S. Song *et al.*, "Designer magnetic topological graphene nanoribbons," *arXiv preprint arXiv:2204.12880*, 2022. DOI: `10.48550/arXiv.2204.12880`.

[166] K. Sun *et al.*, "Manipulation of spin polarization in boron-substituted graphene nanoribbons," *ACS Nano*, vol. 16, no. 7, pp. 11 244–11 250, 2022. DOI: `10.1021/acsnano.2c04563`.

[167] S. Mishra *et al.*, "Topological defectinduced magnetism in a nanographene," *J. Am. Chem. Soc.*, vol. 142, pp. 1147–1152, 2020. DOI: `10.1021/jacs.9b09212`.

[168] S. Mishra *et al.*, "Collective allcarbon magnetism in triangulene dimers," *Angew. Chem., Int. Ed.*, vol. 59, pp. 12 041–12 047, 2020. DOI: `10.1002/anie.202002687`.

[169] B. Cirera *et al.*, "Tailoring topological order and π-conjugation to engineer quasi-metallic polymers," *Nat. Nanotechnol.*, vol. 15, no. 6, pp. 437–443, 2020. DOI: `10.1038/s41565-020-0668-7`.

[170] A. Sánchez-Grande *et al.*, "Diradical organic one-dimensional polymers synthesized on a metallic surface," *Angew. Chem., Int. Ed.*, vol. 59, no. 40, pp. 17 594–17 599, 2020. DOI: `10.1002/anie.202006276`.

[171] A. Tzalenchuk *et al.*, "Towards a quantum resistance standard based on epitaxial graphene," *Nat. Nanotechnol.*, vol. 5, pp. 186–189, 2010. DOI: `10.1038/nnano.2009.474`.

[172] J. Aprojanz *et al.*, "Ballistic tracks in graphene nanoribbons," *Nat. Commun.*, vol. 9, pp. 2–7, 2018. DOI: `/10.1038/s41467-018-06940-5`.

[173] H. Karakachian *et al.*, "One-dimensional confinement and width-dependent bandgap formation in epitaxial graphene nanoribbons," *Nat. Commun.*, vol. 11, pp. 1–8, 2020. DOI: `10.1038/s41467-020-19051-x`.

[174] M. Fritton *et al.*, "The influence of ortho-methyl substitution in organometallic self-assembly - a comparative study on Cu(111) *vs.* Ag(111)," *Chem. Commun.*, vol. 54, no. 70, pp. 9745–9748, 2018. DOI: `10.1039/c8cc04854a`.

[175] D. Barton *et al.*, "Formation of organometallic intermediate states in on-surface Ullmann couplings," *Chem. - Eur. J.*, vol. 23, pp. 6190–6197, 2017. DOI: `10.1002/chem.201605802`.

[176] J. M. Beebe, V. B. Engelkes, L. L. Miller, and C. D. Frisbie, "Contact resistance in metal-molecule-metal junctions based on aliphatic SAMs: effects of surface linker and metal work function," *J. Am. Chem. Soc.*, vol. 124, pp. 11 268–11 269, 2002. DOI: `doi/10.1021/ja0268332`.

[177] L. Venkataraman *et al.*, "Single-molecule circuits with well-defined molecular conductance," *Nano Lett.*, vol. 6, pp. 458–462, 2006. DOI: `10.1021/nl052373+`.

[178] P. W. Anderson, "Theory of localized magnetic states in metals," *J. Appl. Phys.*, vol. 37, p. 1194, 1966. DOI: `10.1063/1.1708389`.

[179] N. Roch, S. Florens, T. A. Costi, W. Wernsdorfer, and F. Balestro, "Observation of the underscreened Kondo effect in a molecular transistor," *Phys. Rev. Lett.*, vol. 103, p. 197 202, 2009. DOI: `10.1103/PhysRevLett.103.197202`.

[180] X. Peng *et al.*, "Visualizing designer quantum states in stable macrocycle quantum corrals," *Nat. Commun.*, vol. 12, p. 5895, 2021. DOI: `10.1038/s41467-021-26198-8`.

[181] S. Fatayer *et al.*, "Probing molecular excited states by atomic force microscopy," *Phys. Rev. Lett.*, vol. 126, p. 176 801, 2021. DOI: `10.1103/PhysRevLett.126.176801`.

[182] R. Vincent, S. Klyatskaya, M. Ruben, W. Wernsdorfer, and F. Balestro, "Electronic read-out of a single nuclear spin using a molecular spin transistor," *Nature*, vol. 488, no. 7411, pp. 357–360, 2012. DOI: `10.1038/nature11341`.

[183] S. Thiele *et al.*, "Electrically driven nuclear spin resonance in single-molecule magnets," *Science*, vol. 344, no. 6188, pp. 1135–1138, 2014. DOI: `10.1126/science.1249802`.

[184] R. Gaudenzi *et al.*, "Exchange coupling inversion in a high-spin organic triradical molecule," *Nano Lett.*, vol. 16, no. 3, pp. 2066–2071, 2016. DOI: `10.1021/acs.nanolett.6b00102`.

[185] E. Lörtscher, "Wiring molecules into circuits," *Nature Nanotechnol.*, vol. 8, no. 6, pp. 381–384, 2013. DOI: `10.1038/nnano.2013.105`.

[186] S. V. Aradhya and L. Venkataraman, "Single-molecule junctions beyond electronic transport," *Nature Nanotechnol.*, vol. 8, no. 6, pp. 399–410, 2013. DOI: 10.1038/nnano.2013.91.

[187] D. Xiang, X. Wang, C. Jia, T. Lee, and X. Guo, "Molecular-scale electronics: from concept to function," *Chem. Rev.*, vol. 116, no. 7, pp. 4318–4440, 2016. DOI: 10.1021/acs.chemrev.5b00680.

[188] J. W. Ruitenberg *et al.*, "Room-temperature gating of molecular junctions using few-layer graphene nanogap electrodes," *Nano Lett.*, vol. 11, no. 11, pp. 4607–4611, 2011. DOI: 10.1021/nl202065x.

[189] J. H. Warner *et al.*, "Scaling limits of graphene nanoelectrodes," *Nano Lett.*, vol. 17, no. 6, pp. 3688–3693, 2017. DOI: 10.1021/acs.nanolett.7b00909.

[190] W. Auwärter, D. Écija, F. Klappenberger, and J. V. Barth, "Porphyrins at interfaces," *Nat. Chem.*, vol. 7, no. 2, pp. 105–120, 2015. DOI: 10.1038/nchem.2159.

[191] X. Li, L. Cao, H. L. Li, H. Wan, and G. Zhou, "Spin-resolved transport properties of a pyridine-linked single molecule embedded between zigzag-edged graphene nanoribbon electrodes," *J. Phys. Chem. C*, vol. 120, no. 5, pp. 3010–3018, 2016. DOI: 10.1021/acs.jpcc.5b10880.

[192] J. C. Oberg *et al.*, "Control of single-spin magnetic anisotropy by exchange coupling," *Nature Nanotechnol.*, vol. 9, no. 1, pp. 64–68, 2014. DOI: 10.1038/nnano.2013.264.

[193] V. M. García-Suárez *et al.*, "Spin signatures in the electrical response of graphene nanogaps," *Nanoscale*, vol. 10, no. 38, pp. 18 169–18 177, 2018. DOI: 10.1039/C8NR06123H.

[194] L. Talirz, P. Ruffieux, and R. Fasel, "On-surface synthesis of atomically precise graphene nanoribbons," *Adv. Mater.*, vol. 28, no. 29, pp. 6222–6231, 2016. DOI: 10.1002/adma.201505738.

[195] D. G. de Oteyza and C. Rogero, *On-surface synthesis II*, D. G. de Oteyza and C. Rogero, Eds. Cham: Springer International Publishing, 2018. DOI: 10.1007/978-3-319-75810-7.

[196] D. G. De Oteyza *et al.*, "Substrate-independent growth of atomically precise chiral graphene nanoribbons," *ACS Nano*, vol. 10, no. 9, pp. 9000–9008, 2016. DOI: 10.1021/acsnano.6b05269.

[197] A. Wiengarten *et al.*, "Surface-assisted cyclodehydrogenation; break the symmetry, enhance the selectivity," *Chem. Eur. J*, vol. 21, no. 35, pp. 12 285–12 290, 2015. DOI: `10.1002/chem.201502001`.

[198] J. Hieulle *et al.*, "On-surface route for producing planar nanographenes with azulene moieties," *Nano Lett.*, 2017. DOI: `10.1021/acs.nanolett.7b04309`.

[199] C. Rubio-Verdú *et al.*, "Orbital-selective spin excitation of a magnetic porphyrin," *Comm. Phys.*, vol. 1, p. 15, 2018. DOI: `10.1038/s42005-018-0015-6`.

[200] M. C. Chong *et al.*, "Narrow-line single-molecule transducer between electronic circuits and surface plasmons," *Phys. Rev. Lett.*, vol. 116, no. 3, p. 036 802, 2016. DOI: `10.1103/PhysRevLett.116.036802`.

[201] S. Karan *et al.*, "Spin control induced by molecular charging in a transport junction," *Nano Lett.*, vol. 18, no. 1, pp. 88–93, 2018. DOI: `10.1021/acs.nanolett.7b03411`.

[202] D. Jacob, "Simulation of inelastic spin flip excitations and Kondo effect in STM spectroscopy of magnetic molecules on metal substrates," *J. Phys.: Condens. Matter*, vol. 30, no. 35, p. 354 003, 2018. DOI: `10.1088/1361-648X/aad523`.

[203] D. Jacob, "Renormalization of single-ion magnetic anisotropy in the absence of the Kondo effect," *Phys. Rev. B*, vol. 97, no. 7, pp. 1–8, 2018. DOI: `10.1103/PhysRevB.97.075428`.

[204] K. Haule, C.-H. Yee, and K. Kim, "Dynamical mean-field theory within the full-potential methods: electronic structure of CeIrIn$_5$, CeCoIn$_5$, and CeRhIn$_5$," *Phys. Rev. B*, vol. 81, p. 195 107, 2010. DOI: `10.1103/PhysRevB.81.195107`.

[205] J. J. Parks *et al.*, "Mechanical control of spin states in spin-1 molecules and the underscreened Kondo effect," *Science*, vol. 328, no. 5984, pp. 1370–1373, 2010. DOI: `10.1126/science.1186874`.

[206] B. Bryant, a. Spinelli, J. J. T. Wagenaar, M. Gerrits, and a. F. Otte, "Local control of single atom magnetocrystalline anisotropy," *Phys. Rev. Lett.*, vol. 111, no. 12, p. 127 203, 2013. DOI: `10.1103/PhysRevLett.111.127203`.

[207] W. J. Cho, Y. Cho, S. K. Min, W. Y. Kim, and K. S. Kim, "Chromium porphyrin arrays as spintronic devices," *J. Am. Chem. Soc.*, vol. 133, no. 24, pp. 9364–9369, 2011. DOI: `10.1021/ja111565w`.

List of Publications

Publications included in this Thesis

- **N Friedrich**, R. Menchón, I. Pozo, J. Hieulle, A. Vegliante, J. Li, D. Sánchez-Portal, D. Peña, A. Garcia-Lekue, and J. Pascual, "Addressing electron spins embedded in metallic graphene nanoribbons," *ACS Nano*, vol. 16, no. 9, pp. 14 819–14 826, 2022. DOI: 10.1021/acsnano.2c05673

- **N Friedrich**, P. Brandimarte, J. Li, S. Saito, S. Yamaguchi, I. Pozo, D. Peña, T. Frederiksen, A. Garcia-Lekue, D. Sánchez-Portal, and J. Pascual, "Magnetism of topological boundary states induced by boron substitution in graphene nanoribbons," *Physical Review Letters*, vol. 125, p. 146 801, 2020. DOI: 10.1103/PhysRevLett.125.146801

- J. Li, **N Friedrich**, N. Merino, D. de Oteyza, D. Peña, D. Jacob, and J. Pascual, "Electrically addressing the spin of a magnetic porphyrin through covalently connected graphene electrodes," *Nano Letters*, vol. 19, no. 5, pp. 3288–3294, 2019. DOI: 10.1021/acs.nanolett.9b00883

Further publications

- T. Wang, A. Berdonces-Layunta, **N Friedrich**, V.-V. M, J. Calupitan, J. Pascual, D. Peña, D. Casanova, M. Corso, and D. de Oteyza, "Aza-triangulene: On-surface synthesis, electronic and magnetic properties," *Journal of the American Chemical Society*, vol. 144, pp. 4522–4529, 2022. DOI: 10.1021/jacs.1c12618

- J. Hieulle, S. Castro, **N Friedrich**, A. Vegliante, F. Lara, S. Sanz, D. Rey, M. Corso, T. Frederiksen, J. Pascual, and D. Peña, "On-surface synthesis and collective spin excitations of a triangulene-based nanostar," *Angewandte Chemie International Edition*, vol. 60, pp. 25 224–25 229, 2021. DOI: 10.1002/anie.202108301

- D. Bikaljević, C. González-Orellana, M. Peña-Díaz, D. Steiner, J. Dreiser, P. Gargiani, M. Foerster, M. Niño, L. Aballe, S. Ruiz-Gomez, **N Friedrich**, J. Hieulle, L. Jingcheng, M. Ilyn, C. Rogero, and J. Pascual, "Noncollinear magnetic order in two-dimensional NiBr2 films grown on Au(111)," *ACS Nano*, vol. 15, pp. 14 985–14 995, 2021. DOI: 10.1021/acsnano.1c05221

- J. Li, S. Sanz, J. Castro-Esteban, M. Vilas-Varela, **N Friedrich**, T. Frederiksen, D. Peña, and J. Pascual, "Uncovering the triplet ground state of triangular graphene nanoflakes engineered with atomic precision on a metal surface," *Physical Review Letters*, vol. 124, p. 177 201, 2020. DOI: 10.1103/PhysRevLett.124.177201

- L. Xie, H. Lin, C. Zhang, J. Li, N. Merino-Díez, **N Friedrich**, X. Bouju, Y. Li, J. Pascual, and W. Xu, "Switching the spin on a ni trimer within a metal-organic motif by controlling the on-top bromine atom," *ACS Nano*, vol. 13, pp. 9936–9943, 2019. DOI: 10.1021/acsnano.9b04715

- C. Wagner, M. Green, M. Maiworm, P. Leinen, T. Esat, N. Ferri, **N Friedrich**, R. Findeisen, A. Tkatchenko, R. Temirov, and F. Tautz, "Quantitative imaging of electric surface potentials with single-atom sensitivity," *Nature Materials*, vol. 18, pp. 853–859, 2019. DOI: 10.1038/s41563-019-0382-8

- T. Esat, **N Friedrich**, F. Tautz, and R. Temirov, "A standing molecule as a single-electron field emitter," *Nature*, vol. 558, pp. 573–576, 2018. DOI: 10.1038/s41586-018-0223-y

- R. Temirov, M. Green, **N Friedrich**, P. Leinen, T. Esat, P. Chmielniak, S. Sarwar, J. Rawson, P. Kögerler, C. Wagner, M. Rohlfing, and F. Tautz, "Molecular model of a quantum dot beyond the constant interaction approximation," *Physical Review Letters*, vol. 120, p. 206 801, 2018. DOI: `10.1103/PhysRevLett.120.206801`

Author Contributions

The Chapters 3–6 are based on manuscripts containing significant contributions from several authors. Here, I provide a detailed list of the individual contributions to the manuscripts.

Chapter 3

Author contributions:
N.F. and J.I.P. conceived the experiment. **N.F.** and J.L. performed the on-sufrace synthesis and STM measurments. **N.F.** performed the STS measurements. S.S., S.Y. I.P. and D.P. synthesized the molecular precursors. **N.F.** analysed the experimental data. P.B., T.F., A.G.L. and D.S.P. performed the corresponding DFT simulations. **N.F.** and J.I.P. wrote the manuscript (with input from all authors). **N.F.**, P.B., J.L., T.F. A.G.L., D.S.P. and J.I.P. contributed to the discussion of the results. All authors discussed and approved the manuscript.

Chapter 4

Author contributions:
N.F. and J.I.P. conceived the experiment. **N.F.**, J.L., E.C.S. and M.C. performed on-sufrace synthesis and STM measurments. **N.F.** performed the STS measurements. I.P. and D.P. designed and synthesized the molecular precursors. **N.F.** analysed the data. **N.F.**, L.M. and T.F. performed the MFH simulations. P.B., T.F. and A.G.L. performed the corresponding DFT simulations. **N.F.** wrote the manuscript. **N.F.**, P.B., T.F., A.G.L., D.S.P. and J.I.P discussed the results.

Chapter 5

Author contributions:

N.F., J.H., A.V. and J.L. performed on-sufrace synthesis and STM measurments. I.P., D.P. and J.I.P. designed and synthesized the molecular precursors. **N.F.** analysed the data. R.E.M. performed the theoretical calculations under supervision of A.G.L. **N.F.**, R.E.M., D.S.P., A.G.L. and J.I.P. interpreted the theoretical calculations. **N.F.** wrote the manuscript (with input from all authors). All authors contributed to the discussion of the manuscript.

Chapter 6

Author contributions:

J.L. and J.I.P. conceived the experiment. J.L. and **N.F.** performed on-sufrace synthesis and STM measurments. D.P. provided the chiral DBBA. J.L. analysed the data. D.J. performed the numerical simulations. J.I.P. supervised the project. J.L. wrote the manuscript. All authors contributed to the discussion of the results and the manuscript.

Resumen extendido

El campo emergente de la espintrónica molecular persigue procesar información usando el espín electrónico de moléculas orgánicas producidas *á la carte* utilizando métodos de síntesis de química orgánica. Las nanoestructuras de grafeno representan una plataforma molecular prometedora para la espintrónica de moléculas individuales por combinar movilidad de electrones a través de partes conjugadas con la posibilidad de estabilizar estados de espín. La investigación orientada en las aplicaciones para la industria es capaz de integrar copos de grafeno en dispositivos de transporte para procesar información. Recientemente, la colaboración entre químicxs y físicxs generó avances importantes en la fabricación y caracterización de nanoestructuras de grafeno con estados de espín estables. Sin embargo, su estudio mediante transporte electrónico para evaluar el potencial de la espintrónica de moléculas individuales sigue siendo un desafío.

Conceptos físicos y técnicas experimentales

En esta tesis, investigo el transporte electrónico de dos contactos a través de nanotiras de grafeno (GNRs por su denominación en inglés) individuales con polarización interna de espín. Para realizar estos experimentos de transporte las GNRs se sitúan entre la punta y el sustrato de un microscopio de efecto túnel de temperatura baja, formando así un puente entre ambos. En esta tesis, me centro en el estudio de tres tipos de GNRs: nanotiras de grafeno de borde "armchair" con siete átomos de carbono de ancho (7-aGNR), otras con una variación de su anchura entre cinco y siete átomos (575-aGNR), ambas dopadas con boro, y una estructura híbrida de nanotiras de grafeno de orientación quiral-(3,1) con porfirina de hierro.

Las nanotiras han sido fabricadas *in situ* bajo condiciones de ultra-alto vacío usando métodos de síntesis en superficie sobre un sustrato de Au(111). Las nanotiras se forman a partir de precursores moleculares por un primer paso de polimerización en una reacción de Ullmann, provocada al calentar el sustrato. En un segundo paso, se induce la planarización mediante una reacción de deshidrogenación cíclica a una temperatura más alta que en la anterior reacción. Caracterizo las moléculas con las técnicas de microscopía y espectroscopía de efecto túnel (STM y STS por su denominación en inglés). Imágenes tomadas a bajo voltaje, usando una punta funcionalizada con una molécula de CO, proporcionan resolución de enlaces intramoleculares y confirman la estructura atómica de las moléculas.

Mediante manipulación mecánica mediada por la punta de STM contacto un extremo de la nanotira y, retirando la punta de STM, desacoplo electrónicamente del sustrato la parte elevada. Para ese proceso, uso un programa desarrollado en nuestro grupo de investigación para controlar manualmente la posición de la punta de STM con precisión picométrica. Para contactar la molécula acerco la punta de STM con la electrónica de retroalimentación apagada y a bajo voltaje hasta que se forma un enlace entre ambos. Una vez formado dicho enlace, al alejar la punta del sustrato, se crea un puente molecular entre estos. En la parte que ya no está en contacto con la superficie se consigue un estado libre de hibridización con el sustrato. Esta configuración nos permite estudiar las propiedades prístinas de la nanotira parcialmente levantada.

Esta tesis demuestra que se puede acceder a estados con polarización de espín en nanotiras de grafeno a través del transporte coherente de electrones. Para ello mido la conductancia diferencial mediante STS. La presencia de una resonancia Kondo en los sistemas de $S = 1/2$ o excitaciones inelásticas con forma de escalón en los sistemas de $S = 1$ confirma la existencia de dichos estados.

Los resultados experimentales son complementados con simulaciones del modelo Hubbard para iluminar los diferentes orígenes de los estados con polarización de espín en los tres sistemas. Este modelo describe el movimiento de los electrones de un sitio electrónico a otro a través de procesos cinéticos facilitados por el efecto túnel. Además, el modelo integra un canje de Coulomb cuando dos electrones con espines opuestos comparten un mismo sitio. Cada átomo de carbono contribuye con un or-

bital p_z, degenerado en el espín del electrón, a la red conjugada de sitios electrónicos en una nanotira de grafeno. Aquí empleamos una aproximación de campo medio para obtener los autoestados del hamiltoniano de sistemas con cientos de átomos de carbono.

Transporte bipolar en nanotiras de grafeno

En una 7aGNR con un dopante de diboro emerge un estado localizado alrededor de los átomos de boro. En las cintas parcialmente levantadas, el estado localizado se sitúa en una configuración de doble barrera para electrones túnel y observamos transporte resonante mediado por el estado de boro, similar al observado en puntos cuánticos. Cambiando la distancia entre punta y sustrato, variamos la posición vertical del punto cuántico en la unión de túnel de manera continua. Observamos dos resonancias de transporte electrónico que se acercan mientras según aumenta la distancia entre punta y sustrato. Interpretamos ese resultado con un modelo simple de transporte resonante bipolar a través de un punto cuántico. Asumiendo que es el estado ocupado el que facilita el transporte resonante de electrones en ambas polarizaciones del voltaje, las simulaciones reproducen los datos experimentales.

Adicionalmente, observamos en los experimentos de transporte resonancias satélites causadas por vibraciones, con un cuanto de energía de 20 meV. Ese modo vibracional también está presente en el transporte resonante a través de la banda de valencia. Asimismo, la banda de valencia está cuantizada debido a una barrera de potencial asociada al dopante de boro. Como consecuencia de esto, la nanotira parcialmente levantada se comporta como un diodo con una rectificación de corriente en el mismo rango de los mejores dispositivos de moléculas orgánicas publicados.

Magnetismo de estados topológicos en nanotiras de grafeno inducido por dopaje substitutional de diboro

Una resonancia Kondo aparece en los experimentos de transporte a través de una nanotira 7aGNR dopada con una unidad de diboro (2B) al desacoplar el sitio del dopaje del sustrato. Esto indica una polarización de espín del estado del 2B. Nuestros cálculos combinados con métodos *ab initio* y un modelo de Hubbard de campo medio muestran que la falta

de dos electrones p_z en la posición del diboro, en combinación con la estabilización de dos sextetos de Clar a su alrededor, rompe la conjugación continua de los electrones de la banda de valencia. En consecuencia, dos estados de borde con protección topológica se forman en el interior de la nanotira en los dos lados de la unidad 2B.

Vemos que una interacción finita del canje de Coulomb entre los dos estados con polarización de espín resulta en un estado fundamental de triplete de espín con $S = 1$. Cuando hay más de un sitio de 2B en la nanotira, la interacción entre los tripletes es antiferromagnética y disminuye con la separación entre los dopantes 2B. Los estados de triplete presentan una interacción débil cuando existe una separación entre los sitios de 2B mayor que $3.5\,\mathrm{nm}$. Para distancias menores de $3.5\,\mathrm{nm}$, se predice la formación de una cadena de espines $S = 1$ con canje ferromagnético. Acercando los estados aún más, llegamos al punto en el cual el canje de Coulomb entre los dos espines de un sitio 2B es más débil que el canje entre dos espines $S = 1/2$ de sitios 2B colindantes. Entonces los dos espines de los sitios colindantes forman un estado de capa cerrada y la polarización de espín desaparece en la parte de la nanotira con dopaje sustitutional de 2B. La transición entre la cadena de espines y el estado de capa cerrada ocurre por una separación de los 2B de $\sim 1.5\,\mathrm{nm}$.

Recuperación de la fase topológica

Sorprendentemente, observamos una resonancia de Kondo similar al caso de la tira con un solo sitio de 2B en tiras con un dopaje suficientemente denso de 2B, donde el canje entre dos sitios 2B es más alto que el canje de Coulomb. En este sistema no se espera un estado topológico. Al simular el proceso de levantar la nanotira, usando teoría del funcional de la densidad, reproducimos un estado con polarización de espín dentro de una 7aGNR con dopaje denso de 2B que tiene una distribución espacial semejante al estado topológico observado en las 7aGNRs.

Empleamos el modelo de Hubbard de campo medio para racionalizar el origen de esta polarización de espín. El sustrato metálico facilita procesos donde los electrones "saltan" de un lado de la unidad 2B al otro. Estos procesos permiten una propagación libre de los electrones dentro de la banda de valencia de la nanotira, que, en consecuencia, da lugar a una recuperación aparente de su carácter topológico en el segmento de

la GNR en contacto con la superficie. Ese proceso está prohibido en la parte parcialmente levantada de la nanotira, bloqueando la propagación de electrones. Así, un estado con polarización de espín, parecido al estado de borde topológico, aparece en la cercanía del sustrato dentro de la parte no levantada de la nanotira.

Magnetismo en nanotiras de grafeno metálicas

Analizamos un nuevo caso donde se han eliminado ocho átomos de carbono en la celda unidad de las 7aGNR con dopaje denso de boro. Abreviamos las nuevas nanotiras como 2B-575-aGNRs. Las simulaciones de teoría del funcional de la densidad muestran que estas nanotiras poseen una banda plana con polarización de espín en cercanía al nivel de Fermi unificada con una banda dispersa cruzando E_{Fermi}, resultando en un sistema con carácter metálico.

En contraste a las 7aGNRs, la polarización de espín en las 2B-575-aGNRs no tiene origen topológico, pero está asociado a estados de boro. Encontramos que la polarización de espín forma una cadena de espines $S = 1/2$ con canje antiferromagnético entre sitios 2B colindantes. Las diferentes simetrías de las funciones de onda de la banda plana y la banda dispersa permiten la coexistencia de la polarización de espín en la primera y el carácter metálico debido a la segunda. En experimentos de transporte a través de esta nanotira, encontramos transporte balístico con altos valores de conductancia, llegando a $\sim 0.2G_0$; en combinación con una resonancia de Kondo estable en un rango de retracción de varios nanometros. Así, el experimento confirma las predicciones teóricas sobre los 2B-575-aGNRs al combinar un carácter metálico con un estado con polarización de espín.

Además, encontramos que la falta de un átomo específico de carbono en cada celda de unidad de los 2B-575-aGNRs, defecto frecuente en los experimentos, permite una interacción perturbativa entre la banda metálica de transporte y la banda plana. La eliminación de un átomo de carbono disminuye la energía de Fermi y reduce la población del estado de espín, resultando en una distribución de aproximadamente un electrón por dos sitios 2B. Los experimentos de transporte de dos contactos a través de nanotiras con el defecto muestran una resonancia Kondo o excitaciones inelásticas de electrones de efecto túnel. El primero en el

caso de una separación mediana entre punta y sustrato y el segundo en el caso de una separación alta.

Simulamos este proceso con un modelo de Hubbard, donde los sitios electrónicos representan los sitios 2B. El número de electrones es menor que el número de sitios de acuerdo con los resultados de los simulaciones de teoría de funcional de la densidad. Encontramos que la escala de energía relevante para describir las excitaciones inelásticas es el parámetro cinético del modelo. La interacción entre espines colindantes resulta en excitaciones de un par electrón-hueco, cambiando la ocupación de los sitios electrónicos y el estado de espín.

Acceso a un espín de capa d a través de una nanotira de grafeno

Finalmente, estudiamos el transporte de dos contactos a través de GNRs híbridas formadas por una porfirina de hierro contactada a dos GNRs quirales. Demostramos el acceso eléctrico a un espín en una capa electrónica d en un dispositivo híbrido vía inyección de carga a través de la nanotira de grafeno quiral que conecta la porfirina de hierro y los electrodos.

Vemos que la energía de anisotropía magnética del espín de la capa d, obtenida por espectroscopía de eventos inelásticos de electrones de efecto túnel, es idéntico en el caso de una transmisión directa de electrones de efecto túnel desde la punta de STM o de la inyección de electrones de transporte por la nanotira. El proceso inelástico implica que los electrones de transporte interaccionan directamente con el espín $S = 1$ localizado en la capa d del hierro, una condición necesaria para aplicaciones espintrónicas.

Por la reacción en superficie se crean porfirinas de diferentes simetrías alrededor del hierro. Nos enfocamos en el caso asimétrico ($C1$). En este caso la energía de anisotropía magnética aumenta a lo largo del proceso de levantar la molécula. La descripción del sistema en un modelo de impureza de Anderson de dos orbitales nos permite explicar este efecto como una renormalización de energía de anisotropía magnética en la molécula encima de la superficie. Esto es debido a una fluctuación de la carga en la capa d en la cual el espín está localizado. Las fluctuaciones desapare-

cen cuando el ion de hierro forma parte de la estructura híbrida elevada, recuperando la energía de anisotropía magnética prístina.

Conclusión

Los resultados presentados en esta tesis ponen a disposición un entendimiento más profundo de los orígenes, mecanismos y esquemas de detección de estados con polarización de espín en el interior de nanotiras de grafeno. El acceso electrónico de estos estados en una configuración de transporte de dos contactos, como se muestra en esta tesis, responde a preguntas sobre el surgimiento, la persistencia y la excitación de espines con corrientes de transporte de electrones, allanando el camino hacia una implementación de nanotiras de grafeno en dispositivos espintrónicos de moléculas individuales. El estudio de la profunda física de la molécula sin perturbación en esta tesis se debe a nuestra capacidad de desacoplar las GNRs parcialmente del sustrato, resultando en un segmento libre de hibridización.